

Universidade de Santiago de Compostela
Departamento de Física de Partículas



**STUDY OF LIGHT NEUTRON-RICH NUCLEI
VIA ONE-NEUTRON KNOCKOUT
REACTIONS**

Carme Rodríguez Tajés
under the direction of
Dolores Cortina Gil

September 2009

Dolores Cortina Gil, Profesora Titular do Departamento de Física de Partículas da **Universidade de Santiago de Compostela**,

CERTIFICO: Que a memoria titulada “**Study of light neutron-rich nuclei via one-neutron knockout reactions**” foi realizada por **Carme Rodríguez Tajés** baixo a miña dirección na Universidade de Santiago de Compostela e constitúe a Tese que presenta para obter ao grao de **Doutor en Ciencias Físicas**.

Santiago de Compostela, setembro de 2009

Asdo.: Dolores Cortina Gil

Asdo.: Carme Rodríguez Tajés

*El mundo era tan reciente,
que muchas cosas carecían de nombre,
y para mencionarlás
había que señalarlas con el dedo.*

Gabriel García Márquez,
“Cien años de soledad”

Contents

Resume en galego	1
1 Introduction	9
1.1 Nuclear-structure studies	9
1.2 Exploring single-particle properties through direct reactions	12
1.3 This work	15
2 The experiment	17
2.1 The Fragment Separator	17
2.1.1 The energy-loss mode	19
2.2 The detector setup	20
2.2.1 Multiple-sample ionisation chambers	21
2.2.2 Scintillators	23
2.2.3 Time-projection chambers	23
2.2.4 MINIBALL	25
3 Data analysis	27
3.1 MUSIC calibration	27
3.2 Time-of-flight calibration	28
3.3 TPC calibration	30
3.3.1 TPC efficiency at F2	34
3.3.2 Tracking at F2	37
3.4 Dispersion measurements	38
3.5 Location of the final focal plane	41
3.6 MINIBALL calibration	43
3.6.1 MINIBALL efficiency	45
4 The physical observables	49
4.1 Identification	49
4.1.1 Measuring the mass-to-charge ratio	50
4.2 Inclusive longitudinal-momentum distributions	52
4.2.1 Calculation of the longitudinal momentum	53
4.2.2 Momentum resolution	54
4.2.3 Acceptance cuts	55

4.2.4	FWHM of the longitudinal-momentum distributions	56
4.3	Inclusive cross-sections	59
4.3.1	Calculation of the inclusive cross-section	59
4.3.2	Transmission correction	61
4.3.3	Detection efficiency at F4	62
4.3.4	Results for the inclusive knockout cross-sections	62
4.4	Exclusive knockout cross-sections	64
4.4.1	Exclusive results for ^{17}C one-neutron knockout	66
4.4.2	Exclusive results for ^{19}N one-neutron knockout	67
4.4.3	Exclusive results for ^{21}O one-neutron knockout	69
4.4.4	Exclusive results for ^{25}F one-neutron knockout	71
5	Discussion of the results	73
5.1	Results for $^{14-19}\text{C}$	73
5.2	Results for $^{16-22}\text{N}$, $^{19-23}\text{O}$ and $^{21-26}\text{F}$	77
5.3	Results for $^{24-28}\text{Ne}$	78
5.3.1	Single-particle content from longitudinal-momentum distributions	82
	Conclusions	89
	A Optics of charged particles	95
A.1	The phase space	95
A.2	The transfer matrix	96
A.3	Measuring the longitudinal momentum	97
	B Inclusive longitudinal-momentum distributions	101
	C Transmission through the FRS	117
	D γ-ray measurements	121
	Bibliography	121

List of Figures

1.1	Single-particle shell model	10
1.2	Diffractive breakup	14
1.3	Neutron stripping	14
1.4	Light neutron-rich region of the nuclear landscape	15
2.1	GSI facilities	18
2.2	Fragment Separator	18
2.3	Energy-loss mode at the FRS	19
2.4	Detectors and measurements	20
2.5	Detector setup at the intermediate focal plane	21
2.6	Detector setup at the final focal plane	21
2.7	Schematic view of a MUSIC	22
2.8	Schematic view of a TPC	24
2.9	Schematic view of MINIBALL	25
2.10	MINIBALL cluster	25
3.1	MUSIC velocity correction	28
3.2	MUSIC calibration	29
3.3	TOF calibration	30
3.4	TPC signals and control-sum condition	31
3.5	TPC calibration	32
3.6	TPC misalignment at F2	33
3.7	Left <i>vs.</i> right TPC time signals	35
3.8	Left <i>vs.</i> right TPC time signals under the control-sum condition	36
3.9	Correlation between the direction tangents at F2 and F4	38
3.10	Experimental determination of the dispersion coefficients	40
3.11	Dispersion as a function of the longitudinal position at F4	41
3.12	Horizontal direction tangent <i>vs.</i> horizontal position at F4	42
3.13	Width of the horizontal position distribution at F4	42
3.14	MINIBALL signals	43
3.15	Doppler correction	44
3.16	MINIBALL energy calibration	45
3.17	MINIBALL efficiency for static calibration sources	46
3.18	MINIBALL dead time <i>vs.</i> spill time	47

3.19	Accepted γ triggers with null DGF signals <i>vs.</i> spill time	47
3.20	Counting rate for the 1460 keV background line <i>vs.</i> spill time	48
4.1	Corrections of the mass-to-charge ratio	50
4.2	Identification plots	51
4.3	Determination of the reaction channel	52
4.4	Momentum distributions from two sets of measurements	54
4.5	Momentum resolution of the FRS	55
4.6	Acceptance cuts through the FRS	56
4.7	Detection efficiency for γ rays <i>vs.</i> spill time	65
4.8	Analysis of the γ rays measured in ^{17}C one-neutron knockout	66
4.9	γ rays measured in ^{19}N one-neutron knockout	67
4.10	Coincidences between the γ rays observed in ^{19}N one-neutron knockout	68
4.11	Simulated and measured γ spectra in ^{19}N one-neutron knockout	69
4.12	Analysis of the γ rays measured in ^{21}O one-neutron knockout	70
4.13	Analysis of the γ rays measured in ^{25}F one-neutron knockout	71
5.1	Inclusive results for $^{14-19}\text{C}$	75
5.2	Inclusive results for $^{16-22}\text{N}$, $^{19-23}\text{O}$ and $^{21-26}\text{F}$	77
5.3	Inclusive results for $^{24-28}\text{Ne}$	81
5.4	Analysis of the inclusive momentum distributions in $^{22-23}\text{O}$ one-neutron knockout	85
5.5	Analysis of the inclusive momentum distributions in $^{24-26}\text{Ne}$ one-neutron knockout	87
5.6	Analysis of the inclusive momentum distributions in $^{27-28}\text{Ne}$ one-neutron knockout	88
A.1	Coordinate system used in the optics of charge particles	96
A.2	Schematic drawing of the FRS	98
B.1	Momentum distributions measured in $^{14-16}\text{C}$ one-neutron knockout	102
B.2	Momentum distributions measured in $^{17-19}\text{C}$ one-neutron knockout	103
B.3	Momentum distributions measured in $^{16-17}\text{N}$ one-neutron knockout	104
B.4	Momentum distributions measured in $^{18-19}\text{N}$ one-neutron knockout	105
B.5	Momentum distributions measured in $^{20-22}\text{N}$ one-neutron knockout	106
B.6	Momentum distributions measured in $^{19-21}\text{O}$ one-neutron knockout	107
B.7	Momentum distributions measured in $^{22-23}\text{O}$ one-neutron knockout	108
B.8	Momentum distributions measured in $^{21-23}\text{F}$ one neutron knockout	109
B.9	Momentum distributions measured in $^{24-26}\text{F}$ one-neutron knockout	110
B.10	Momentum distributions measured in $^{24-26}\text{Ne}$ one-neutron knockout	111
B.11	Momentum distributions measured in $^{27-28}\text{Ne}$ one-neutron knockout	112
B.12	Momentum distributions measured in $^{27-29}\text{Na}$ one-neutron knockout	113
B.13	Momentum distributions measured in $^{30-31}\text{Na}$ one-neutron knockout	114
B.14	Momentum distributions measured in $^{31-33}\text{Mg}$ one-neutron knockout	115

B.15	Momentum distributions measured in $^{34-35}\text{Al}$ one-neutron knockout	116
D.1	γ spectrum measured in ^{15}C one-neutron knockout.	121
D.2	γ spectrum measured in ^{16}C one-neutron knockout.	122
D.3	γ spectrum measured in ^{17}C one-neutron knockout.	122
D.4	γ spectrum measured in ^{17}N one-neutron knockout.	123
D.5	γ spectrum measured in ^{18}N one-neutron knockout.	123
D.6	γ spectrum measured in ^{19}N one-neutron knockout.	124
D.7	γ spectrum measured in ^{20}N one-neutron knockout.	124
D.8	γ spectrum measured in ^{20}O one-neutron knockout.	125
D.9	γ spectrum measured in ^{21}O one-neutron knockout.	125
D.10	γ spectrum measured in ^{22}O one-neutron knockout.	126
D.11	γ spectrum measured in ^{22}F one-neutron knockout.	126
D.12	γ spectrum measured in ^{23}F one-neutron knockout.	127
D.13	γ spectrum measured in ^{24}F one-neutron knockout.	127
D.14	γ spectrum measured in ^{25}F one-neutron knockout.	128

List of Tables

3.1	Correction of the TPC misalignment at F2	33
3.2	TPC signals verifying the control-sum condition at F2	34
3.3	Correct TPC signals at F2	36
3.4	Tracking possibilities at F2	37
3.5	MINIBALL efficiency for static calibration sources	46
4.1	Widths of the longitudinal-momentum distributions	59
4.2	TPC efficiency at F4	62
4.3	Inclusive one-neutron knockout cross-sections	63
4.4	Inclusive one-neutron knockout cross-sections corrected for reactions outside the target	63
4.5	Exclusive results for ^{17}C one-neutron knockout	66
4.6	Exclusive results on ^{19}N one-neutron knockout	69
4.7	Exclusive results for ^{21}O one-neutron knockout	70
4.8	Exclusive results for ^{25}F one-neutron knockout	71
5.1	Calculated <i>core</i> \otimes <i>neutron</i> contributions in the $^{22-23}\text{O}$ ground state .	86
5.2	Calculated <i>core</i> \otimes <i>neutron</i> contributions in the $^{24-28}\text{Ne}$ ground state .	88
C.1	FRS settings.	117
C.2	Transmission of the knockout fragments between F2 and F4	120

Resume en galego

Introdución

A visión actual dos sistemas nucleares e da súa estrutura desenvolveuse ao longo dos anos sen un coñecemento detallado das forzas involucradas. Neste contexto, a sinerxia entre a teoría e os experimentos xoga un papel fundamental, sendo as reaccións nucleares unha das maiores fontes de información empregada polos científicos para explorar a estrutura do núcleo atómico.

A descrición do núcleo evolucionou en paralelo á observación experimental. Medidas da enerxía de ligadura puxeron de manifesto a existencia dos chamados números máxicos, números de protóns e/ou neutróns asociados a núcleos especialmente ligados. A raíz deste descubrimento, suxeriuse unha estrutura de capas para os nucleóns no núcleo análoga á dos electróns nos átomos. En 1949, Mayer [May49] e Jensen [Hax49] melloraron considerablemente este modelo coa introdución dun novo termo no potencial que dá conta da interacción espín-órbita. Debido á necesidade de incluír varias partículas de valencia, o modelo de capas, que comezou sendo un modelo de partícula independente, converteuse máis tarde nunha teoría de moitos corpos que evolucionou para dar lugar a unha potente ferramenta de cálculo.

Os estudos de estrutura nuclear leváronse a cabo fundamentalmente para núcleos estables, na base dunha configuración de capas ben establecida con certos números máxicos asociados. Non obstante, nas últimas décadas, a dispoñibilidade de feixes radioactivos de alta enerxía permitiu acceder a condicións de gran asimetría de carga, gran isospín e enerxías de ligadura febles.

O réxime de alta enerxía (50 MeV/nucleón–1 GeV/nucleón) supón importantes vantaxes desde os puntos de vista experimental e teórico. É posible incrementar o espesor dos brancos e, debido á focalización cinemática cara diante, moderar o tamaño dos detectores. Ademais, os reducidos tempos de interacción e os pequenos ángulos de dispersión simplifican a descrición dos mecanismos de reacción subxacentes e a interpretación dos observables físicos.

A investigación experimental con feixes radioactivos relativistas comezou en 1979

en *Lawrence Berkeley Laboratory*, EEUU, [Ber], [Sym79, Wes79]. Poucos anos despois, Tanihata e colaboradores determinaron neste laboratorio o radio dos isótopos ${}^6\text{-}^{11}\text{Li}$ e ${}^7\text{-}^{10}\text{Be}$ a partir das súas seccións eficaces de interacción [Tan85]. O ${}^{11}\text{Li}$ distinguiuse entre os outros núcleos por ter un radio excepcionalmente grande, debido a unha cola de baixa densidade na función de onda dos neutróns de valencia. Os nucleóns menos ligados forman unha “nube” arredor do *core* central, dando lugar á que hoxe denominamos estrutura de halo [Han87]. Desde entón, outros núcleos con halo foron descubertos lonxe da estabilidade e novos candidatos foron propostos. Este é o caso do ${}^{22}\text{N}$, para o que se predixo unha extensa distribución espacial asociada cun neutrón $s_{1/2}$ [Oza00]. Existen datos espectroscópicos recentes que parecen reforzar esta hipótese [Soh08].

Cando nos afastamos da estabilidade β , a evolución da estrutura de capas amosa outros fenómenos interesantes, como a modificación dos tradicionais números máxicos. Algúns exemplos son o desvanecemento da capa pechada $N = 8$ para o ${}^{12}\text{Be}$ [Iwa00a, Iwa00b] e a aparición novas subcapas pechadas en $N = 14$ e 16 para os isótopos de osíxeno [Kan09, Oza00, Sta04]. Tal e como propoñen Otsuka e colaboradores [Ots01b], a interacción nucleón-nucleón podería ser responsable do novo salto enerxético en $N = 16$, en detrimento do número máxico $N = 20$, establecido para núcleos estables.

Por outra banda, atopáronse tamén estruturas inesperadas na rexión $N \sim 20$. Este efecto descubriuse en 1975, cando medidas da masa dos núcleos ${}^{31,32}\text{Na}$ indicaron formas non esféricas en desacordo co convencional peche de capa en $N = 20$ [Thi75]. Máis tarde, apareceron novas evidencias de deformación para o ${}^{32}\text{Mg}$ [Mot95] e o ${}^{30}\text{Ne}$ [Yan03]. Esta rexión denomínase *illa de inversión* porque se pensa que o estado fundamental consiste en configuracións intrusas con neutróns que ocuparían a capa *pf* en lugar da capa *sd*. Estudos co propósito de definir os límites desta rexión están levándose a cabo actualmente [Him08].

Explorando propiedades de partícula independente mediante reaccións directas

As reaccións directas empregáronse no pasado para estudar as propiedades de partícula independente dos núcleos estables. Entre elas, as reaccións de transferencia, onde se intercambian un ou máis nucleóns entre o proxectil e o branco, foron aplicadas recentemente a feixes radioactivos [Cat05b, Fer07, Gau06, Gau08, Win01]. As seccións eficaces típicas nestes experimentos rondan 1 mb e a enerxía óptima varía entre 10 e 20 MeV/nucleón. O uso dun espectrómetro magnético permite diferenciar o estado final do residuo e pode determinarse o momento angular orbital do nucleón transferido a partir da distribución angular, identificándose así as distintas configuracións de partícula independente.

Sen embargo, os experimentos de transferencia con núcleos exóticos só son posibles desde hai uns anos. Namentres, desenvolvéronse técnicas alternativas para traballar con feixes secundarios de alta enerxía e baixa intensidade. Este é o caso das reaccións de ruptura, con seccións eficaces que aumentan de 1 a 100 mb cando pasamos da estabilidade a núcleos pouco ligados. A natureza da interacción pode ser nuclear ou electromagnética, dependendo da carga do branco. Neste contexto, é interesante mencionar aqueles estudos relacionados co arranque dun nucleón, *single-nucleon knockout*¹, xa que proporcionan información básica sobre a estrutura de capas e permiten elucidar a función de onda de núcleos exóticos, entendida como a superposición de distintas configuracións $core \otimes nucleon$.

O interese nas reaccións de arranque dun neutrón naceu mediada a década dos oitenta, relacionado coa investigación das estruturas de halo. Os fragmentos $A - 1$ emerxentes amosaban distribucións de momento moi estreitas que reflectían a extensa distribución espacial asociada á configuración de halo do nucleón arrincado [Bau98]. Ademais, observáronse grandes seccións eficaces, que constituíron unha importante fonte de información complementaria.

As primeiras medidas coñécense como inclusivas xa que se basaban por completo na detección dos fragmentos producidos na reacción. Máis tarde, comprobouse que a suposición subxacente de que só se poboaba o estado fundamental do *core* resultaba inapropiada e pouco precisa, advertíndose a contribución de configuracións máis ligadas do proxectil. O uso de detectores de raios γ dou lugar ás chamadas medidas exclusivas, que permiten diferenciar os distintos estados do fragmento $A - 1$ e proporcionan unha imaxe máis realista da estrutura do poxectil [Aum00, Cor02, Mad01].

Co transcurso do tempo, os experimentos de *knockout* extendéronse do estudo de núcleos con halo a outras especies exóticas, investigándose maiormente núcleos lixeiros debido a limitacións técnicas relacionadas coa produción de feixes secundarios radioactivos. O momento de retroceso do fragmento producido na reacción conduce ao momento angular do nucleón arrincado e a medida dos raios γ emitidos en coincidencia permite determinar os coeficientes de ramificación e as seccións eficaces parciais correspondentes aos distintos estados do fragmento. Os resultados poden entón compararse coas predicións de modelos de partícula independente.

Durante moitos anos, NSCL [NSC] foi o laboratorio máis activo neste campo, traballando con núcleos ricos en neutróns a enerxías intermedias entre 50 e 150

¹A denominación *nucleon knockout* ten a súa orixe nas publicacións do laboratorio *National Superconducting Cyclotron Laboratory*, en Michigan, EEUU [NSC]. Trátase dun nome herdado de experimentos de dispersión case libre inducidos por protóns e neutróns, $(p, 2p)$ e $(e, e'p)$. Na literatura, este termo refírese normalmente a reaccións de natureza nuclear, mentres que os procesos electromagnéticos se designan como *Coulomb breakup*.

MeV/nucleón [Aum05, Gad08, Han03]. Este laboratorio foi ademais pioneiro no estudo de reaccións de *knockout* con núcleos máis pesados [Gad06b] e na realización de experimentos basados no arranque de dous neutróns [Baz03, Gad06a, Yon06]. Nun dominio enerxético semellante, a técnica de *knockout* emprégase tamén en GANIL, Francia, [GAN], [Sau04], mentres que o centro de investigación xaponés RIKEN [RIK] se centra no estudo de reaccións de ruptura inducidas electromagneticamente [Fuk04, Nak99]. O experimento descrito nesta tese levouse a cabo no GSI [GSI], en Alemaña, onde se teñen realizado experimentos de natureza tanto coulombiana [Noc05, Pal03, Pra03] coma nuclear [Bau98, Cor02, Cor04].

Os experimentos nos que se emprega a técnica de arranque dun neutrón ou *one-neutron knockout* requiren certa comprensión dos distintos mecanismos de reacción que poden contribuír. En particular, cando traballamos con brancos lixeiros² no réxime de alta enerxía, as chamadas reaccións de *stripping*, onde o neutrón de valencia é absorbido polo branco e só o *core* ten un parámetro de impacto suficientemente grande para evitar a colisión, dominan sobre as demais [Hen96]. Neste contexto, a distribución de momento do fragmento $A - 1$ pode identificarse coa distribución que tería o neutrón arrincado cando estaba no proxectil. Esta interpretación asume que o branco é “transparente” ao fragmento e coñécese como *límite transparente do modelo de Serber* [Ser47]. Sen embargo, a supervivencia do *core* require que a reacción sexa periférica, de xeito que esta técnica só permite acceder á parte máis externa da función de onda [Han96, Sme98].

Por outra banda, a compoñente do momento lonxitudinal á dirección de incidencia do proxectil vese menos afectada polo mecanismo de reacción cas compoñentes transversais. Este comportamento foi estudado desde as perspectivas experimental [Han95, Orr92] e teórica [Ber92, Sag94], concluíndose que a distribución lonxitudinal é unha sonda máis fiable da estrutura do proxectil. A partir da forma e anchura destas distribucións é posible identificar o momento angular orbital do neutrón arrincado na reacción e obter información sobre a súa función de onda. Este observable é ademais axeitado para o estudo de estruturas de halo xa que, de acordo co principio de incerteza de Heisenberg, a deslocalización espacial tradúcese nunha estreita distribución de momento [Kob88].

Desde o punto de vista experimental, é posible obter unha imaxe máis completa mediante a determinación da sección eficaz de arranque dun neutrón e o uso de detectores de raios γ , que nos proporcionan información espectroscópica.

²O feito de considerar brancos lixeiros, cun baixo número atómico, permítenos obviar as reaccións de natureza electromagnética.

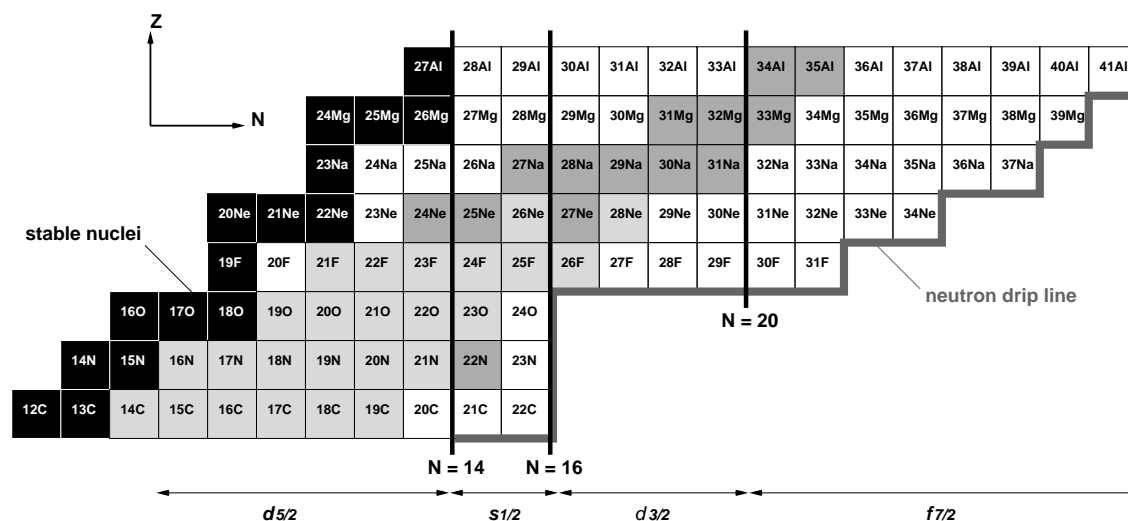


Figure 1: Rexión rica en neutróns da carta de núcleos. Os núcleos investigados neste experimento aparecen en tons grises. Os cadros máis escuros corresponden a aqueles casos que non foron estudados antes mediante reaccións de arranque dun neutrón. Indícase tamén a configuración de neutróns que predí o modelo de capas convencional.

Este experimento

O traballo descrito nesta tese tiña como obxectivo principal o estudo das propiedades de partícula independente de proxectís lixeiros ricos en neutróns, entendidos como a suma de distintas configuracións $core \otimes neutron$. Mediante reaccións de arranque dun neutrón, investigamos de forma sistemática o estado fundamental de trinta e nove isótopos diferentes situados entre C e Al. Así, puidemos realizar unha ampla sondaxe da rexión comprendida entre $N = 8$ e 22 da carta de núcleos.

O experimento realizouse no centro de investigación alemán *Gesellschaft für Schwerionenforschung* [GSI], en Darmstadt, entre os días 18 e 27 de abril de 2006. Empregouse un feixe primario de ^{40}Ar completamente ionizado, cunha intensidade de 10^{10} ións/pulso, que foi acelerado no UNILAC (2–20 MeV/nucleón) e ultra-acelerado no sincrotrón SIS para acadar unha enerxía de 700 MeV/nucleón e o 80 % da velocidade da luz no baleiro. Logo, os proxectís de interese obtivéronse mediante fragmentación nun branco de Be cun espesor de 4 g/cm^2 , situado na entrada do espectrómetro magnético FRS [Gei92].

A figura 2 amosa un esquema do dispositivo experimental. A primeira parte do FRS, F0–F2, adicouse á identificación e selección dos proxectís. O branco de reacción, Be cun espesor de 1720 mg/cm^2 , situouse no plano focal intermedio, F2. Nesta rexión, incluíuse ademais un conxunto de detectores de Ge cos que se mediron os raios γ emitidos en coincidencia, MINIBALL [Ebe01]. Os fragmentos producidos

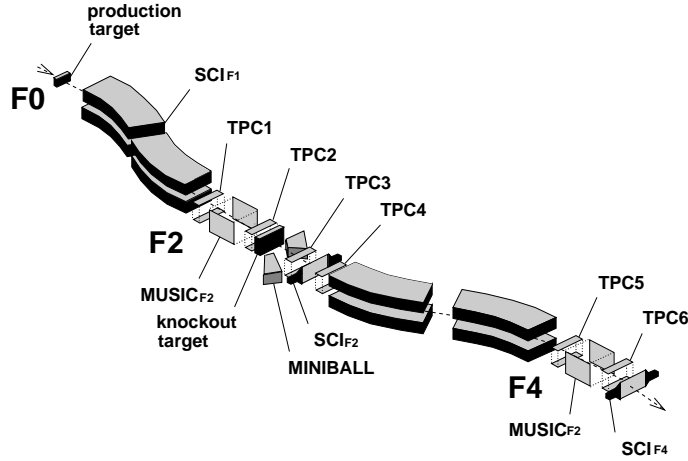


Figure 2: Dispositivo experimental no espectrómetro magnético FRS. A carga dos núcleos foi determinada en cámaras de ionización, MUSIC. As súas posicións medíronse nas TPCs e empregáronse os tempos de voo entre centelleadores, SCI_{F1}-SCI_{F2} e SCI_{F2}-SCI_{F4}, para medir as súas velocidades. Finalmente, MINIBALL permitiunos detectar os raios γ emitidos en coincidencia e identificar o estado dos fragmentos despois da reacción.

na reacción estudáronse na segunda metade do FRS, F2-F4. A identificación dos núcleos basouse na determinación da súa carga en cámaras de ionización, MUSIC [Pfü94], e na avaliación do cociente A/Q . Este último cálculo fíxose a partir de: (i) medidas de posición nas TPCs [Hli98], que nos permitiron calcular a rixidez magnética, $B\rho = \lambda m_0 \beta c / Q$, e (ii) os tempos de voo entre centelleadores, SCI_{F1}-SCI_{F2} e SCI_{F2}-SCI_{F3}, que nos proporcionaron a velocidade de cada núcleo.

Leváronse a cabo medidas inclusivas da distribución de momento lonxitudinal dos fragmentos $A - 1$ e da sección eficaz de arranque dun neutrón para un gran número de proxectís, a saber, $^{14-19}\text{C}$, $^{16-22}\text{N}$, $^{19-23}\text{O}$, $^{21-26}\text{F}$, $^{24-28}\text{Ne}$, $^{27-31}\text{Na}$, $^{31-33}\text{Mg}$ e $^{34-35}\text{Al}$. As medidas de momento realizadas para ^{14}C e ^{16}N víronse seriamente afectadas polos límites de aceptación do FRS e non foi posible determinar os valores de FWHM asociados. En canto ás seccións eficaces, entre as diversas correccións que lles aplicamos aos datos experimentais, foi importante dar conta de aquelas reaccións que non ocorreron no branco, senón nos materiais circundantes. Esta tarefa requiriu a realización de medidas específicas e só puido levarse a cabo nun determinado número de casos, $^{16-17}\text{C}$, $^{18-20}\text{N}$, $^{20-22}\text{O}$, $^{23-25}\text{F}$, $^{26-27}\text{Ne}$, $^{29-30}\text{Na}$ e $^{31-32}\text{Mg}$.

Por mor da gran cantidade de datos recollida neste experimento, a interpretación dos resultados inclusivos restrinxíuse a certas cadeas isotópicas e organizouse arredor dalgúns temas específicos:

- Resultados para $^{14-19}\text{C}$.
Discutimos a posibilidade dunha configuración de halo para o neutrón de va-

lencia dos isótopos de C cun número impar de neutróns, isto é, $^{15,17,19}\text{C}$. Os resultados que obtivemos para o ^{15}C parecen suxerir unha distribución espacial extendida. Pese a que a información recadada en anteriores experimentos de *knockout* apunta na mesma dirección, medidas contraditorias da sección eficaz de interacción total fan que a situación deste núcleo aínda se considere dubidosa. No caso do ^{17}C , contamos con medidas exclusivas que nos proporcionaron información adicional sobre a súa estrutura. O estado fundamental está dominado por unha compoñente $^{16}\text{C}(2^+) \otimes 1d_{5/2}$ que inhibe a formación dun halo. Por último, os observables inclusivos reflicten claramente a ben coñecida estrutura de halo do ^{19}C .

- Resultados para $^{16-22}\text{N}$, $^{19-23}\text{O}$ e $^{21-26}\text{F}$.
En todas estas cadeas isotópicas, observamos a transición entre as configuracións $1d_{5/2}$ e $2s_{1/2}$ cando se cruza $N = 14$, en bo acordo coas predicións do modelo de capas tradicional. Este traballo ofrece ademais os primeiros datos de *one-neutron knockout* para o ^{22}N , que amosa unha significativa compoñente $2s_{1/2}$. Sen embargo, non podemos resolver a cuestión plantexada na literatura en relación a unha posible distribución espacial extendida do neutrón de valencia [Oza00, Soh08]. Noutra orde de cousas, non se observou ningún efecto claro en relación ao cruce de $N = 16$ por parte do ^{26}F . En contra do agardado, os datos experimentais non parecen corresponder a unha configuración $1d_{3/2}$, senón que, como xa suxeriron Fernández *et al.* [Fer03], poderían indicar unha configuración distinta baseada nun neutrón de valencia $2s_{1/2}$ acoplado a un estado excitado do core ^{25}F .
- Resultados para $^{24-28}\text{Ne}$.
Tal e como ocorre para N, O e F, os isótopos de Ne amosan significativas contribucións $2s_{1/2}$ cando se cruza $N = 14$. Sen embargo, $^{27,28}\text{Ne}$, con $N = 17$ e 18 , non seguen a tendencia esperada. Lonxe de ocupar o nivel $1d_{3/2}$, o neutrón de valencia ocupa o nivel $2s_{1/2}$, acoplado a un estado excitado do core. Co fin de profundizar na estrutura dos proxectís $^{24-28}\text{Ne}$, servímonos dun sinxelo modelo teórico para analizar as distribucións de momento dos fragmentos $A - 1$. Os nosos cálculos teñen en conta o momento angular orbital do neutrón arrincado, a súa enerxía de separación e un parámetro de impacto mínimo que asegura a supervivencia do core no proceso de *knockout*. Asumimos ademais unha visión simplificada do estado fundamental do proxectil na que só se consideran dúas posibles configuracións *core* \otimes *neutron*. As conclusións ás que chegamos mediante esta descrición están en bo acordo cos resultados exclusivos obtidos por Terry *et al.* [Ter06] nun experimento anterior no que estudaron os núcleos $^{26,28}\text{Ne}$.

Utilizamos un conxunto de detectores de Ge segmentados, MINIBALL [Ebe01], para realizar medidas exclusivas. A estatística acumulada foi suficiente para estudar os raios γ emitidos en coincidencia co *knockout* de determinados proxectís, en

concreto, $^{15-17}\text{C}$, $^{17-20}\text{N}$, $^{20-22}\text{O}$ e $^{22-25}\text{F}$. No caso de ^{24}F , $^{20,22}\text{O}$ e $^{15,16}\text{C}$, non observamos ningún indicio de desexcitación dos fragmentos $A - 1$, probablemente porque aquelas reaccións onde se poboa directamente o seu estado fundamental dominan o proceso. Por outra banda, a moderada resolución dos nosos espectros impediu unha análise detallada de situacións complexas onde se observaron numerosos raios γ . En consecuencia, centrámonos na análise de catro casos máis simples, ^{17}C , ^{19}N , ^{21}O e ^{25}F , para os que determinamos os coeficientes de ramificación e as seccións eficaces parciais asociadas aos distintos estados do fragmento:

- Os raios γ medidos no *knockout* de ^{17}C suxiren a poboación do primeiro estado excitado do core ^{16}C , a 1766 keV, e dun grupo de tres niveis próximos a 4000 keV. Os datos exclusivos apoian o traballo de Maddalena *et al.* [Mad01], onde os autores atoparon unha probabilidade significativa de poboar o estado fundamental do core, en aparente contradición con cálculos teóricos. Nós chegamos a resultados semellantes que confirman as súas conclusións.
- En canto ao *knockout* de ^{19}N , tres niveis do core ^{18}N a baixas enerxías, 115, 588 e 747 keV, foron poboados na reacción³. De acordo coas coincidencias γ observadas, propuxemos un esquema de desexcitación para o ^{18}N que está en bo acordo co recente traballo de Wiedeking *et al.* [Wie08]. Aínda que non foi posible calcular os coeficientes de ramificación nin seccións eficaces asociadas, fomos capaces de determinar límites superiores e inferiores para os estados 2^- e 3^- do core a 588 e 747 keV, respectivamente.
- No *knockout* de ^{21}O , observáronse os dous primeiros estados excitados do core ^{20}O , a 1674 e 3570 keV. Os coeficientes de ramificación e as seccións eficaces que obtivemos amosan diferencias significativas respecto aos resultados de Fernández *et al.* [Fer03]. A baixa resolución das medidas levadas nese experimento podería explicar o desacordo cos nosos datos.
- No *knockout* de ^{25}F , pobouse o primeiro nivel excitado do core ^{24}F , a 522 keV. Calculáronse os coeficientes de ramificación e as seccións eficaces parciais.

En termos xerais, este traballo contribúe a unha mellor comprensión da zona rica en neutróns da carta nuclear. Os nosos datos poden analizarse xunto a experimentos anteriores, onde se investigaron maiormente núcleos lixeiros con número atómico $Z \leq 9$, co fin de obter unha visión máis sólida das distintas cadeas isotópicas. Ademais, as medidas realizadas para núcleos cun maior número de protóns, ata $Z = 13$, supoñen unha valiosa fonte de información nun dominio relativamente inexplorado ata o momento.

³O terceiro nivel excitado do ^{18}N , a 747 keV, foi identificado por primeira vez no traballo de Putt *et al.* [Put83]. Datos recentes de fusión-evaporación obtidos por Wiedeking *et al.*, sitúano a unha enerxía lixeiramente distinta, 742 keV [Wie08]. O noso espectro γ indica a súa localización a 730 ± 20 keV.

Chapter 1

Introduction

Much of our understanding about the structure of nuclear systems has developed without a detailed knowledge of the nuclear forces involved. In this context, the interplay between theory and experiments plays a fundamental role and nuclear reactions constitute a primary source of information. Today, different kinds of reactions are known and can be used by scientists to explore the structure of the atomic nucleus.

The first section of this introduction is a brief story about how the description of the nucleus evolved with the experimental observation, starting with the so-called liquid-drop and shell models. New phenomena appear when approaching exotic nuclei and require more complex explanations. Special attention will be given to the vicinity of the neutron drip-line, which is the focus of the work presented here.

Then, a few lines will be dedicated to describing the investigation of single-particle properties through direct reactions. Specifically, one-neutron knockout reactions, used in this experiment to investigate the evolution of shell structure, will be explained with more care. The zone between $N = 8$ and 22 was explored using this technique, facilitating the systematic study of different isotopes ranging from C to Al.

The last section will end with a general description of the work carried out and how it is distributed in the chapters of this dissertation.

1.1 Nuclear-structure studies

Until the mid-1960s, two descriptions of the nucleus had been proposed. The first one was called the *liquid-drop model* and dates from 1935. It was inspired by scattering experiments, which indicated an approximately constant nuclear density. The nucleus was described as an incompressible liquid drop made of nucleons that hold together by the strong nuclear force. Though a crude model, it explains the spheri-

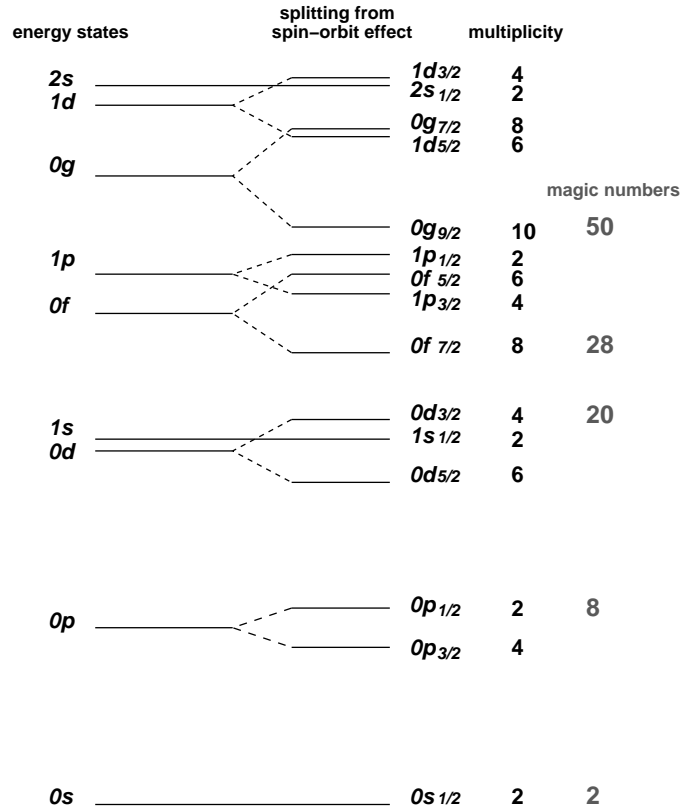


Figure 1.1: Low-lying energy levels in a single-particle shell model with oscillator potential. The magic numbers are related to a large energy gap between adjacent shells.

cal shape of most nuclei and the general trend of the binding energy with respect to the mass number [Wei35]. However, this description is not suitable for light nuclei, $A < 20$, and cannot explain effects such as the existence of magic numbers.

Measurements of nuclear binding energies revealed systematic deviations with respect to the predictions of the liquid-drop model. The observation of nuclei with certain proton and/or neutron numbers that appeared to be specially bound (magic numbers) suggested a shell structure of nucleons in the nucleus analogous to that of electrons in atoms. The model was considerably improved in 1949 by Mayer [May49] and Jensen [Hax49], who introduced a new term in the potential accounting for the spin-orbit interaction, see Fig. 1.1. In general, the *shell model* provides an excellent fit to the experimental data. Over time, it has evolved into a powerful calculation method that is suitable for solving some variants of the nuclear N-body problem¹.

¹The nuclear shell model was started by Mayer and Jensen in 1949 as a single-particle model. Afterwards, because of the need to include many valence particles, it became a many-body theory and evolved as a calculation method. The nucleus is understood as a non-relativistic quantum N-body system where the nucleons have no structure and only interact via two-body interactions.

Nuclear-structure studies have advanced on the basis of a well-established shell structure associated with certain magic numbers and have been predominantly carried out on stable nuclei, which can be well understood within this context. Nevertheless, in recent decades, the availability of fast radioactive beam facilities opened the door to experimental research far off β stability, allowing the investigation of nuclear properties at large charge asymmetry, large isospin and weak binding energies.

The high-energy regime (50 MeV/nucleon–1 GeV/nucleon) has important experimental and theoretical advantages. It is possible to increase the thickness of the targets and moderate the size of the detectors due to the kinematical forward focusing. Short interaction times and small scattering angles also allow the use of key approximations in the description of the underlying reaction mechanisms.

Experimental research with relativistic radioactive beams began in 1979 at Lawrence Berkeley Laboratory, in California, USA, [Ber], [Sym79, Wes79]. A few years later, important results on nuclear structure emerged from this laboratory, where Tanihata and collaborators determined the radius of ${}^6\text{--}11\text{Li}$ and ${}^7\text{--}10\text{Be}$ isotopes from interaction cross-section measurements [Tan85]. ${}^{11}\text{Li}$ showed a remarkably large radius, which was later explained as a low-density tail in the wave function of the valence neutrons. Such a state is now known as a *nuclear halo* [Han87], in reference to the weakly bound nucleon or nucleons that form a low-density cloud around a central core. Since then, several halo nuclei, namely, ${}^6\text{He}$, ${}^8\text{He}$, ${}^{11}\text{Be}$, ${}^{14}\text{Be}$, ${}^{17}\text{B}$ and ${}^{19}\text{C}$, have been discovered near the neutron drip-line and new candidates have been suggested. One such case is ${}^{22}\text{N}$, for which an extended spatial distribution of the $s_{1/2}$ neutron state has been proposed [Oza00]. Recent experimental data from in-beam γ -ray spectroscopy could support this hypothesis [Soh08].

The evolution of the shell structure shows other interesting phenomena when moving away from the valley of β stability. Experiments have revealed important differences with respect to the magic numbers established for stable nuclei. Some examples are the vanishing of the $N = 8$ closed neutron shell for ${}^{12}\text{Be}$ [Iwa00a, Iwa00b] or the appearance of new sub-shell closures at $N = 14$ and 16 for oxygen isotopes [Kan09, Oza00, Sta04]. Otsuka and collaborators [Ots01b] suggested that the nucleon-nucleon interaction, which changes when adding or removing nucleons, could be responsible for this enhancement of the energy gap at $N = 16$. The non-occupation of the $d_{5/2}$ proton level would cause the $d_{3/2}$ neutron orbit to be pushed up close to the pf shell and a new gap would appear at $N = 16$, to the detriment of the traditional $N = 20$ magic number.

Unusual shell structures have also been found for neutron-rich nuclei with $N \sim 20$. This effect was first discovered in 1975, when mass measurements of ${}^{31,32}\text{Na}$ indicated non-spherical shapes and disagreed with the conventional shell closure at

$N = 20$ [Thi75]. Later on, further evidence of an onset of deformation emerged for ^{32}Mg [Mot95] and ^{30}Ne [Yan03]. This area is commonly known as the *island of inversion* because the ground state is believed to consist of intruder configurations with neutrons excited from the *sd* to the *pf* shell. Studies to define the edges of this region are still going on [Him08].

1.2 Exploring single-particle properties through direct reactions

Direct reactions such as transfer or quasi-free scattering were extensively used in the past to investigate the single-particle properties of stable nuclei. Among them, mainly transfer reactions, in which one or more nucleons are exchanged between the projectile and the target, have been applied to radioactive beams [Cat05b, Fer07, Gau06, Gau08, Win01]. The typical cross-sections in these experiments are about 1 mb and the optimum beam energies vary between 10 and 20 MeV/nucleon. The use of a magnetic spectrometer makes it possible to distinguish the final state of the residue and the angular momentum of the transferred nucleon can be obtained by measuring the angular distribution, leading to the identification of single-particle configurations.

However, it must be noted that transfer experiments with exotic nuclei have only been possible for the last few years and alternative techniques suitable for high-energy, low-intensity secondary beams have been developed. This is the case with breakup reactions, whose cross-sections are enhanced from 1 to 100 mb when moving from tight to weakly bound nuclei. The nature of the interaction can be either nuclear or electromagnetic, depending on the charge of the target and the energy regime. Within this context, early one-nucleon removal measurements evolved into the *single-nucleon knockout* technique, which has become a reliable tool for obtaining basic information on shell structure and clarifying the wave function of exotic nuclei, understood as a superposition of different *core* \otimes *nucleon* configurations. The term ‘nucleon knockout’ was adopted in publications from the National Superconducting Cyclotron Laboratory, in Michigan, USA [NSC]. In the literature, it usually refers to nuclear reactions, while electromagnetic processes induced by heavy targets are designated as *Coulomb breakup*. The knockout name was inherited from former quasi-free scattering experiments induced by protons and electrons, $(p,2p)$ and $(e,e'p)$, which were regarded as powerful spectroscopic tools [Kra01, Pan97].

Interest in one-neutron knockout reactions was triggered by the study of halo nuclei in the mid-1980s. The emerging $A - 1$ core fragments exhibited narrow momentum distributions that clearly reflected the extended spatial distribution of the halo [Bau98]. Large cross-sections were also measured, providing a complementary source of structural information.

Early measurements were called *inclusive* since they were entirely based on the detection of the core fragments. Later on, the underlying assumption that only the ground state of the core was populated in the reaction turned out to be inaccurate. Although contributions from more deeply bound configurations in the projectile are expected to be small for a halo nucleus, they can be observed in the tails of the momentum distributions. The use of γ -ray detectors gave rise to *exclusive* measurements that made it possible to distinguish between different states of the $A - 1$ fragment and provide a more realistic picture of the projectile structure [Aum00, Cor02, Mad01].

With time, knockout experiments have extended from halo nuclei to other exotic species. By means of γ coincidences, the states populated in the $A - 1$ nucleus can be identified and measurement of the fragment recoil momentum can provide the angular momentum of the removed nucleon. Branching ratios and partial cross-sections can be calculated and compared with single-particle calculations.

Due to technical limitations related to the production of secondary beams, knockout investigations have concentrated on the light region of the nuclear landscape and have only recently been extended to heavier nuclei. For many years, NSCL [NSC] has been the most active laboratory in this field, focusing on the study of neutron-rich nuclei at intermediate energies between 50 and 150 MeV/nucleon [Aum05, Gad08, Han03]. Knockout measurements for heavier nuclei [Gad06b] and studies concerning the removal of two nucleons have recently begun there [Baz03, Gad06a, Yon06]. The knockout technique has also been applied in a similar energetic domain at GANIL [GAN], [Sau04], in France, while the Japanese research centre RIKEN [RIK] has focused on the study of Coulomb-induced breakup [Fuk04, Nak99]. The experiment described in this dissertation was performed at GSI [GSI], in Germany, where several experiments on both Coulomb [Noc05, Pal03, Pra03] and nuclear breakup [Bau98, Cor02, Cor04] have been carried out.

The interpretation and understanding of the one-neutron knockout technique requires certain knowledge of the reaction mechanisms that may contribute to the one-neutron removal channel. The following cases can be identified:

- **Coulomb breakup** is caused by high-energy photons created in the quickly changing electric field of the target nucleus seen by the projectile. The probability of Coulomb breakup is proportional to the square of the target charge and can therefore be neglected when working with light targets such as Be, which was used in this experiment.
- **Diffraction breakup** represents the excitation to continuum nucleon-core states and the consequent projectile dissociation. Two particles are expected in the final state, as shown in Fig. 1.2.

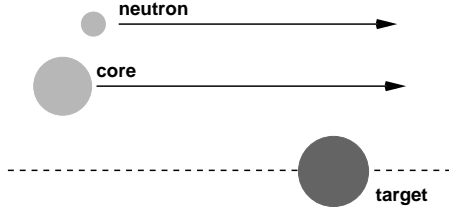


Figure 1.2: Diffractive breakup.

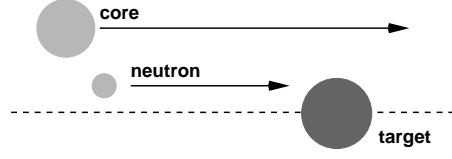


Figure 1.3: Neutron stripping.

- **Neutron stripping** occurs when the valence neutron is absorbed by the target. Only the impact parameter of the core, which is the sole particle in the final state, is large enough to avoid the collision, see Fig. 1.3.

Stripping reactions dominate in the high-energy regime [Hen96]. Within this context, the momentum distribution of the observed core fragment is identified with the ground-state distribution of the removed nucleon inside the projectile nucleus. This interpretation assumes that the target is *transparent* to the core fragment and is commonly known as the *transparent limit of the Serber model* [Ser47]. However, the core survival implies a lower cut-off on the impact parameter, so that only the outer part of the wave function is sampled using this technique [Han96, Sme98].

Experiments have suggested that momentum components transverse to the beam direction are much more affected by the reaction mechanism than the longitudinal one [Han95, Orr92]. Theory supports this conclusion and the longitudinal-momentum distribution is regarded as a better way of exploring the projectile structure [Ber92, Sag94]. Its sensitivity to the orbital angular momentum of the removed nucleon makes it a valuable observable for nuclear-structure investigation.

Since only the core fragment is detected in the experiments, diffractive breakup and stripping are usually considered in the calculation of single-particle cross-sections, $\sigma_{sp} = \sigma_{sp}^{diff} + \sigma_{sp}^{str}$. Eqs. 1.1 and 1.2 show how both contributions can be computed as integrals on the impact parameter [Tos99].

$$\sigma_{sp}^{diff} = \frac{1}{2J+1} \int d\mathbf{b} \left[\sum_M \langle \phi_{JM}^c | (1 - S_c S_n)^2 | \phi_{JM}^c \rangle \right] - \frac{1}{2J+1} \int d\mathbf{b} \left[\sum_{M,M'} |\langle \phi_{JM'}^c | (1 - S_c S_n) | \phi_{JM}^c \rangle|^2 \right] \quad (1.1)$$

$$\sigma_{sp}^{str} = \frac{1}{2J+1} \int d\mathbf{b} \sum_M \langle \phi_{JM}^c | (1 - |S_n|^2) |S_c|^2 | \phi_{JM}^c \rangle \quad (1.2)$$

The function $|\phi_{JM}^c\rangle$ represents the neutron with quantum numbers (nlj) moving with respect to the core in the $c \equiv I^\pi$ state and $\mathbf{J} = \mathbf{I} + \mathbf{j}$. S_c and S_n are the

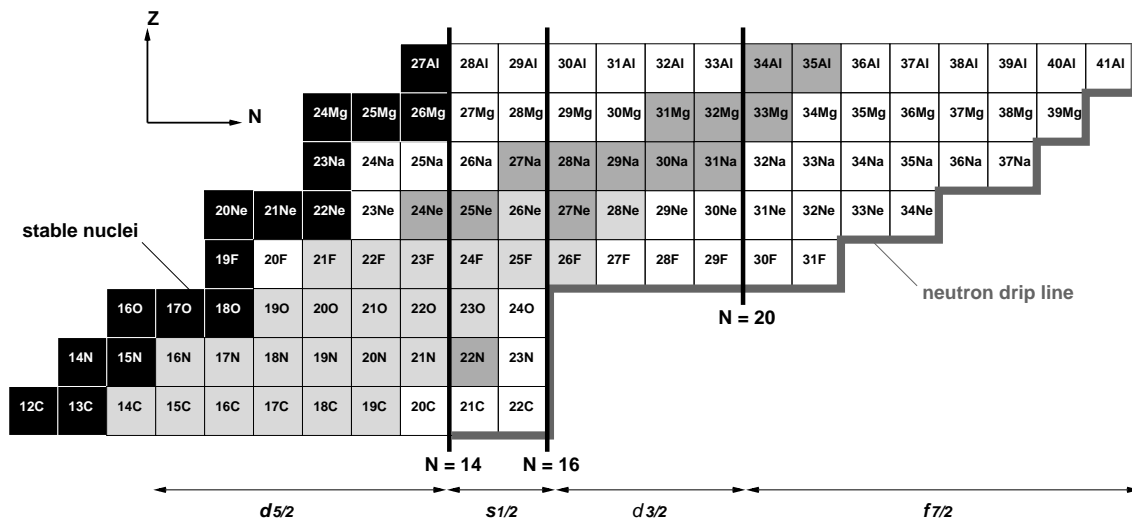


Figure 1.4: Light neutron-rich region of the nuclear landscape. The nuclei studied in this work are distinguished with shades of grey. The darkest grey squares represent cases that had not been previously studied with one-neutron knockout reactions. The neutron levels expected according to the conventional shell model are also indicated.

S -matrices for core and neutron scattering.

The cross-section for populating a given final state I^π of the core would be obtained from Eq. 1.3 as the contribution of the different single-particle states.

$$\sigma(I^\pi) = \sum_j C^2 S(I^\pi, nlj) \sigma_{sp}(I^\pi, nlj) \quad (1.3)$$

By measuring the γ rays emitted by the core fragment after the reaction, it would be possible to determine the branching ratio to each single-particle state and the corresponding spectroscopic factor, $C^2 S(I^\pi, nlj)$.

1.3 This work

One-neutron knockout reactions have been used in this work to explore the evolution of the nuclear structure close to the neutron drip-line. Thirty-nine different isotopes, ranging from C to Al, have been studied and the region between $N = 8$ and 22 has been closely examined. Fig. 1.4 displays the location of these nuclei within the nuclear landscape.

The experiment was performed April 18–27, 2006, at *Gesellschaft für Schwerionenforschung* [GSI], in Darmstadt, Germany. We worked with high beam energies around 700 MeV/nucleon and made use of the FRS two-stage magnetic spectrometer [Gei92]. The MINIBALL array was also included in the setup for coincident

γ -ray detection [Ebe01]. In the weeks prior to our investigation, the same experimental arrangement was used for one-neutron knockout studies on ^{56}Ti , yielding the first knockout measurements for medium-mass nuclei, $A \sim 50$, at relativistic energies. The analysis of those data was carried out at *Technische Universität München* [TUM] by Maierbeck and collaborators [Mai09].

The experimental details will be given in Chapter 2. Then, the first steps of the analysis: the calibration of the different detectors, the efficiency calculations and the determination of some other relevant parameters, will be explained in Chapter 3. Chapter 4 will be devoted to the one-neutron knockout observables, beginning with the selection of the reaction channel. Three physical magnitudes were used to obtain information about the investigated nuclei, namely:

- The longitudinal-momentum distribution of the one-neutron knockout fragment.
- The inclusive one-neutron knockout cross-section.
- The exclusive one-neutron knockout cross-sections and branching ratios to the different I^π fragment states.

The results of this work will be discussed and contextualised in Chapter 5, followed by the conclusions.

Chapter 2

The experiment

In April 2006, a one-neutron knockout experiment was performed at *Gesellschaft für Schwerionenforschung* [GSI], in Darmstadt, Germany. The main goal of this experiment was to explore the structural properties of light, neutron-rich nuclei in an extended region between C and Al. The experimental technique involved the study of one-neutron knockout reactions in a Be target using exotic neutron-rich projectiles that were produced by fragmentation of a primary beam. We benefited from the relativistic exotic beams available at GSI, since the high velocities allowed for a clean extraction of the physical observables and facilitated the interpretation of the results.

In this chapter, we will explain the characteristics of the setup and the different detectors. We started with a ^{40}Ar primary beam which was accelerated in the UNILAC (2–20 MeV/nucleon) and then ultra-accelerated in the SIS heavy ion synchrotron, reaching 700 MeV/nucleon (80 % of the velocity of light in vacuum). The mean intensity of the primary beam was around 10^{10} ions/spill, for spills produced within a 10 s period and a length fluctuating between 4 and 6 s.

Afterwards, the Ar primary beam was driven to a 4 g/cm^2 Be target where, via fragmentation reactions, a cocktail of exotic projectiles was produced. They were selected and identified in the first half of the Fragment Separator, FRS [Gei92]. The one-neutron knockout reaction took place in a 1720 mg/cm^2 Be target located at the intermediate focal plane and the resulting fragments were studied in the second half of the FRS. Fig. 2.1 shows a schematic view of the GSI-FRS facility.

2.1 The Fragment Separator

The Fragment Separator, FRS [Gei92], was designed for research and applied studies with relativistic heavy-ion beams. It is a high-resolution forward spectrometer with a nominal momentum resolving power of 1500 and an emittance of $20\pi\text{ mm}\cdot\text{mrad}$, where it is possible to analyse heavy ions with magnetic rigidities ranging from 5 to

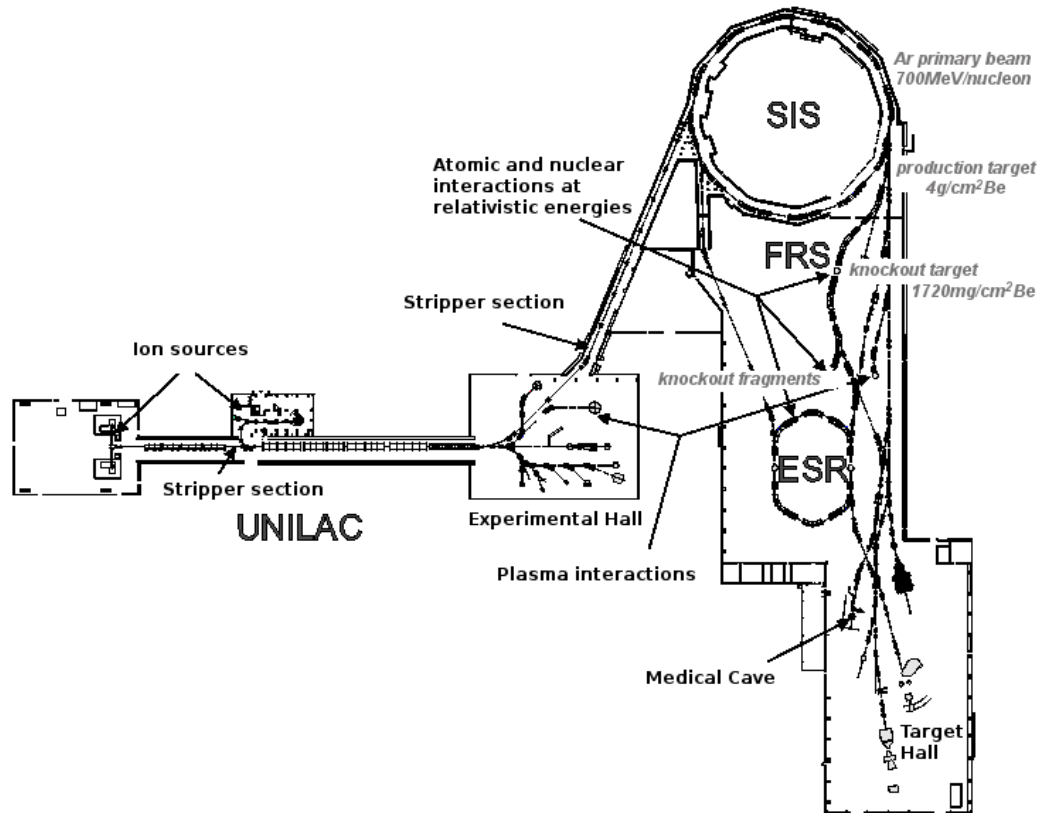


Figure 2.1: GSI facilities, in Darmstadt, Germany. *Italic characters refer to the one-neutron knockout experiment that will be described throughout this dissertation.*

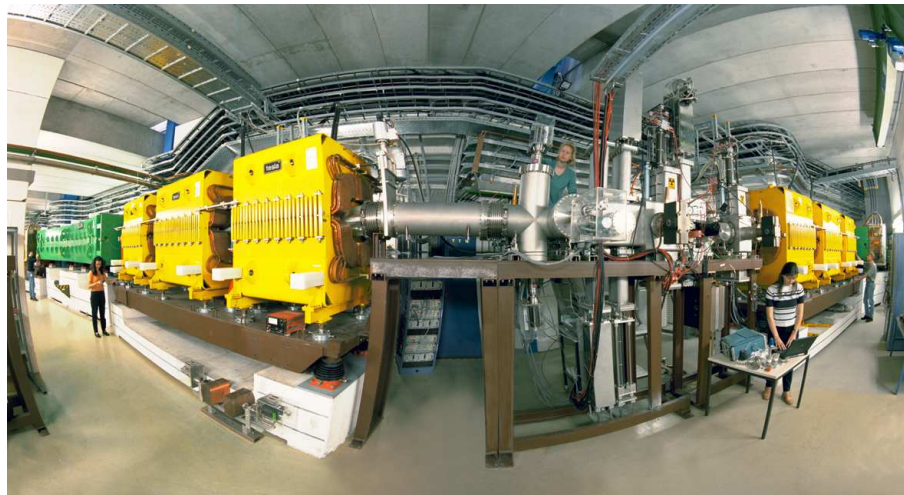


Figure 2.2: Photograph of the Fragment Separator, FRS, at GSI.

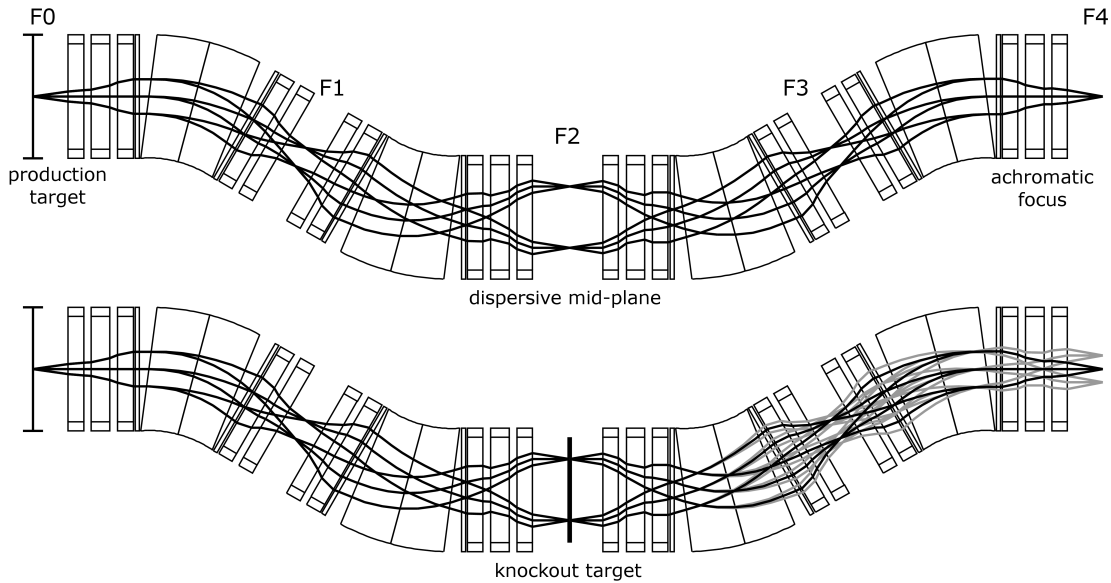


Figure 2.3: (Top) FRS working as an achromatic system with a dispersive mid-plane. Nuclei with three angles and two different magnetic rigidities are represented. The two values of the magnetic rigidity are separated at the mid-plane, F2, and focussed back at the final focal plane, F4. (Bottom) The momentum change induced by the knockout target is translated into a position difference at the final focal plane. (*Figure adapted from Baumann PhD dissertation [Bau99]*).

18 Tm.

The FRS is composed of four independent stages, each consisting of a dipole magnet and a set of quadrupoles placed before and after the dipoles. The quadrupoles provide proper illumination of the field volume of the bending magnets and determine the focusing ion-optical conditions at the focal planes. Sextupoles are also used to correct for second-order aberrations. A photograph of the FRS is displayed in Fig. 2.2.

2.1.1 The energy-loss mode

In this experiment, the FRS was operated in the energy-loss mode. We distinguish two different stages in the spectrometer, F0–F2 and F2–F4, with F0 referring to the position of the production target and F_i , $i = 1–4$, to the four FRS focal planes. Each stage is itself dispersive, but the combination of both constitutes an achromatic system that drives nuclei to the same point at the final focal plane, F4, independently of their initial momentum and charge.

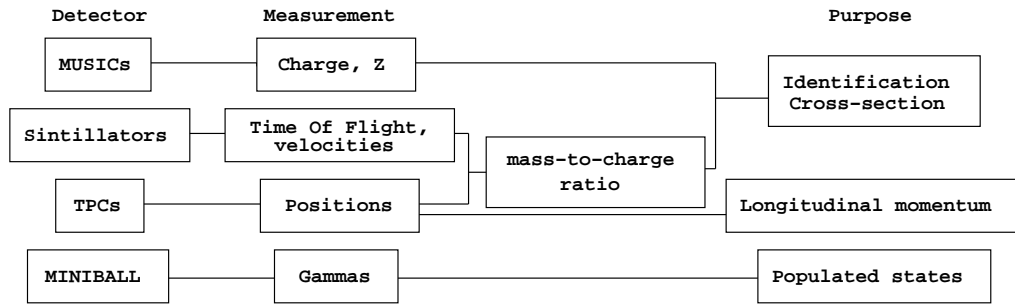


Figure 2.4: Measurements performed with the different detectors. The charges of the nuclei were determined with MUSICs. Their velocities were obtained from time-of-flight measurements provided by the scintillators and their positions at the intermediate and final focal planes were given by TPCs. With this information, the nuclei involved in the reaction were unambiguously identified and the one-neutron knockout cross-section was calculated. The positions identified by the TPCs were also used to determine the longitudinal momentum of the knockout fragments. Finally, MINIBALL measured the γ rays emitted in coincidence with the reaction, making it possible to distinguish between the populated fragment states.

The working principle is illustrated in Fig. 2.3. If we insert a target at F2, the momentum change that it produces will be reflected in a position difference at the final focal plane. This technique is described in Ref. [Gei92] and was successfully used in previous knockout experiments [Bau99]. The momentum change induced by the knockout reaction can be precisely determined from the simple measurement of the position at F4.

However, the detectors included at the mid-plane region, F2, represented a significant amount of matter that disturbed the optical system, which could no longer be considered achromatic. The fact that we studied different nuclei in a single set of measurements also complicated the procedure. As a consequence, the position at F4 was insufficient to correctly determine the momentum of the knockout fragments, thus we rigorously followed the optic transfer matrices of the system, using the complete equations derived from them. In Chapter 4, we will explain the details related to the momentum calculation.

2.2 The detector setup

Our measurements were concerned with the determination of the charges, velocities and positions of the nuclei involved in the one-neutron knockout reaction. Identification of the projectiles and one-neutron knockout fragments was based on the charge and mass-to-charge ratio, which allowed an unambiguous selection of the reaction channel. We determined the cross-section of the one-neutron knockout process and the longitudinal-momentum distribution of the produced fragments as well. The setup also included a γ detector in the target region, MINIBALL, which provided

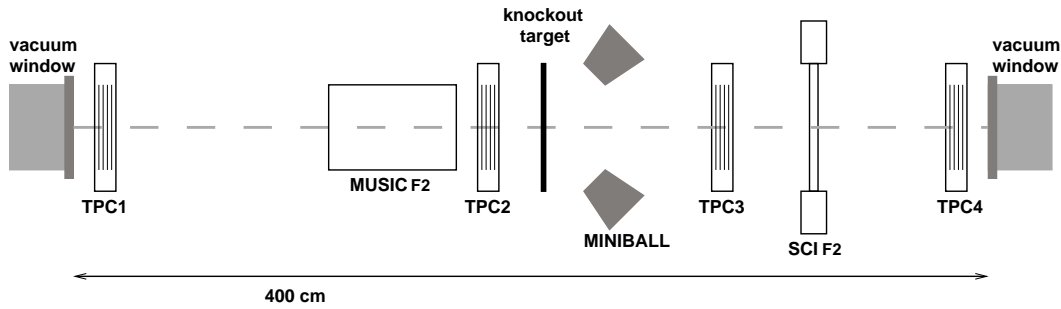


Figure 2.5: Schematic view of the detector setup at the intermediate focal plane, F2.

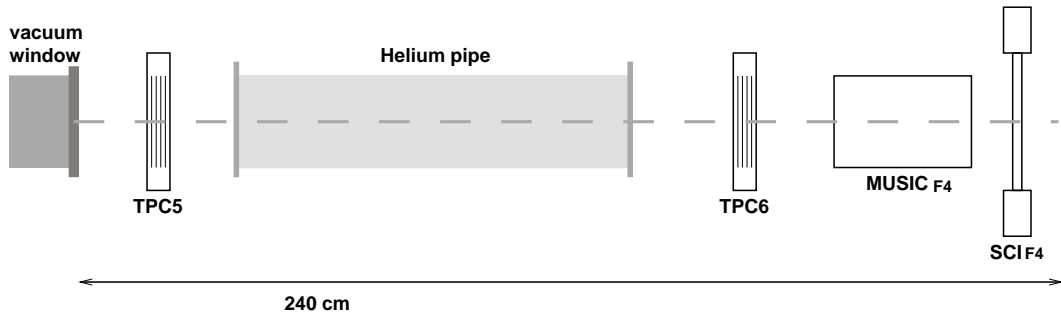


Figure 2.6: Schematic view of the detector setup at the final focal plane, F4.

information about the γ rays emitted by the knockout fragments and informed on the different states populated in the reaction.

In the following pages, we will explain the characteristics of the different detectors used in this experiment: MUSIC (Multiple-Sample Ionisation Chamber), SCI (Scintillator), TPC (Time-Projection Chamber) and MINIBALL. The measurements performed with them are summarised in Fig. 2.4. The detectors were concentrated at the intermediate and final focal planes of the FRS and arranged as shown in Figs. 2.5 and 2.6.

2.2.1 Multiple-sample ionisation chambers

The charges of the exotic projectiles and one-neutron knockout fragments were determined using two multiple-sample ionisation chambers, known as MUSICs [Pfü94] and located at F2 and F4, by measuring energy deposition in the gas volume of the detectors. Both MUSICs were filled with CF_4 gas. They had an active area of $200 \times 80 \text{ mm}^2$ and eight anodes whose signals were averaged to obtain the charge information.

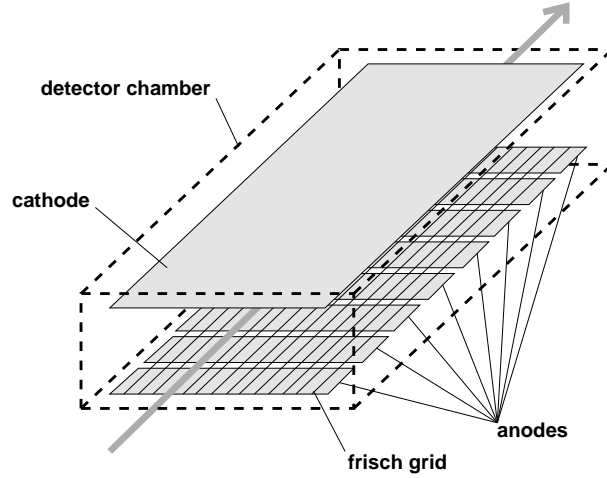


Figure 2.7: Schematic view of a multiple-sample ionisation chamber (MUSIC).

The working principle of a MUSIC is the detection of the electrons created when an ionising particle penetrates the chamber and loses part of its energy in the filling gas. The specific energy loss of charged particles in a material was described by Bethe in Eq. 2.1,

$$\frac{-dE}{ds} = \frac{4\pi Z_p^2}{m_e c^2 \beta^2} \left(\frac{e^2}{4\pi\epsilon_0} \right)^2 Z_t N_t \left(\ln \frac{2m_e v^2}{I} - \ln(1 - \beta^2) - \beta^2 \right) \quad (2.1)$$

where s represents the path length of the particle in the absorber, Z_p and β correspond to the charge and the velocity of the penetrating particle and Z_t , N_t and I are the proton number, the particle density and the mean excitation energy of the material, respectively. Finally, e and m_e are the charge and mass of the electron.

According to the previous formula, the number of electrons released in the gas is, at a first approximation, proportional to the square of the charge of the penetrating particle. In the electric field of the chamber, the electrons drift towards the anodes and charge-sensitive preamplifiers convert their charge into a proportional signal amplitude, see Fig. 2.7.

However, it should be noted that the ionisation in the detector gas is not directly related to the energy loss, but to the energy deposition, which can differ from each other due to the fact that δ rays can be produced. These energetic electrons can create more ions or leave the active volume of the detector, making the energy deposited smaller than the energy loss in the latter case. This reduction depends on the detector geometry and was described by Pfützner *et al.* [Pfü94] with the *truncated Bethe-Bohr model*, represented by Eq. 2.2.

$$\Delta = s \frac{4\pi Z_p^2}{m_e c^2 \beta^2} \left(\frac{e^2}{4\pi\epsilon_0} \right)^2 Z_t N_t \left(\frac{1}{2} \ln \frac{E_M E_d}{I^2} - \beta^2 \right) \quad (2.2)$$

Here, Δ is the mean energy deposition in the detector, s names the active length of the gas volume, E_M is the maximum energy that can be transferred to an electron in a single collision and E_d is an empirical parameter that depends on the dimensions of the absorber.

2.2.2 Scintillators

Scintillation is a luminescence process whereby light of a characteristic spectrum is emitted following the absorption of radiation. Different materials with this property are used in many physics research applications to detect electromagnetic waves or particles. A scintillator converts the energy deposited by the penetrating particle into light of a wavelength that can be detected by easy-to-handle detectors such as photomultiplier tubes, which convert the light pulse into an electric pulse.

The scintillators, or SCI, were used as time detectors to register the passage of the particles. We included three BC400 plastic scintillators in our setup, located at F1, F2 and F4. By knowing their exact locations and measuring the time differences between them, it was possible to determine the time of flight and the velocity of the nuclei.

The detector dimensions were $50 \times 60 \times 5 \text{ mm}^3$ (SCI_{F1}), $360 \times 40 \times 3.5 \text{ mm}^3$ (SCI_{F2}) and $360 \times 40 \times 4 \text{ mm}^3$ (SCI_{F4}). Each scintillator had photomultiplier modules on both sides. Those linked to SCI_{F1} corresponded to the H1949-50 model and were designed to withstand high counting rates; their main characteristics can be found in Ref. [PMT]. Even though it was not used during this experiment, the presence of a signal at each extreme of the scintillator made it possible to obtain position information concerning the y coordinate for SCI_{F1} , which was vertically oriented, and the x coordinate for SCI_{F2} and SCI_{F4} , oriented horizontally.

2.2.3 Time-projection chambers

Time-projection chambers, TPC [Hli98], were used for horizontal and vertical position measurements. The resolution of these detectors is around a few hundred microns and fulfilled the experimental requirements. We mounted six TPCs along the Fragment Separator: four were placed at the intermediate focal plane, F2, two of which were in front of the knockout target and two behind it. The fifth and sixth TPCs were placed at F4. All the detectors were filled with Ar gas, but the dimensions of the active volumes differed a bit. Following the beam direction, we had:

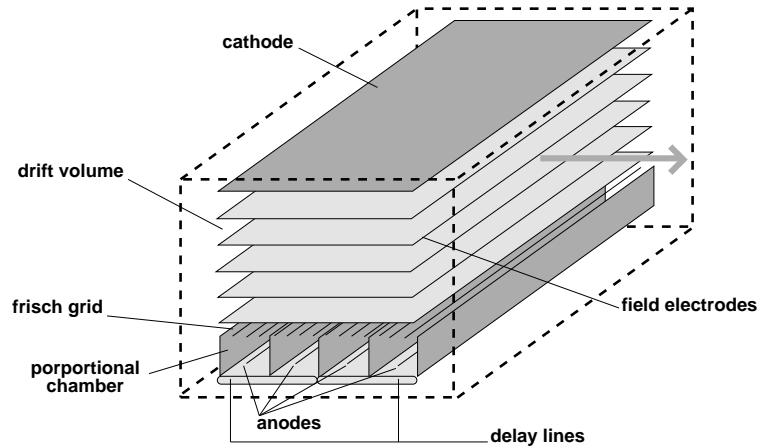


Figure 2.8: Schematic view of a time-projection chamber. The TPCs used in this experiment had two delay lines, each one covering a pair of anodes.

- TPC1: $240 \times 80 \times 110 \text{ mm}^3$
- TPC2: $240 \times 60 \times 110 \text{ mm}^3$
- TPC3: $240 \times 60 \times 110 \text{ mm}^3$
- TPC4: $240 \times 80 \times 110 \text{ mm}^3$
- TPC5: $240 \times 60 \times 110 \text{ mm}^3$
- TPC6: $240 \times 60 \times 110 \text{ mm}^3$

TPCs consist of a gaseous drift space in a uniform electric field applied in the vertical direction, see Fig. 2.8. An ionising particle passing through the detector creates a shower of electrons along its track that drift towards the proportional chambers surrounding each anode wire. The electron drift times provide a measurement of the y coordinate.

The x coordinate is recorded by a delay line below the anodes. The signal induced in the delay line spreads to both ends and the x coordinate is determined from the time difference between the arrival of the signals at the left and right extremes.

The above time measurements were performed in the common-stop mode, with the *start* signal coming from the TPC and the *stop* signal, which was used as a time reference, given by a plastic scintillator.

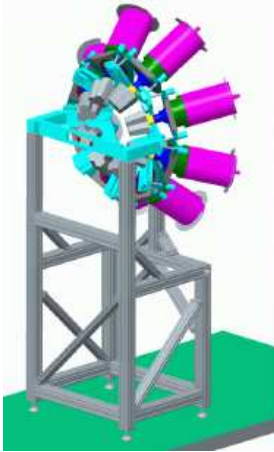


Figure 2.9: Schematic view of MINIBALL. It is composed of eight different clusters of segmented Ge detectors.

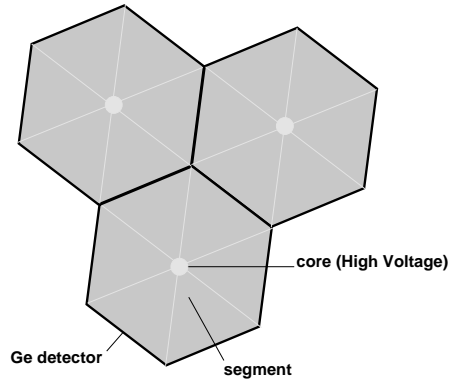


Figure 2.10: Zoom of one MINIBALL cluster, composed of three Ge detectors segmented into six different parts.

2.2.4 MINIBALL

The MINIBALL detector [Ebe01] was used to measure the γ rays emitted in coincidence with the one-neutron knockout reaction. This information allowed us to disentangle the different fragment states that were populated in the process.

MINIBALL is a highly efficient γ detector suited for work with low-intensity radioactive beams. It consists of modular clusters made up of independent, high-purity Ge detectors. Each cluster is formed by three Ge crystals segmented into six different parts, providing a granularity which is absolutely necessary for performing the Doppler correction of the γ rays emitted by a relativistic nucleus. Schematic views can be found in Figs. 2.9 and 2.10.

New encapsulated Ge detector technology was used in the MINIBALL array, where each module is kept under ultra-high vacuum conditions in a thin-walled aluminium can, so that the single detectors of a cluster can be easily replaced and the malfunction of one of them would not influence the others.

In this experiment, we used the eight available MINIBALL clusters arranged in a ring that surrounded the Be knockout target at F2, see Fig. 2.5, with an average distance of 24.6 cm with respect to the target centre and an average azimuthal angle of 40° with respect to the beam axis.

Chapter 3

Data analysis

The first sections of this chapter will be dedicated to the calibration procedures used to translate the raw data recorded by the different detectors into physical information. A few critical issues will also be addressed here, such as the partial malfunctioning of the TPCs at the intermediate focus and the tracking procedure developed to overcome this problem.

We will also describe the determination of important parameters for later evaluation of the longitudinal momentum of the knockout fragments, namely, the dispersion through the Fragment Separator and the exact location of the final focal plane. These concepts, related to the optics of charged particles [Car87], are explained in Appendix A together with the associated formulas that will appear in this chapter.

The final section will focus on the MINIBALL detector and the γ measurements performed in this experiment.

3.1 MUSIC calibration

The purpose of the MUSIC calibration was to obtain, from the signals collected in the anodes, the charge of the particle penetrating the detector. The MUSICS utilised in this experiment had eight anodes, each giving an individual energy signal. We used the geometric average of them all, dE_{raw} , as calculated in Eq. 3.1.

$$dE_{raw} = (e_1 \cdot e_2 \cdot e_3 \cdot e_4 \cdot e_5 \cdot e_6 \cdot e_7 \cdot e_8)^{1/8} \quad (3.1)$$

The variable e_i refers to the signal provided by the anode i , $i = 1-8$, after subtracting a certain offset that shifted the signals from the different anodes to a similar channel number.

However, the energy that a particle deposits in the MUSIC also depends on its velocity. To account for this effect, we measured dE_{raw} with a ^{48}Ca primary beam

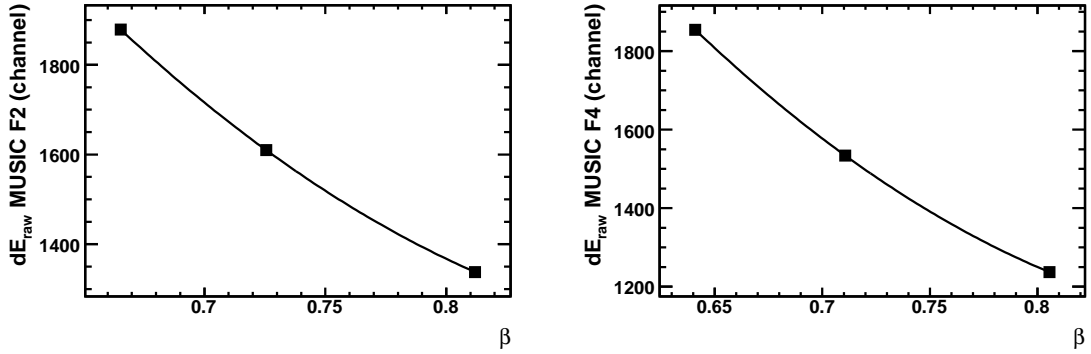


Figure 3.1: Velocity correction for the MUSICs placed at F2 and F4. The solid line represents the fit to a second-order polynomial that was used to obtain the coefficients of Eq. 3.2.

at three different energies, 350, 452 and 690 MeV/nucleon. For each energy, we evaluated the velocity in the regions F1–F2 and F2–F4 using MOCADI [Iwa97], a Monte Carlo simulation program specifically developed for the FRS. The dE_{raw} data obtained from the MUSICs at F2 and F4 were afterwards studied as a function of the velocity, as shown in Fig. 3.1. They were then fitted to a second-order polynomial and the velocity correction was performed according to the function of Eq. 3.2,

$$Corr_{\beta} = a_0 + a_1\beta + a_2\beta^2 \quad (3.2)$$

where β represents the velocity of the particle.

Once this correction was applied to the dE_{raw} signals, the charge of the particle was determined as follows:

$$Z_{signal} = \sqrt{\frac{dE_{raw}}{Corr_{\beta}}} \quad (3.3)$$

The final MUSIC calibration is shown in Fig. 3.2, where we identified the values of Z_{signal} for several elements. From the linear relation between Z_{signal} and the atomic number, Z , we obtained the appropriate parameters of the calibration function, written in Eq. 3.4.

$$Z = b_0 + b_1 \cdot Z_{signal} \quad (3.4)$$

3.2 Time-of-flight calibration

We calculated the time of flight, TOF, through the FRS from the time difference between the signals given by scintillators SCI_{F1} , SCI_{F2} and SCI_{F4} . In particular, we measured TOF_{F1F2} and TOF_{F2F4} and deduced from them the velocities of the

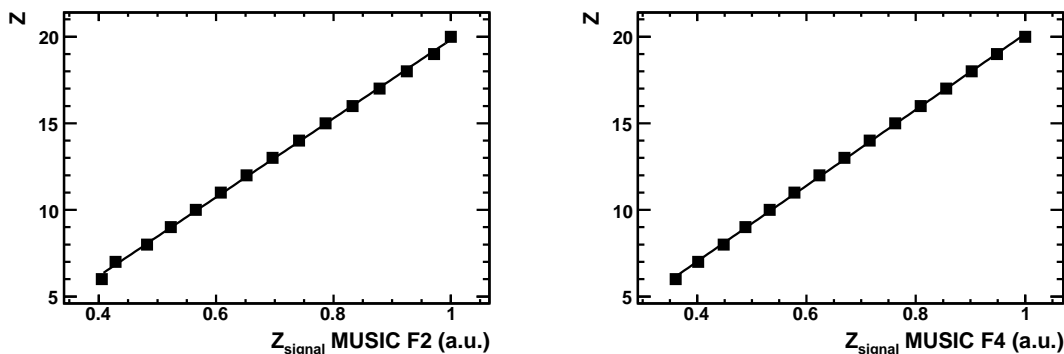


Figure 3.2: Final calibration plots for the MUSICs at F2 and F4.

projectiles and one-neutron knockout fragments assuming that the distances travelled from one plastic to another were constant.

The scintillators had photomultipliers at both sides, so that each detector produced two measurements. SCI_{F1} was vertically oriented and gave *up* and *down* time signals, t_{up} and t_{down} . SCI_{F2} and SCI_{F4} were oriented horizontally, providing *left* and *right* signals, t_{left} and t_{right} . By combining this information, the following data were recorded:

$$T_{F1F2,DL} = t_{F1,down} - t_{F2,left} \quad (3.5)$$

$$T_{F1F2,UR} = t_{F1,up} - t_{F2,right} \quad (3.6)$$

$$T_{F2F4,LL} = t_{F2,left} - t_{F4,left} \quad (3.7)$$

$$T_{F2F4,RR} = t_{F2,right} - t_{F4,right} \quad (3.8)$$

We used three different energies of a ^{48}Ca primary beam to carry out the TOF_{F1F2} and TOF_{F2F4} calibrations, as we had done for the velocity correction of the MUSICs, which was explained in Section 3.1. From the corresponding velocity values, we determined the times of flight and studied them as a function of the measured $T_{F1F2,DL}$, $T_{F1F2,UR}$, $T_{F2F4,LL}$ and $T_{F2F4,RR}$ signals, see Fig. 3.3. The final time-of-flight values were evaluated as the averages 3.9 and 3.10.

$$\text{TOF}_{F1F2} = \frac{\text{TOF}_{F1F2,DL} + \text{TOF}_{F1F2,UR}}{2} \quad (3.9)$$

$$\text{TOF}_{F2F4} = \frac{\text{TOF}_{F2F4,LL} + \text{TOF}_{F2F4,RR}}{2} \quad (3.10)$$

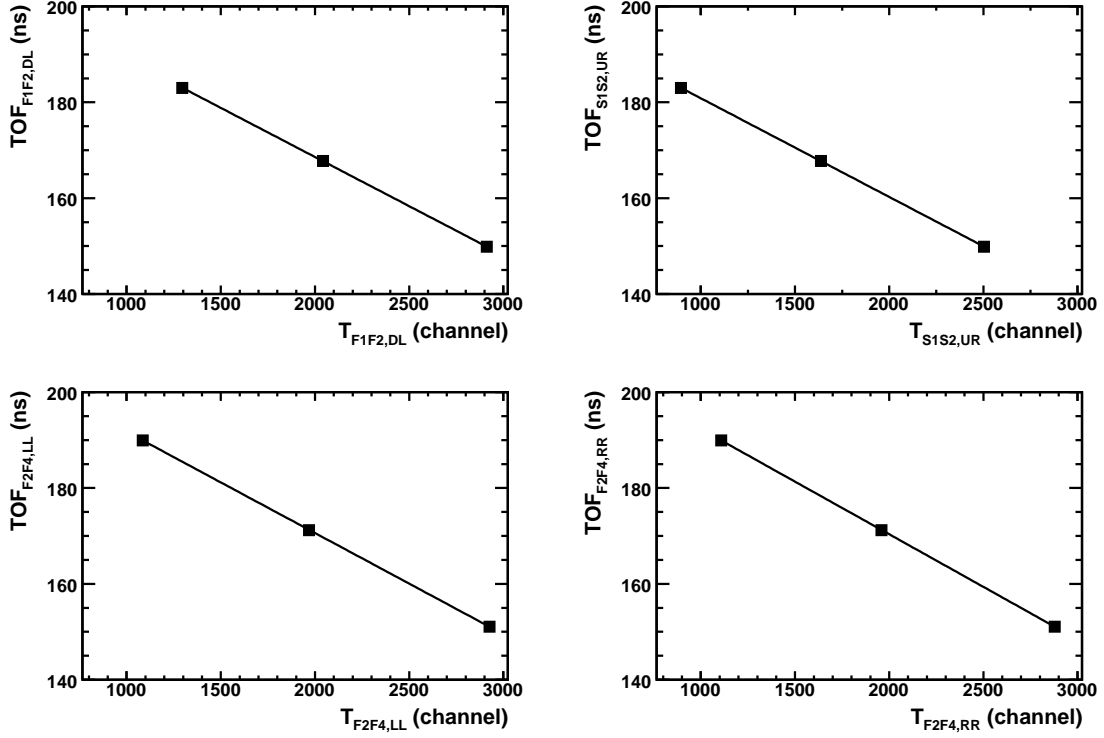


Figure 3.3: Calibrations of $\text{TOF}_{F_1F_2}$ and $\text{TOF}_{F_2F_4}$. Measurements were done for three energies of a ^{48}Ca primary beam, 350, 452 and 690 MeV/nucleon.

3.3 TPC calibration

In Chapter 2, we explained how the x and y coordinates are measured in a time-projection chamber. Here, we will describe the calibrations needed to transform the recorded signals into position data expressed in length units.

The TPCs used in this experiment had two delay lines, each one covering a pair of anodes, see Fig. 2.8 in Chapter 2. As a consequence, each detector produced eight different time signals:

- The anode drift times, related to the y coordinate, t_{a1} , t_{a2} , t_{a3} and t_{a4} .
- The times at the left and right ends of the two delay lines, related to the x coordinate, $t_{d1,left}$, $t_{d1,right}$, $t_{d2,left}$ and $t_{d2,right}$.

In Fig. 3.4, we show a schematic representation of the measured signals. It is important to clarify that $t_{d,left}$ and $t_{d,right}$ do not simply correspond to the time that the signal induced in the delay line needs to reach the left and right ends, but also include the anode drift time, t_a .

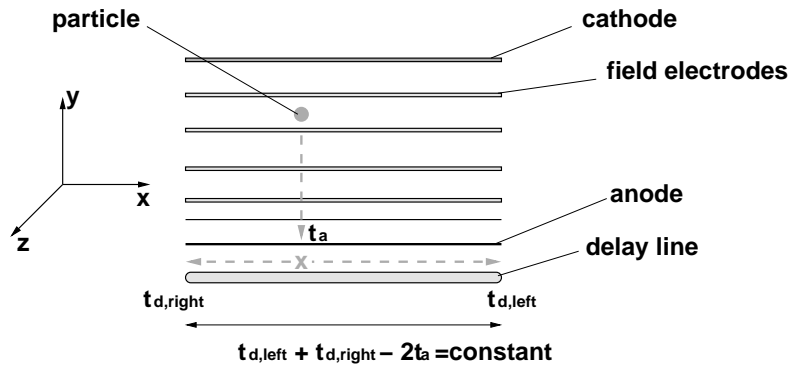


Figure 3.4: Schematic frontal view of a TPC. The anode drift time, t_a , provides a measurement of the y coordinate. The signal then spreads to both ends of the delay line and the x coordinate is determined from the difference $t_{d,left} - t_{d,right}$. The length of the delay line can be calculated as $t_{d,left} + t_{d,right} - 2t_a$.

Noise signals can easily be rejected by applying a simple filter based on the fact that the total length of the delay line is constant. This filter is usually known as *control-sum condition* and is expressed by Eq. 3.11, which must be verified by any correct TPC signal and is illustrated in Fig. 3.4.

$$t_{di,left} + t_{di,right} - 2t_{aj} = \text{constant} \quad (3.11)$$

The index j refers to any of the two anodes associated with the delay line i .

The different anodes, as well as the delay lines, were individually calibrated and, thus, a single TPC provided four and two measurements of the y and x coordinates, respectively. They were averaged to obtain the final position values.

We followed two different methods in the calibration of the TPCs:

- For TPC2, 3 and 4, we placed a metallic grid in front of the detector, associating the different holes in the x and y signals with the corresponding positions in the grid.
- For TPC1, 5 and 6, we used a mask of scintillators and looked for the coincidences between the TPC and the SCI signals. The peaks coming from them were identified with the position of each scintillator strip.

Both methods are represented in Fig. 3.5, which shows the linear correlation between the raw information in channels and the position in mm.

TPC alignment

After the position calibration, the measurements provided by the four TPCs placed at the intermediate focal plane, F2, were cross-checked by means of data recorded

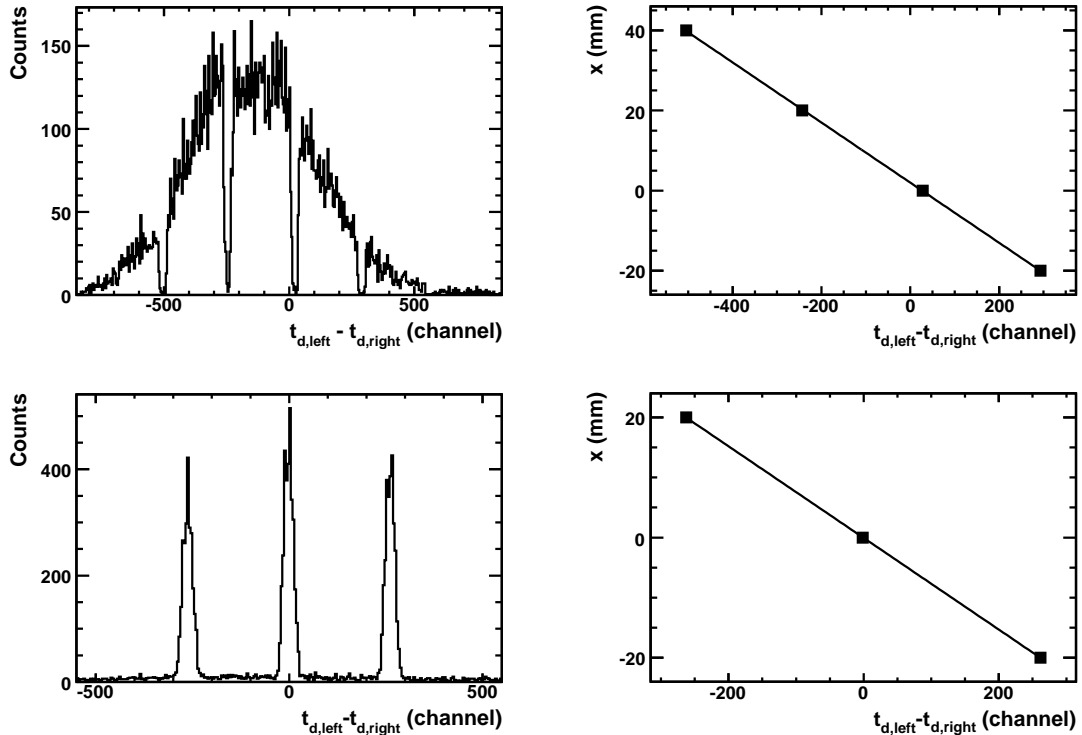


Figure 3.5: (Top) x calibration of a delay line using a metallic grid in front of the TPC. The plot on the left shows the holes in the TPC signals produced by the grid and the plot on the right shows the positions associated with each hole. (Bottom) x calibration of a delay line using a mask of scintillators. The plot on the left shows the coincidences between the TPC and the SCI signals. The plot on the right shows the positions associated with each coincidence.

without the knockout target in-between. In this way, we found a permanent incoherence that revealed a vertical and horizontal misalignment of the detectors that needed to be corrected.

The redundant information coming from the four TPCs showed that one of the detectors was displaced with respect to the others, see Fig. 3.6. The same effect was observed in both x and y directions, but the shifted detectors were different in each case. We defined the proper alignment using the three TPCs that had consistent measurements. Then, in order to correct the position data, we included additional offsets for the x and y coordinates, see Table 3.1.

TPC resolution

The calibration procedure was completed with the experimental evaluation of the TPC resolution in both the horizontal and the vertical directions. For that purpose,

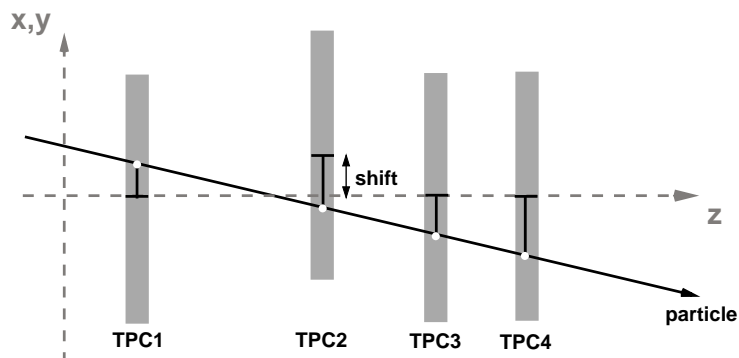


Figure 3.6: Example of the measurements performed with the TPCs at the intermediate focal plane, F2, when one of the detectors is shifted with respect to the others in either the horizontal or the vertical direction.

Detector	x offset (mm)	y offset (mm)
TPC1	0.04	-6.08
TPC2	-1.94	-0.10
TPC3	-0.17	0.21
TPC4	0.13	-0.11

Table 3.1: Correction of the TPC misalignment at F2, the x and y offsets were applied to the TPC measurements.

we used TPC1 and 2 to reconstruct the x position at the intermediate focal plane, $x_{F2,bt}$. Then, we repeated the procedure with TPC3 and 4 and obtained $x_{F2,at}$ ¹. The calculations are shown in Eqs. 3.12 and 3.13, where *dist* means *distance*.

$$x_{F2,bt} = x_{TPC2} + \left(\frac{x_{TPC2} - x_{TPC1}}{dist_{TPC2,TPC1}} \right) dist_{F2,TPC2} \quad (3.12)$$

$$x_{F2,at} = x_{TPC3} - \left(\frac{x_{TPC4} - x_{TPC3}}{dist_{TPC4,TPC3}} \right) dist_{TPC3,F2} \quad (3.13)$$

Afterwards, we subtracted the $x_{F2,bt}$ and $x_{F2,at}$ distributions and obtained a third distribution², $D_x = x_{F2,bt} - x_{F2,at}$, with a Gaussian profile and a width, σ_{D_x} , which satisfied Eq. 3.14.

$$\sigma_{D_x}^2 = \sigma_{x_{F2,bt}}^2 + \sigma_{x_{F2,at}}^2 \quad (3.14)$$

This expression was the starting point for obtaining the TPC resolution, σ_{TPC_x} . The terms $\sigma_{x_{F2,bt}}$ and $\sigma_{x_{F2,at}}$ followed Eqs. 3.15 and 3.16.

¹The labels *bt* and *at* mean *before the target* and *after the target*, respectively.

²This distribution was called D_x to refer to the *difference* between $x_{F2,bt}$ and $x_{F2,at}$.

Primary intensity (ions/spill)	FRS setting	Delay line 1 (%)	Delay line 2 (%)
$6 \cdot 10^9$	$^{24}\text{F} \rightarrow ^{23}\text{F}$	62	61
$7 \cdot 10^9$	$^{22}\text{N} \rightarrow ^{22}\text{N}$	38	26
$7 \cdot 10^9$	$^{25}\text{F} \rightarrow ^{24}\text{F}$	68	68
$7 \cdot 10^9$	$^{23}\text{O} \rightarrow ^{22}\text{O}$	38	33
$9 \cdot 10^9$	$^{20}\text{O} \rightarrow ^{19}\text{O}$	14	21
$1 \cdot 10^{10}$	$^{24}\text{O} \rightarrow ^{23}\text{O}$	25	28
$2 \cdot 10^{10}$	$^{22}\text{N} \rightarrow ^{21}\text{N}$	17	19

Table 3.2: Percentages of signals fulfilling the control-sum conditions for the delay lines of one of the TPCs placed at F2.

$$\sigma_{x_{F2,bt}}^2 = \sigma_{TPC_x}^2 + 2 \left(\frac{dist_{F2,TPC2}}{dist_{TPC2,TPC1}} \right)^2 \sigma_{TPC_x}^2 \quad (3.15)$$

$$\sigma_{x_{F2,at}}^2 = \sigma_{TPC_x}^2 + 2 \left(\frac{dist_{TPC3,F2}}{dist_{TPC4,TPC3}} \right)^2 \sigma_{TPC_x}^2 \quad (3.16)$$

Then, using these relations in Eq. 3.14 and working out σ_{TPC_x} , we arrived at:

$$\sigma_{TPC_x} = \sqrt{\frac{\sigma_{D_x}^2}{2 + 2 \left(\frac{dist_{F2,TPC2}}{dist_{TPC2,TPC1}} \right)^2 + 2 \left(\frac{dist_{TPC3,F2}}{dist_{TPC4,TPC3}} \right)^2}} \quad (3.17)$$

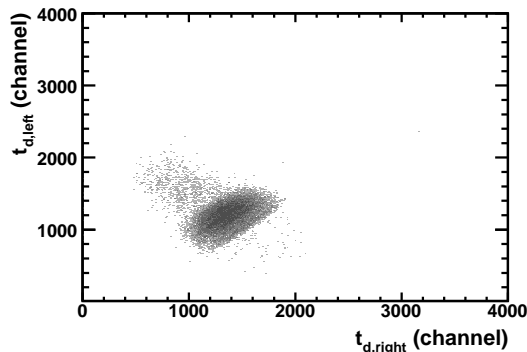
The width σ_{D_x} was measured without the knockout target for a ^{40}Ar primary beam centred through the Fragment Separator. We then calculated the denominator of this last formula, Eq. 3.17, and obtained $\sigma_{TPC_x} = 0.25$ mm.

The same methodology was applied for the vertical direction, resulting in $\sigma_{TPC_y} = 0.37$ mm.

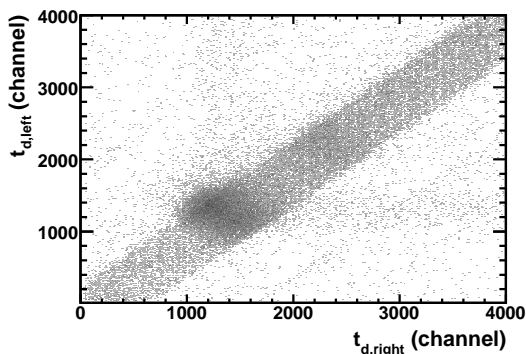
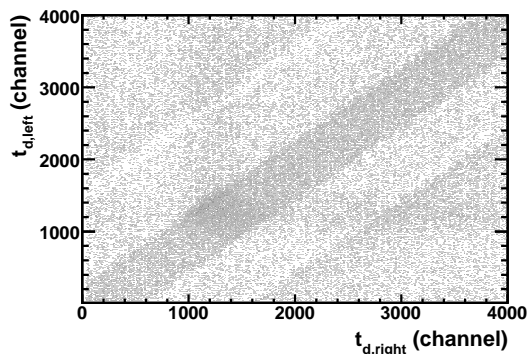
3.3.1 TPC efficiency at F2

The analysis of the experimental data revealed serious complications related to the TPCs at F2, which unfortunately were not detected during the beam time. This section is dedicated to explaining the difficulties we encountered and their consequences for the treatment of the data.

The first indication of a problem with the TPCs was observed after applying the control-sum filter to the production runs. The number of events verifying the control-sum conditions was significantly smaller than expected. Table 3.2 illustrates that this effect became more important for the most exotic runs, which are associ-



(a) Calibration run.

(b) Production run, $^{25}\text{F} \rightarrow ^{24}\text{F}$ setting.(c) Production run, $^{22}\text{N} \rightarrow ^{21}\text{N}$ setting.**Figure 3.7:** Relation between the left and right time signals registered by a TPC delay line.

ated with the highest intensities of the primary beam³.

In order to understand the causes of the reported failure, we analysed the relation between the right and left time signals in the delay lines. According to the control-sum condition, they should be linearly correlated, with an offset that depended on the drift time and with a negative slope. This is shown in Fig. 3.7. The plot labelled (a) corresponds to a calibration run where the TPCs worked correctly and serves as a reference for the expected behaviour. Labels (b) and (c) refer to production runs with different FRS settings. Both cases reveal many events where the right and left time signals were not properly correlated. They should not verify the control-sum condition and can be rejected on the basis of this filter. Those events that overcame the control-sum filter are displayed in Fig. 3.8, where the geometrical cuts indicate the region of the correct signals. However, we still observed some undesired events

³The FRS settings that appear in Table 3.2, labelled $^A\text{X} \rightarrow ^{A-1}\text{X}$, were characterised by different magnetic fields in the four FRS dipoles, which were adjusted to centre a certain projectile, ^AX , and a one-neutron knockout fragment, ^{A-1}X .

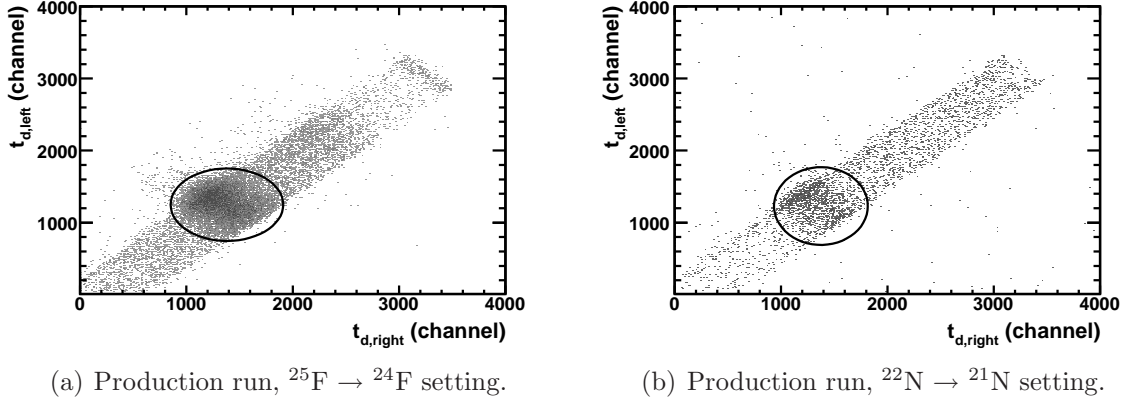


Figure 3.8: Relation between the left and right time signals registered by a TPC delay line after applying the control-sum condition.

Primary intensity (ions/spill)	FRS setting	Delay line 1 (%)	Delay line 2 (%)
$6 \cdot 10^9$	$^{24}\text{F} \rightarrow ^{23}\text{F}$	52	50
$7 \cdot 10^9$	$^{22}\text{N} \rightarrow ^{22}\text{N}$	29	21
$7 \cdot 10^9$	$^{25}\text{F} \rightarrow ^{24}\text{F}$	58	55
$7 \cdot 10^9$	$^{23}\text{O} \rightarrow ^{22}\text{O}$	30	28
$9 \cdot 10^9$	$^{20}\text{O} \rightarrow ^{19}\text{O}$	12	18
$1 \cdot 10^{10}$	$^{24}\text{O} \rightarrow ^{23}\text{O}$	15	14
$2 \cdot 10^{10}$	$^{22}\text{N} \rightarrow ^{21}\text{N}$	7	7

Table 3.3: Percentages of signals fulfilling the control-sum conditions and the geometrical cuts in the $t_{d,left}$ vs. $t_{d,right}$ spectra for one of the TPCs at F2.

that reflected drift-time values out of the expected range.

The low thresholds chosen for the TPCs at F2 during the production runs could explain the discussed complications: light background particles were able to create a *start* signal in the TPCs, but could not to produce a *stop* signal in the scintillator. The *stop* signal arrived from an uncorrelated heavier nucleus, explaining the large range observed in the drift-time values. To cross-check this hypothesis, we analysed the signal amplitudes in the TPC anodes. TPCs also work as an energy-loss detector and provide a rough measurement of the charge of the penetrating particle. We found a consistent accumulation of statistics in the low channels, associated with low-charge particles.

To get rid of these spurious events, we included additional filters in the analysis, related to the identification of the desired nuclei and to the selection of the appropriate data acquisition trigger. Once they were applied, together with the control-sum

Primary intensity (ions/spill)	FRS setting	TPC1 and 2 (%)	TPC3 and 4 (%)
$6 \cdot 10^9$	$^{24}\text{F} \rightarrow ^{23}\text{F}$	37	40
$7 \cdot 10^9$	$^{22}\text{N} \rightarrow ^{22}\text{N}$	14	10
$7 \cdot 10^9$	$^{25}\text{F} \rightarrow ^{24}\text{F}$	37	48
$7 \cdot 10^9$	$^{23}\text{O} \rightarrow ^{22}\text{O}$	10	10
$9 \cdot 10^9$	$^{20}\text{O} \rightarrow ^{19}\text{O}$	7	9
$1 \cdot 10^{10}$	$^{24}\text{O} \rightarrow ^{23}\text{O}$	1	7
$2 \cdot 10^{10}$	$^{22}\text{N} \rightarrow ^{21}\text{N}$	2	3

Table 3.4: The column *TPC1 and 2* shows the percentage of events where complete tracking of the projectiles was possible by means of TPC1 and 2, placed ahead of the knockout target. The column *TPC3 and 4* shows the percentage of events where it was possible to reconstruct the trajectories of the knockout fragments from the measurements of TPC3 and 4, placed behind the target.

conditions and the geometrical cuts in the $t_{d,left}$ vs. $t_{d,right}$ spectra, the selection of correct TPC events was improved.

The reduction of the TPC efficiency at F2 seriously damaged the experimental statistics. Table 3.3 summarises the number of signals verifying both the control-sum condition and the geometrical cut indicated in Fig. 3.8.

3.3.2 Tracking at F2

The determination of the physical observables in this experiment involved the reconstruction of the projectile and knockout-fragment trajectories at the F2 region. In order to identify the different nuclei and calculate the longitudinal momentum of the knockout fragments, it was necessary to know the exact x position of each nucleus at the intermediate focal plane; i.e., the reaction point. Moreover, tracking of the fragments after the reaction was crucial to performing the Doppler correction of the γ rays emitted in coincidence with the one-neutron knockout reaction.

In principle, the mentioned requirements could be fulfilled by the TPCs placed in front of and behind the knockout target, TPC1–4. This would facilitate complete tracking of both the projectiles and the fragments. However, as is summarised in Table 3.4, the complications with the detectors explained in Section 3.3.1 impeded such an analysis for a significant part of the data.

In order to reduce the consequences of the TPC failure on the experimental statistics, we developed an additional tracking procedure based on the FRS transfer matrices, see Appendix A. According to the transfer matrix between the in-

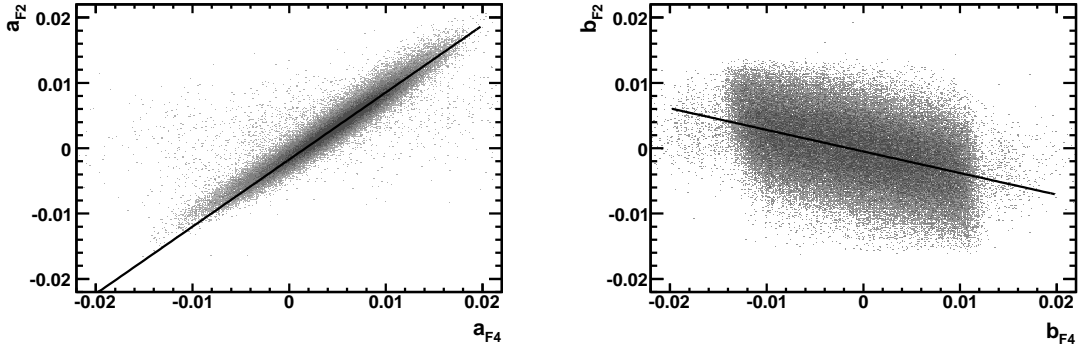


Figure 3.9: Dependence between the direction tangents at F2 and F4 in both horizontal and vertical directions, $a = \text{Tan}\theta_x$ and $b = \text{Tan}\theta_y$. The data were taken from calibration runs where the TPCs at F2 worked correctly.

intermediate and final focal planes, the direction tangents at F2, $a_{F2} = \text{Tan}\theta_{x_{F2}}$ and $b_{F2} = \text{Tan}\theta_{y_{F2}}$, were linearly correlated with the direction tangents at F4, $a_{F4} = \text{Tan}\theta_{x_{F4}}$ and $b_{F4} = \text{Tan}\theta_{y_{F4}}$. As is illustrated in Fig. 3.9, we used experimental data from the calibration runs to determine the parameters of these correlations, which are labelled C_{0-3} in Eqs. 3.18 and 3.19.

$$a_{F2} = C_0 a_{F4} + C_1 \quad (3.18)$$

$$b_{F2} = C_2 b_{F4} + C_3 \quad (3.19)$$

The evaluation of a_{F2} and b_{F2} from data recorded at F4 made it possible to reconstruct the trajectories of the knockout fragments from the position at either TPC3 or 4, without requiring a simultaneous good signal in both of them. Following this procedure, the observed statistics were increased by around 30 % and even more for settings with the highest intensities. However, this method could not be applied in the calculation of the one-neutron knockout cross-sections, which required detection of the fragment at the final focal plane. Thus, it could not be used to estimate the real number of projectiles impinging the target.

3.4 Dispersion measurements

Dispersion is a fundamental magnitude linked to the optical properties of the Fragment Separator. It determines the change in position induced by a difference in the fractional momentum deviation, defined by Eq. 3.20.

$$\delta_p = \frac{p - p_0}{p} \quad (3.20)$$

The variable p represents the momentum of the ion and p_0 , the momentum of the central trajectory.

Mathematically, the dispersion is usually expressed as follows:

$$D = (x|\delta) = \frac{\partial x}{\partial \delta_p} \quad (3.21)$$

In this experiment, the dispersion coefficients for the F0–F2 and F2–F4 stages of the Fragment Separator, named A and B respectively, were especially important for obtaining the longitudinal momentum of the knockout fragments. Although our selection of the FRS optics determined their nominal values, $D_A = -4.338$ cm/% and $D_B = 4.785$ cm/%, specific measurements were required for greater accuracy. For that purpose, we worked with a ^{40}Ar primary beam and scaled the magnetic fields in the dipoles, which changed the momentum of the central trajectory and, consequently, the δ_p value. The dispersion was evaluated by studying the changes induced in the x position of the beam.

As explained in Appendix A, the position at the focal plane F2 could be calculated as:

$$x_{F2} = (x|\delta)_A \delta_{F0} \quad (3.22)$$

where the coefficient $(x|\delta)_A$ represents the dispersion in the first stage of the spectrometer and δ_{F0} can be expressed as a function of the momentum of the central trajectory, p_A , and the momentum of the particle, p_{F0} .

$$\delta_{F0} = \frac{p_{F0} - p_A}{p_A} \quad (3.23)$$

Now, if we named as x_{F2} and x'_{F2} the positions measured for two different values of the fractional momentum deviation, δ_{F0} and δ'_{F0} , and we subtracted them in the light of Eq. 3.22, we would obtain:

$$x_{F2} - x'_{F2} = (x|\delta)_A (\delta_{F0} - \delta'_{F0}) \quad (3.24)$$

We developed the term $\delta_{F0} - \delta'_{F0}$, taking into account that only the momentum of the central trajectory changed.

$$\delta_{F0} - \delta'_{F0} = \frac{p_{F0} - p_A}{p_A} - \frac{p_{F0} - p'_A}{p'_A} = \frac{p_{F0}(p'_A - p_A)}{p'_A p_A} \quad (3.25)$$

Then, using this result in Eq. 3.24, we arrived at the following expression:

$$x_{F2} - x'_{F2} = (x|\delta)_A \frac{p_{F0}(p'_A - p_A)}{p'_A p_A} \quad (3.26)$$

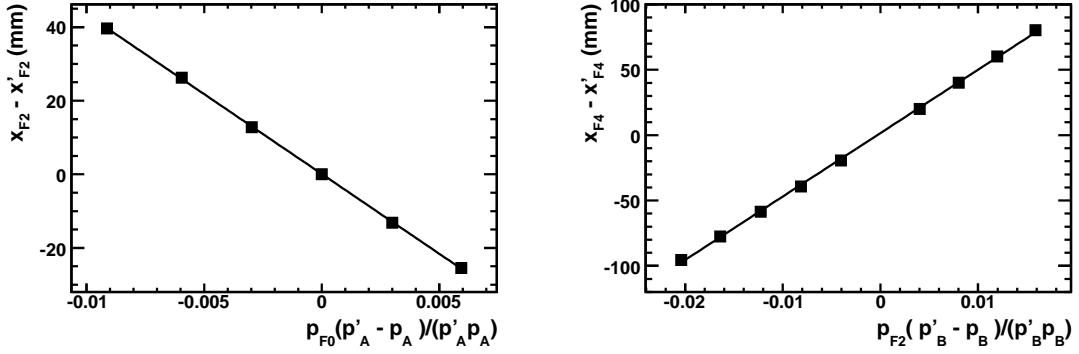


Figure 3.10: Determination of the dispersion coefficients from the experimental data. The slopes of the solid lines correspond to $D_A = (x|\delta)_A$ (right) and $D_B = (x|\delta)_B$ (left).

In Fig. 3.10, $x_{F2} - x'_{F2}$ is shown as a function of $\frac{p_{F0}(p'_A - p_A)}{p'_A p_A}$. The slope of the rising line was the dispersion between the focal planes F0 and F2 of the Fragment Separator, $D_A = (x|\delta)_A$.

Fig. 3.10 also illustrates the calculation of the dispersion coefficient in the second stage of the spectrometer, $D_B = (x|\delta)_B$. In this case, we followed a similar procedure, starting from the relation:

$$x_{F4} = (x|x)_B x_{F2} + (x|a)_B a_{F2} + (x|\delta)_B \delta_{F2} \quad (3.27)$$

which determines the position at F4, x_{F4} . This formula and the coefficients $(x|x)_B$ and $(x|a)_B$ are explained in Appendix A. The variable a_{F2} represents the x direction tangent at F2 and δ_{F2} could be written as follows:

$$\delta_{F2} = \frac{p_{F2} - p_B}{p_B} \quad (3.28)$$

where p_B and p_{F2} are the momenta of the central trajectory and of the particle in the second stage of the spectrometer.

The first two terms in the addition of Eq. 3.27 did not change during the measurements. Consequently, Eq. 3.29 was verified when working with two different values of the momentum of the central trajectory, p_B and p'_B . We then proceeded in analogy to the D_A calculation.

$$x_{F4} - x'_{F4} = (x|\delta)_B (\delta_{F2} - \delta'_{F2}) = (x|\delta)_B \frac{p_{F2}(p'_B - p_B)}{p'_B p_B} \quad (3.29)$$

Nevertheless, D_B needed to be evaluated at the exact location of the final focal plane. For that reason, we calculated its value at several z positions behind the spectrometer and used this data to build the line of Fig. 3.11, which allowed us to

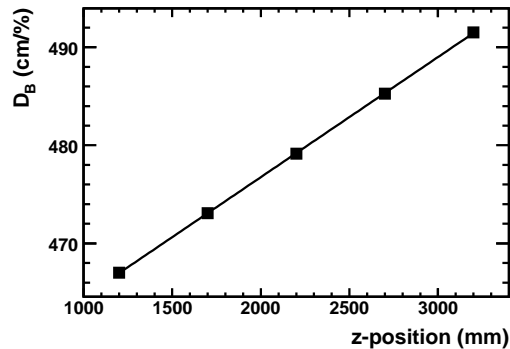


Figure 3.11: The squares represent the dispersion D_B obtained at different z positions behind the spectrometer. The dispersion line, which facilitated the determination of D_B at any z , is super-imposed.

obtain the dispersion at any z location.

3.5 Location of the final focal plane

The calculation of the longitudinal momentum of the knockout fragments was based on the transfer matrix between the intermediate and final focal planes of the FRS, F2 and F4. For this purpose, we made use of the equations described in Appendix A, where the momentum is given as a function of the positions x_{F2} and x_{F4} . The first was directly evaluated at the knockout target, but the exact z location of the final focal plane was experimentally determined for greater accuracy in obtaining x_{F4} .

In a system with point-to-point imaging, the matrix element $(x|a) = \frac{\partial x}{\partial a}$ has to be zero at the focal plane, which means that the horizontal position does not depend on the angle. The graphs of Fig. 3.12 show how the focal plane condition was verified for a certain z . However, these representations are merely qualitative and it is complicated to extract more precise information from them.

As an alternative, we looked for the z value with the narrowest x distribution, which is in fact a consequence of the $(x|a) = 0$ definition, see Fig. 3.13. Following this method, F4 was sighted at a z distance of 2700 ± 90 mm, measured from the exit of the magnetic system. This value is the average of the results obtained for different settings and the associated error corresponds to the standard deviation of the sample. It should be compared with the nominal location, $z = 2200$ mm.

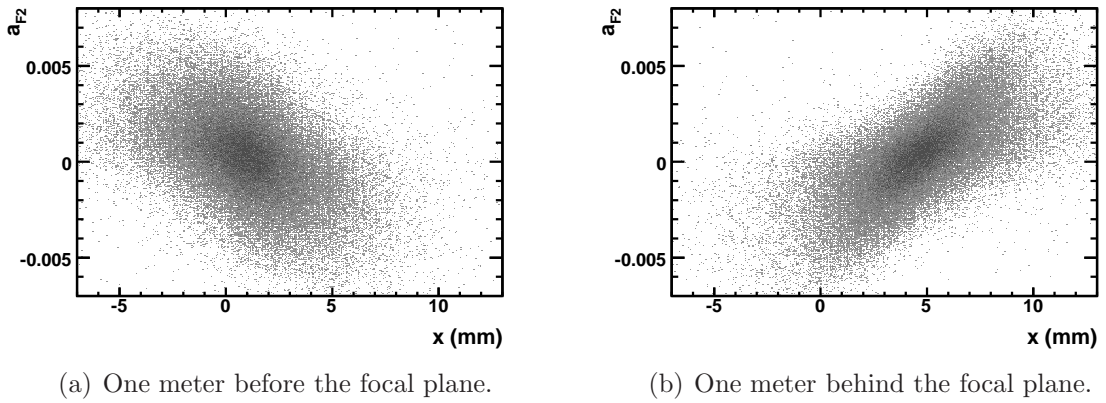


Figure 3.12: Correlation between the direction tangent a_{F2} and the x position at different z locations in the F4 region. The two quantities are independent at the focal plane.

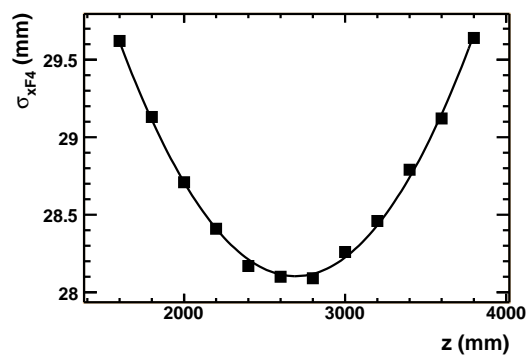


Figure 3.13: Width of the x distribution as a function of the z position in the F4 region. The minimum indicates the exact location of the focal plane.

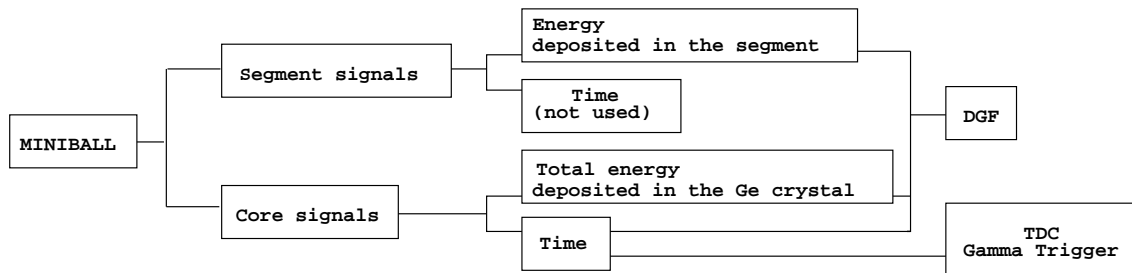


Figure 3.14: Diagram of the different MINIBALL signals. The core times were used to avoid background events and select those γ rays emitted in coincidence with the knockout reaction. The full energy of the detected γ rays was obtained in the reference frame of the laboratory from the core energies after an appropriate add-back procedure. The segment energies determined the first interaction point in the cluster and were used to perform the Doppler correction and transform the measured γ energy into the frame of the emitting fragment. The signals were processed by means of DGF and TDC modules, the last of which was also responsible for the γ trigger.

3.6 MINIBALL calibration

As was explained in Section 2.2.4, MINIBALL can be understood as an array of segmented Ge detectors organised in several clusters. Specifically, it is composed of eight clusters of three Ge crystals each, which are further divided into six segments. Fig. 3.14 summarises the signals provided by this complex structure. Every segment and core produced time and energy signals, see Fig. 2.10, which were later processed by DGF⁴ and TDC⁵ modules, the latter of which was responsible for the γ trigger.

We will describe in greater detail the different types of data coming from MINIBALL:

- The core time signals indicate the precise instant of γ detection. With this information, we could easily select the coincidences with knockout events by applying a convenient time window.
- The core energy signals were used to reconstruct the full energy of the detected γ rays. For that purpose, the add-back procedure of Eq. 3.30 was applied, adding up the energies deposited in the three Ge crystals that compose each cluster.

⁴DGF is the acronym of Digital Gamma Finder. A DGF is a pulse processor capable of measuring both the amplitude and the shape of pulses in nuclear spectroscopy applications.

⁵TDC is the acronym of Time to Digital Converter. In electronic instrumentation and signal processing, a TDC is a device for converting sporadic pulse signals into a digital representation of their time indices. In other words, it outputs the time of arrival for each incoming pulse. Because the magnitudes of the pulses are not usually measured, a TDC is used when the important information is found in the timing of events.

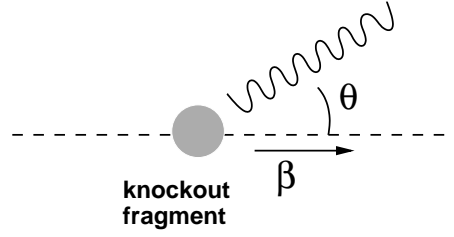


Figure 3.15: In order to perform the Doppler correction, the velocity of the knockout fragment, β , and the angle with respect to the trajectory of the emitted γ ray, θ , were needed. The velocity was obtained from TOF measurements. The angle θ was determined from the first γ interaction point in MINIBALL and from the emission point at the knockout target.

$$E_{lab,k} = \sum_{j=1}^3 E_{core,j,k} \quad (3.30)$$

Here, $E_{core,j,k}$ represents the energy signal coming from the core j of the cluster k , with $j = 1-3$ and $k = 1-8$. $E_{lab,k}$ is the total energy deposited in the cluster k , measured in the reference frame of the laboratory.

- The segment time signals were not used in the analysis.
- The segment energy signals indicated the first γ interaction point in the detector, which was calculated as the centre of mass of the segment with the maximum energy deposited. Then, using the emission point at the target⁶, we could reconstruct the γ trajectory and its emission angle with respect to the direction of the knockout fragment, θ , as represented in Fig. 3.15. This angle was needed to transform the γ energy of Eq. 3.30 into the reference frame of the fragment using the Doppler correction formulated in Eq. 3.31,

$$E_{source,k} = \gamma E_{lab,k} (1 + \beta \cos \theta) \quad (3.31)$$

where $\gamma = \frac{1}{\sqrt{1-\beta^2}}$ and β refers to the velocity of the fragment, previously determined from TOF measurements.

A complete calibration was not needed for the core time signals. They were simply shifted to place the knockout time windows within a convenient range of channels.

The segment and core energy signals were calibrated by means of ^{60}Co and ^{152}Eu sources. As illustrated in Fig. 3.16, the raw signals, e , were identified with the γ

⁶It corresponds to the reaction point and was determined from the tracking at the F2 region by means of the TPC position measurements.

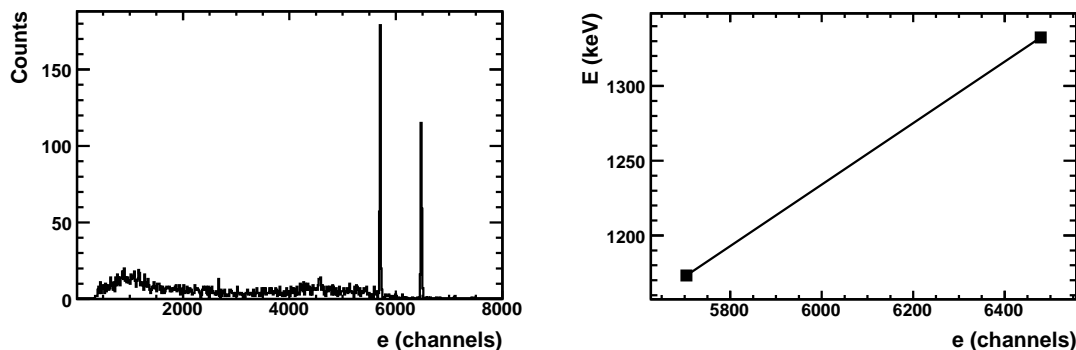


Figure 3.16: (Left) Raw core energy signals measured with a ^{60}Co source. The two γ rays emitted in the β decay of ^{60}Co , with energies of 1173 and 1333 keV, can be clearly distinguished. (Right) Calibration plot: the γ energy is represented in keV as a function of the raw signals. More points were obtained from measurements with ^{152}Eu , improving the accuracy of the calibration.

energies emitted, E , expressed in keV. The coefficients of Eqs. 3.32 and 3.33 could then be determined.

$$E_{segment,i,j,k} = a_{i,j,k} + b_{i,j,k} \cdot e_{segment,i,j,k} \quad (3.32)$$

$$E_{core,j,k} = c_{j,k} + d_{j,k} \cdot e_{core,j,k} \quad (3.33)$$

The sub-indexes $i = 1-6$, $j = 1-3$ and $k = 1-8$ denote the segment, the core and the cluster, respectively.

3.6.1 MINIBALL efficiency

The γ measurements were used to obtain the probabilities of populating different fragment states in the one-neutron knockout reaction. These calculations required accurate knowledge of the MINIBALL efficiency, which was experimentally determined by means of ^{152}Eu , ^{56}Co and ^{60}Co sources located at the target position. The results are compiled in Table 3.5.

However, the efficiency measurements were performed with static calibration sources and could not be directly applied to the knockout analysis, where we faced γ rays emitted by relativistic nuclei. In order to obtain an appropriate estimation of the MINIBALL efficiency, we used a detailed Geant 4 simulation of the detector [Boi02, Gea] in which the velocity of the emitting nuclei and the distribution of the emission point at the target were considered. An additional ROOT macro [ROO] also allowed us to reproduce the add-back procedure and the Doppler correction in a manner similar to how they were applied to the real knockout data.

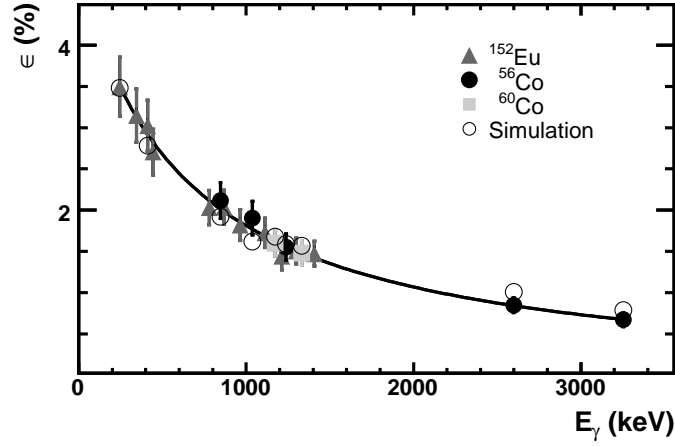


Figure 3.17: MINIBALL efficiency. The experimental data obtained with ^{152}Eu , ^{56}Co and ^{60}Co calibration sources are shown together with the results of the Geant 4 simulation.

E_γ (keV)	ϵ (%)	E_γ (keV)	ϵ (%)
245	3.49 ± 0.36^a	1112	1.73 ± 0.18^a
344	3.15 ± 0.32^a	1173	1.60 ± 0.16^c
411	3.02 ± 0.31^a	1213	1.44 ± 0.16^a
444	2.70 ± 0.28^a	1238	1.55 ± 0.16^b
779	2.03 ± 0.21^a	1299	1.50 ± 0.16^a
847	2.11 ± 0.22^b	1333	1.48 ± 0.15^c
867	2.03 ± 0.21^a	1408	1.47 ± 0.15^a
964	1.82 ± 0.19^a	2598	0.85 ± 0.09^b
1038	1.90 ± 0.20^b	3253	0.67 ± 0.09^b

Table 3.5: Experimental values of the MINIBALL efficiency for different γ energies. The measurements were performed with $^a) ^{152}\text{Eu}$, $^b) ^{56}\text{Co}$ and $^c) ^{60}\text{Co}$ calibration sources located at the target position.

The MINIBALL simulation was tested with simple static cases, covering the energy range found in Table 3.5. The good agreement with the efficiency measurements carried out can be observed in Fig. 3.17. On this basis, the simulation was applied to relativistic events and, as will be shown in Section 4.4, was used to reconstruct the γ spectra measured in this experiment.

Although the simulation accounted for the relativistic γ emitters and successfully described the intrinsic and geometrical detection efficiencies, two additional corrections were still required:

- The MINIBALL dead time, $\epsilon_{dead\ time}$, was calculated as the ratio between

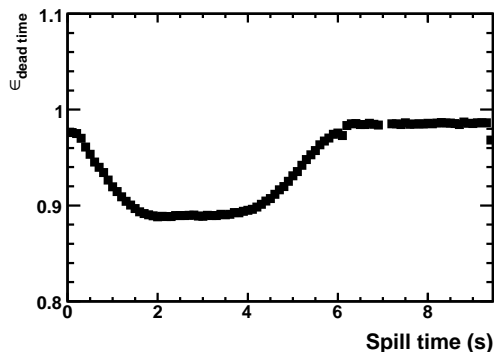


Figure 3.18: MINIBALL dead time as a function of the spill time. $\epsilon_{dead\ time}$ corresponds to the ratio between the accepted and the total number of γ triggers.

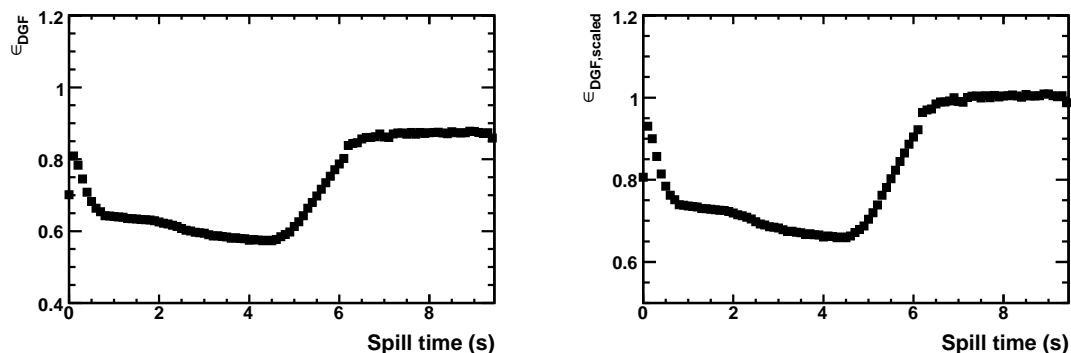


Figure 3.19: Correction factor which accounted for the accepted γ triggers with null DGF signals. (Left) The DGF threshold, which excluded low-energy γ rays, explains the values $\epsilon_{DGF} < 1$ observed outside the spill. (Right) ϵ_{DGF} was scaled up to unity outside the spill because the DGF thresholds did not affect the high-energy γ rays emitted by the one-neutron knockout fragments.

the accepted and the total number of γ triggers. In Fig. 3.18, $\epsilon_{dead\ time}$ is represented as a function of the spill time for a given set of measurements. We can see how it dropped to 0.9 during the spill and later reached a value close to unity.

- The second correction, ϵ_{DGF} , was related to the fact that some γ triggers provided by the TDC module corresponded to null DGF signals and was calculated as the percentage of accepted γ triggers with a valid DGF signal. In order to understand this effect, two different contributions must be considered:
 - (i) First of all, we worked with a DGF threshold that excluded low-energy γ rays. This is why, in Fig. 3.19 (left), we observe $\epsilon_{DGF} < 1$ outside the spill. However, the DGF threshold did not affect the high-energy γ rays we were interested in and ϵ_{DGF} was therefore scaled up to unity, as seen

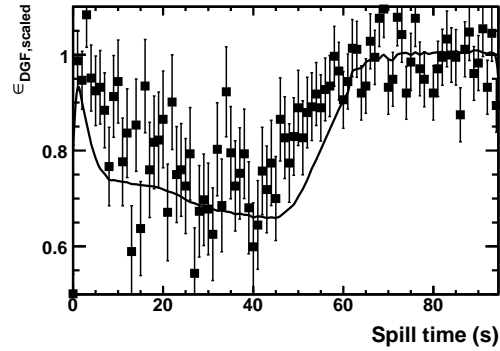


Figure 3.20: Squares represent the experimental 1460 keV counting rate. The solid line corresponds to the calculated factor $\epsilon_{DGF,scaled}$.

in Fig. 3.19 (right).

- (ii) The effect that remained during the spill was interpreted as a drop in the core baseline due to the average signal load and was accounted for by means of what is called $\epsilon_{DGF,scaled}$. In order to verify this correction factor, the 1460 keV background line produced in the β decay of ^{40}K is studied. ^{40}K is present in the concrete that surrounds the experimental setup and, after a dead time correction, the 1460 keV γ rays should be always detected with the same counting rate, independently of the spill time. Fig. 3.20 was created with experimental data and shows that, far from being constant, the 1460 keV counting rate behaved analogously to $\epsilon_{DGF,scaled}$, thus probing the validity of our calculations.

$$\epsilon_{total} = \epsilon_{dead\ time} \cdot \epsilon_{DGF,scaled} \quad (3.34)$$

Chapter 4

The physical observables

We will begin this chapter by describing the determination of the one-neutron knockout channel, based on the unambiguous identification of both the projectile and the fragment produced in the reaction.

Then, we will focus on the calculation of two physical observables that were sensitive to the nuclear structure of our exotic projectiles, namely, the inclusive longitudinal-momentum distribution of the fragments and the inclusive cross-section of the one-neutron knockout process.

The last section will be dedicated to the evaluation of the exclusive cross-sections for those cases where, with the help of MINIBALL, it was possible to disentangle the contributions from the different states of the fragment populated in the reaction. Due to insufficient statistics and the complexity of the measured γ spectra, this analysis could only be performed for a reduced number of projectiles.

As in Chapter 3, we will rely on several concepts and equations related to the optics of charged particles. A detailed explanation can be found in Appendix A.

4.1 Identification

The one-neutron knockout channel was selected by identifying the nuclei before and after the reaction target. For that purpose, the charge of the nuclei was measured with the MUSICs placed at F2 and F4, as was described in Chapter 3; the exact locations of the MUSICs are shown in Figs. 2.5 and 2.6. Since we worked with fully stripped nuclei, the obtained charge was equal to the atomic number, Z . However, additional information was required to distinguish between the different isotopes. The mass-to-charge ratio was also determined in order to complete the identification.

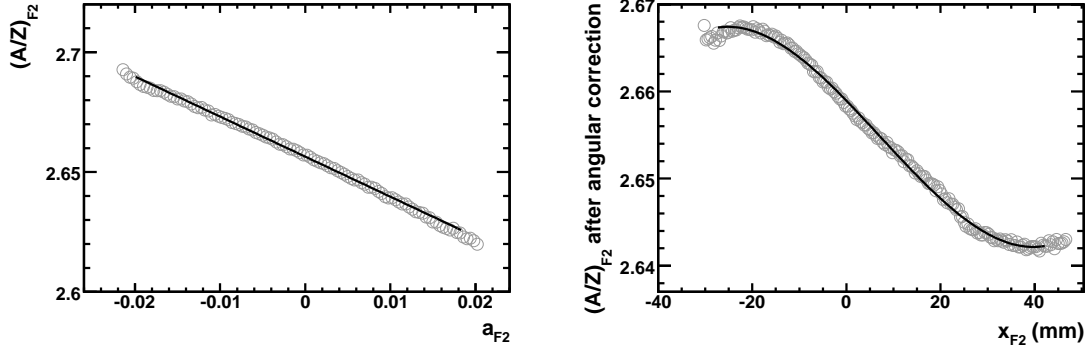


Figure 4.1: Correction of the mass-to-charge ratio dependences in the first stage of the FRS. The solid lines in both graphs represent fits to the experimental data that were used to determine the correction functions. (Left) The ratio $(A/Z)_{F2}$ depends linearly on the direction tangent $a_{F2} = \text{Tan}\theta_{x_{F2}}$. (Right) The graph was created after correcting the angular dependence and shows a correlation with the x_{F2} position. The data were fitted to a third-order polynomial. In the second stage of the spectrometer, the ratio $(A/Z)_{F4}$ only showed a linear dependence on the variable $a_{F4} = \text{Tan}\theta_{x_{F4}}$.

4.1.1 Measuring the mass-to-charge ratio

In general, the mass-to-charge ratio can be easily related to the motion of the ion in the magnetic dipole fields of the Fragment Separator. Such a relation is expressed below by the Lorentz equation,

$$F = qvB = \frac{mv^2}{\rho} = \frac{\gamma m_0 v^2}{\rho} \quad (4.1)$$

where B is the magnetic field perpendicular to the direction of motion and ρ is the radius of the circular path of the ion under the effect of B . The parameter m_0 represents the rest mass of the ion and v , its velocity. Finally, $\gamma = \frac{1}{\sqrt{1-\beta^2}} = \frac{1}{\sqrt{1-(\frac{v}{c})^2}}$.

Eq. 4.1 can lead us directly to:

$$\frac{m_0}{q} = \frac{B\rho}{\gamma\beta c} \quad (4.2)$$

and then to:

$$\frac{A}{Z} = \frac{e}{u} \cdot \frac{B\rho}{\gamma\beta c} \quad (4.3)$$

where e is the charge of the electron and u , the atomic mass unit.

According to this expression, the calculation of the mass-to-charge ratio, A/Z , would involve the measurement of the ion velocity and the product $B\rho$. The velocity was obtained from the time of flight between the scintillators, TOF_{F1F2} and

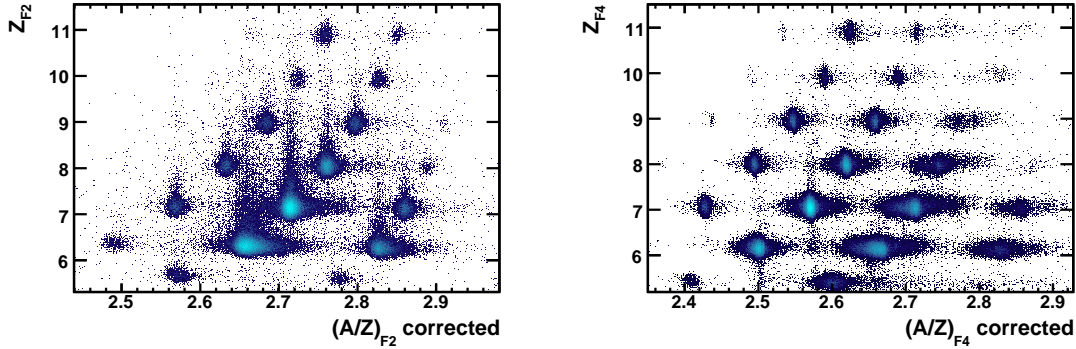


Figure 4.2: Identification plots with the corrected A/Z ratios. The graph on the left side corresponds to the identification carried out before the reaction target at F2. The graph on the right shows the identification of fragments coming out from the target and reaching the final focal plane of the FRS.

TOF_{F2F4}. The quantity $\chi = B\rho$ is usually known as magnetic rigidity and its value should be determined in the two stages of the FRS in order to identify the nuclei before and after the knockout target.

The magnetic rigidities associated with the trajectories of the nuclei through the two stages of the FRS, χ_{F0} and χ_{F2} , verified the following equations:

$$\chi_{F0} = \chi_A \left(1 + \frac{x_{F2}}{D_A} \right) \quad (4.4)$$

$$\chi_{F2} = \chi_B \left(1 - \frac{M_B x_{F2} - x_{F4}}{D_B} \right) \quad (4.5)$$

Here, the sub-indexes A and B refer to the first and second stages of the FRS, respectively. χ_A and χ_B are the magnetic rigidities of the central trajectories. The parameters M and D represent the magnification and the dispersion, elements of the transfer matrices that are explained in Appendix A. The variables x_{F2} and x_{F4} were determined from the TPC measurements and correspond to the x positions at the intermediate and final focal planes.

At this stage of the analysis, neither the dispersion nor the location of the final focal plane had been calculated from the experimental data, but the nominal values were sufficient for our identification purposes. We also used the nominal value of the magnification.

In order to determine the reference magnetic rigidities, χ_A and χ_B , the magnetic fields in the dipoles were measured by means of Hall probes during the experiment and the effective radii of the central trajectory were calculated from a centered pri-

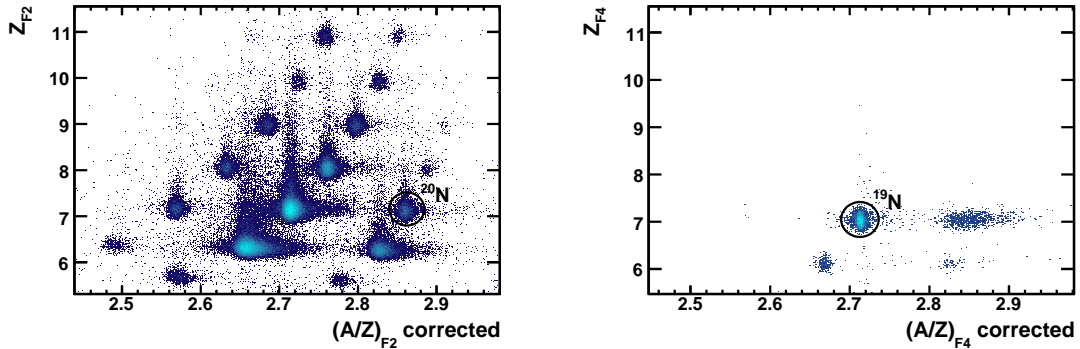


Figure 4.3: Determination of the reaction channel, in this case, ^{20}N one-neutron knockout. The projectile was first selected by making a geometrical cut in the F2 identification plot. Then, the one-neutron knockout fragment was selected from among the different nuclei reaching the final focal plane of the FRS.

mary beam with a well-known energy.

The identification of the nuclei was then achieved from the determination of the atomic number, Z , and the mass-to-charge ratio, A/Z . However, the calculated A/Z showed clear dependences on the horizontal angle and position, reflecting some imprecision that needed correcting in the calculations. In order to improve the quality of the identification, we studied the reported dependences in Fig. 4.1 and introduced the appropriate correction functions, based on polynomial fits to the experimental data.

An example of the final identification plots is given in Fig. 4.2. There, the different nuclei appear clearly and separate from each other. Fig. 4.3 illustrates the selection of a certain $^A X$ projectile at F2, that automatically cleaned the identification plot at F4, highlighting the associated $^{A-1} X$ fragment. A double condition like the one displayed in the figure defined the reaction channel without any ambiguity.

4.2 Inclusive longitudinal-momentum distributions

One of the physical observables determined in this experiment was the longitudinal momentum of the fragments resulting from the one-neutron knockout of exotic neutron-rich projectiles. In the high-energy regime, the shape and width of these distributions can be used to identify the orbital angular momentum of the neutron removed in the reaction.

4.2.1 Calculation of the longitudinal momentum

The longitudinal momentum of the one-neutron knockout fragments was determined in the reference frame of the laboratory using Eq. 4.6, which is carefully explained in Appendix A and depends on the positions at the intermediate and final focal planes, x_{F2} and x_{F4} .

$$p_{F2} = q_B \chi_B \left(1 + \frac{x_{F2}}{(x|\delta)_A} + \frac{x_{F4}}{(x|\delta)_B} \right) \quad (4.6)$$

The positions x_{F2} and x_{F4} were calculated from the TPC measurements. The magnitudes $(x|\delta)_A$ and $(x|\delta)_B$ correspond to the experimental values of the dispersion in the first and second stages of the Fragment Separator. χ_B is the reference magnetic rigidity in the second half of the FRS and q_B is the charge of the knockout fragment.

Afterwards, it was necessary to convert the momentum p_{F2} into the projectile comoving frame. For that purpose, we applied the following Lorentz transformation,

$$p_{||} = \gamma_{F0} \left(p_{F2} - \beta_{F0} \frac{E_{F2}}{c} \right) \quad (4.7)$$

where β_{F0} represents the velocity of the projectile and E_{F2} , the total energy of the fragment in the laboratory, verifying $E_{F2} = \sqrt{p_{F2}^2 c^2 + m_B^2 c^4}$. m_B is the rest mass of the one-neutron knockout fragment.

The Lorentz transformation needed to be carried out for each particle using its velocity, β_{F0} , which was calculated from the momentum of the projectile, p_{F0} , according to Eq. 4.8:

$$\beta_{F0} = \sqrt{1 - \frac{m_A^2 c^4}{p_{F0}^2 c^2 + m_A^2 c^4}} \quad (4.8)$$

The momentum p_{F0} was determined with high accuracy from the position x_{F2} using the formula below,

$$p_{F0} = q_A \chi_A \left(1 + \frac{x_{F2}}{(x|\delta)_A} \right) \quad (4.9)$$

where χ_A represents the reference magnetic rigidity in the first half of the FRS and q_A , the charge of the projectile.

The momentum distributions obtained with this procedure were centred at negative values around a few hundred of MeV/c due to the fact that our calculations did not account for the slowing down of the nuclei in the several layers of matter present at the F2 region. This effect can be corrected by reducing the β_{F0} value:

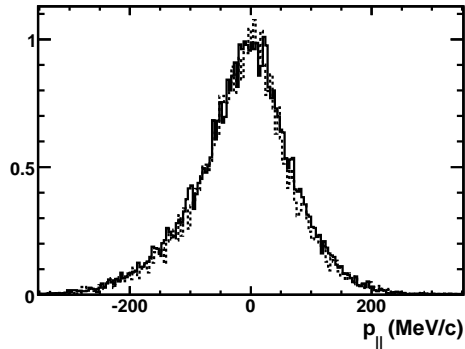


Figure 4.4: Normalised longitudinal-momentum distribution of ^{23}F after one-neutron knockout of ^{24}F . The solid and dashed lines correspond to different sets of measurements, revealing a perfect agreement between them.

$$\beta_{F0,corrected} = \beta_{F0} - \Delta\beta_{F0} \quad (4.10)$$

The quantity $\Delta\beta_{F0}$ could be evaluated from specific measurements where the second stage of the FRS was configured for transmitting projectiles that did not react in the target, by simply comparing the projectile velocities in the second stage with the previous β_{F0} values. MOCADI simulations [Iwa97] could also be performed for those cases where experimental evaluation was not possible. These corrections produced a mean value closer to zero for the momentum distributions. However, they did not lead to any significant difference in shape or width, which were the important observables for our studies.

The results that will be presented and discussed in this work were obtained according to Eqs. 4.6–4.9, without any additional correction. Later on, the momentum distributions were manually shifted to zero, since we were not interested in the central values.

In order to cross-check the validity of our calculations, we applied the procedure explained in the previous paragraph to several sets of measurements where the same nucleus was transmitted through the FRS. The comparison of the results is illustrated in Fig. 4.4 and shows a perfect agreement between them.

4.2.2 Momentum resolution

The final momentum resolution that could be achieved was defined by several factors such as the resolution of the spectrometer, the optical quality of the primary beam, the amount of matter at the mid-plane and the resolution of the detectors. They

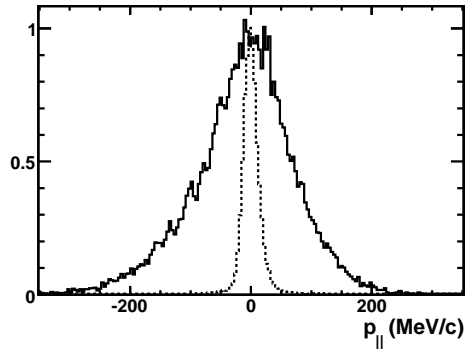


Figure 4.5: Normalised longitudinal-momentum distributions: (Solid line) ^{23}F after one-neutron knockout of ^{24}F . (Dashed line) ^{24}F not reacting with the target and reaching the final focal plane. The width of this distribution was used as an estimation of the momentum resolution. The remarkable difference between both distributions confirmed the sensitivity of our measurements to nuclear-structure effects.

produced an extra broadening in the momentum distributions that is not related to the one-neutron knockout reaction.

In order to quantify the momentum resolution, we made use of projectiles that did not react in the target and did reach the final focal plane, see Fig. 4.5. The FWHM values of the longitudinal-momentum distributions measured for the one-neutron knockout fragments were then corrected as follows:

$$FWHM_{-n}^{corrected} = \sqrt{(FWHM_{-n}^g)^2 - (FWHM_{proj}^g)^2} \quad (4.11)$$

In the equation above, $FWHM_{-n}^g$ and $FWHM_{proj}^g$ are the result of Gaussian fits to the experimental distributions that correspond to the knockout fragment and the non-reacting projectile. This correction reduced the measured widths by 1–5 %, see Table 4.1.

4.2.3 Acceptance cuts

The optics used in this experiment allowed the transmission of several nuclei through the Fragment Separator during a single set of measurements. However, before extracting information from the observed momentum distributions, it was absolutely necessary to check whether artificial cuts appeared for those cases close to the acceptance limits of the spectrometer.

We carried out a systematic study for all the nuclei by means of two-dimensional graphs, as in the examples shown in Fig. 4.6, which pertain to the one-neutron knockout of ^{17}N and ^{20}O . The representation of the longitudinal momentum as a

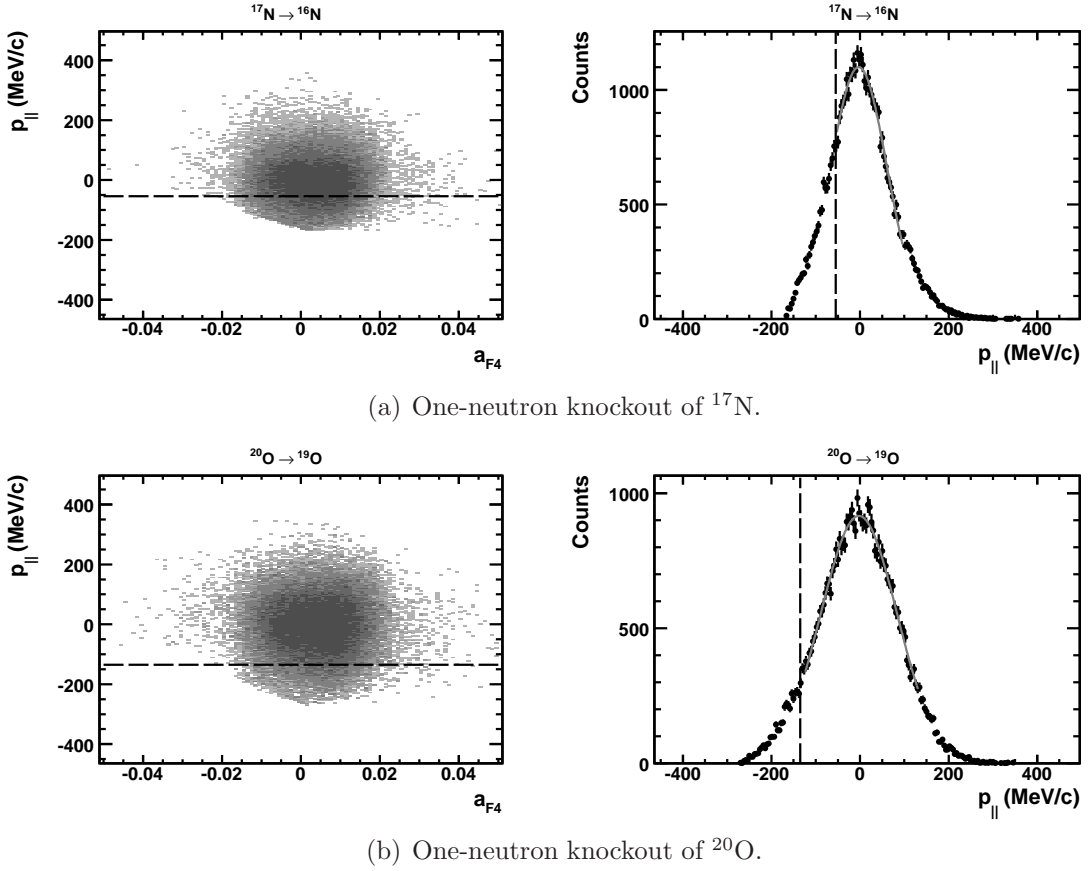


Figure 4.6: On the left side: the longitudinal momentum, $p_{||}$, as a function of the x direction tangent at the final focal plane, a_{F4} . On the right side: the projection on the momentum axis. The dashed lines mark the acceptance cuts.

function of the x angle at the final focal plane makes the acceptance cuts clearly visible.

In order to study a certain nucleus, we selected complete momentum distributions when they were available and, for the few cases where that was not possible, we carefully determined the affected region and excluded it from the analysis. However, in the one-neutron knockout of ^{14}C and ^{16}N , the poor transmission could only lead to biased results and it was not possible to extract the momentum widths. The distribution corresponding to ^{15}C projectiles was also noticeably cut and a graphical evaluation of the FWHM was applied.

4.2.4 FWHM of the longitudinal-momentum distributions

In the previous sections, we explained the calculation of the longitudinal-momentum distributions for the one-neutron knockout fragments. The goal was to analyse their

shapes and widths in order to extract information about the nuclear structure of the original neutron-rich projectiles.

Appendix B contains a compilation of the measured momentum distributions, along with the acceptance studies carried out and the Gaussian fits used to determine the FWHM values. The results were then corrected for the experimental resolution according to Eq. 4.11. They are summarised in Table 4.1, which also displays the data available from other works.

In this experiment, statistics was the main source of error. It determined the bin size of the momentum histograms and, thus, the precision of the calculated widths. The errors associated with the FWHM values reflect the bin size chosen for each case.

Projectile	N	FWHM _{-n} ^g (MeV/c)	FWHM _{-n} ^{corrected} (MeV/c)
¹⁵ C	9	58 ± 12	57 ± 12 ⁽ⁱ⁾ 63.5 ± 0.7 ^(iv) 67 ± 4 ^(v)
¹⁶ C	10	118 ± 8	117 ± 8 ⁽ⁱ⁾ 108 ± 2 ^(iv)
¹⁷ C	11	151 ± 16	150 ± 16 ⁽ⁱ⁾ 111 ± 3 ^(iv) 145 ± 5 ^(v) 141 ± 6 ^(vi) 100 ± 10 ^(vii)
¹⁸ C	12	155 ± 8	154 ± 8 ⁽ⁱ⁾ 126 ± 5 ^(iv) 98 ± 13 ^(vii)
¹⁹ C	13	62 ± 16	59 ± 16 ⁽ⁱ⁾ 42 ± 4 ^(v) 69 ± 3 ^(vi)
¹⁷ N	10	150 ± 4	148 ± 4 ⁽ⁱ⁾ 169 ± 10 ⁽ⁱⁱⁱ⁾ 141 ± 4 ^(iv)
¹⁸ N	11	165 ± 8	164 ± 8 ⁽ⁱ⁾ 154 ± 10 ⁽ⁱⁱⁱ⁾ 168 ± 3 ^(iv)
¹⁹ N	12	186 ± 4	184 ± 4 ⁽ⁱ⁾ 192 ± 10 ⁽ⁱⁱⁱ⁾ 177 ± 3 ^(iv)
²⁰ N	13	182 ± 16	180 ± 16 ⁽ⁱ⁾ 173 ± 10 ⁽ⁱⁱⁱ⁾

Table 4.1 Continued on next page.

Projectile	N	FWHM _{-n} ^g (MeV/c)	FWHM _{-n} ^{corrected} (MeV/c)
			162 ± 4 ^(iv)
²¹ N	14	181 ± 32	180 ± 32 ⁽ⁱ⁾ 149 ± 7 ^(iv)
²² N	15	104 ± 32	102 ± 32 ⁽ⁱ⁾
¹⁹ O	11	186 ± 8	184 ± 8 ⁽ⁱ⁾ 183 ± 10 ⁽ⁱⁱ⁾ 190 ± 8 ^(iv)
²⁰ O	12	202 ± 4	201 ± 4 ⁽ⁱ⁾ 199 ± 10 ⁽ⁱⁱ⁾ 219 ± 5 ^(iv)
²¹ O	13	209 ± 4	207 ± 4 ⁽ⁱ⁾ 190 ± 10 ⁽ⁱⁱ⁾ 210 ± 6 ^(iv)
²² O	14	205 ± 16	203 ± 16 ⁽ⁱ⁾ 206 ± 10 ⁽ⁱⁱ⁾ 206 ± 4 ^(iv)
²³ O	15	135 ± 32	133 ± 32 ⁽ⁱ⁾ 133 ± 10 ⁽ⁱⁱ⁾ 114 ± 9 ^(iv)
²¹ F	12	206 ± 32	204 ± 32 ⁽ⁱ⁾
²² F	13	203 ± 4	201 ± 4 ⁽ⁱ⁾ 183 ± 10 ⁽ⁱⁱⁱ⁾ 185 ± 14 ^(iv)
²³ F	14	211 ± 4	210 ± 4 ⁽ⁱ⁾ 196 ± 10 ⁽ⁱⁱⁱ⁾ 235 ± 4 ^(iv)
²⁴ F	15	158 ± 8	156 ± 8 ⁽ⁱ⁾ 122 ± 10 ⁽ⁱⁱⁱ⁾ 129 ± 4 ^(iv)
²⁵ F	16	121 ± 4	118 ± 4 ⁽ⁱ⁾ 117 ± 10 ⁽ⁱⁱⁱ⁾ 106 ± 8 ^(iv)
²⁶ F	17	156 ± 64	154 ± 64 ⁽ⁱ⁾ 121 ± 10 ⁽ⁱⁱⁱ⁾
²⁴ Ne	14	209 ± 16	207 ± 16 ⁽ⁱ⁾
²⁵ Ne	15	151 ± 8	149 ± 8 ⁽ⁱ⁾
²⁶ Ne	16	137 ± 8	135 ± 8 ⁽ⁱ⁾
²⁷ Ne	17	125 ± 16	122 ± 16 ⁽ⁱ⁾
²⁸ Ne	18	108 ± 16	105 ± 16 ⁽ⁱ⁾
²⁷ Na	16	162 ± 16	159 ± 16 ⁽ⁱ⁾

Table 4.1 Continued on next page.

Projectile	N	FWHM _{-n} ^g (MeV/c)	FWHM _{-n} ^{corrected} (MeV/c)
²⁸ Na	17	146 ± 32	143 ± 32 ⁽ⁱ⁾
²⁹ Na	18	140 ± 16	137 ± 16 ⁽ⁱ⁾
³⁰ Na	19	134 ± 16	130 ± 16 ⁽ⁱ⁾
³¹ Na	20	173 ± 64	170 ± 64 ⁽ⁱ⁾
³¹ Mg	19	161 ± 32	157 ± 32 ⁽ⁱ⁾
³² Mg	20	172 ± 32	167 ± 32 ⁽ⁱ⁾
³³ Mg	21	176 ± 32	172 ± 32 ⁽ⁱ⁾
³⁴ Al	21	184 ± 64	179 ± 64 ⁽ⁱ⁾
³⁵ Al	22	173 ± 64	168 ± 64 ⁽ⁱ⁾

Table 4.1: Widths of the longitudinal-momentum distributions measured for the one-neutron knockout fragments.

⁽ⁱ⁾ This work. FWHM_{-n}^g corresponds to Gaussian fits of the data and FWHM_{-n}^{corrected} was obtained after subtracting the contribution of the experimental resolution.

⁽ⁱⁱ⁾ Cortina *et al.* [Cor04].

⁽ⁱⁱⁱ⁾ Fernández PhD dissertation [Fer03].

^(iv) Sauvan *et al.* [Sau04].

^(v) Bazin *et al.* [Baz98].

^(vi) Baumann *et al.* [Bau98].

^(vii) Ozawa *et al.* [Oza08].

4.3 Inclusive cross-sections

The second physical observable measured in this experiment was the inclusive cross-section of the one-neutron knockout reaction, meaning that all the possible final states of the fragment were treated together. In the following sections, the calculation of this magnitude will be explained and the results will be presented.

4.3.1 Calculation of the inclusive cross-section

The total interaction cross-section, σ_t , expresses the likelihood of interaction between a projectile nucleus and a target. It is defined by Eq. 4.12,

$$I = I_0 e^{-\sigma_t n d} \quad (4.12)$$

where I_0 and I represent the number of incoming and non-reacting projectiles per unit of time, respectively, n is the number of target atoms per volume unit and d is the target thickness.

The one-neutron knockout cross-section, σ_{-n} , can be defined in analogy to Eq. 4.12:

$$I_0 - I_{-n} = I_0 e^{-\sigma_{-n} nd} \quad (4.13)$$

Here, I_{-n} denotes the number of nuclei that undergo a one-neutron knockout reaction per unit of time and $I_0 - I_{-n}$ corresponds to the number of nuclei that do not follow the one-neutron knockout channel.

It is possible to rewrite the previous formula as a function of the total number of incoming projectiles and emerging one-neutron knockout fragments, N_0 and N_{-n} , which were the quantities measured in this experiment.

$$N_0 - N_{-n} = N_0 e^{-\sigma_{-n} nd} \quad (4.14)$$

The cross-section can be then calculated as follows:

$$\sigma_{-n} = \frac{1}{nd} \ln \frac{N_0}{N_0 - N_{-n}} \quad (4.15)$$

The determination of the reaction channel in this experiment was explained in Section 4.1 and illustrated in Fig. 4.3. We made use of Z vs. A/Z identification plots and, for a given ${}^A X$ nucleus at F2, we selected the corresponding ${}^{A-1} X$ fragment at F4. The next step was to evaluate the number of projectiles impinging the target and the number of related one-neutron knockout events; i.e., the N_0 and N_{-n} previously mentioned.

- The number of projectiles, N_0 .
This was directly obtained from the number of nuclei within the corresponding geometrical cut at the F2 identification plot. It required a simple correction to account for the down-scaling of the acquisition trigger during the experiment.
- Number of one-neutron knockout events, N_{-n} .
We selected the one-neutron knockout events with simultaneous geometrical cuts at the F2 and F4 identification plots. However, the procedure was more complicated in this case because two additional corrections were needed. The first one reflected the fact that, due to the acceptance limits of the FRS, only part of the knockout fragments reached the final focal plane, where the detectors were located. The second correction was related to the detectors themselves, particularly, to the efficiency of the time-projection chambers at F4.

It should be noted that Eq. 4.15 only considers the presence of the knockout target. However, nuclear reactions may also occur in the surrounding materials and

this effect has to be corrected. By treating the different layers of matter as a compound target, it is possible to represent their contribution with the quantity $e^{-\tilde{\sigma}_{-n}\tilde{n}\tilde{d}}$ in Eq. 4.16.

$$N_0 - N_{-n} = N_0 e^{-\sigma_{-n}nd} e^{-\tilde{\sigma}_{-n}\tilde{n}\tilde{d}} \quad (4.16)$$

In order to evaluate $e^{-\tilde{\sigma}_{-n}\tilde{n}\tilde{d}}$, we made use of Eq. 4.17. The values of \tilde{N}_0 and \tilde{N}_{-n} were experimentally determined from measurements undertaken without the knockout target in the setup.

$$\tilde{N}_0 - \tilde{N}_{-n} = \tilde{N}_0 e^{-\tilde{\sigma}_{-n}\tilde{n}\tilde{d}} \quad (4.17)$$

Then, expressing $e^{-\tilde{\sigma}_{-n}\tilde{n}\tilde{d}}$ as a function of \tilde{N}_0 and \tilde{N}_{-n} and going back to Eq. 4.16, it was possible to work out σ_{-n} :

$$\sigma_{-n} = \frac{1}{nd} \ln \frac{N_0(\tilde{N}_0 - \tilde{N}_{-n})}{(N_0 - N_{-n})\tilde{N}_0} \quad (4.18)$$

The application of Eq. 4.18 reduced the cross-section values by approximately 30 %. Nevertheless, the low statistics accumulated in the absence of the reaction target prevented us from correcting this for much of the nuclei. Henceforth, we will mostly refer to the results obtained by means of Eq. 4.15.

4.3.2 Transmission correction

Only a percentage of the one-neutron knockout fragments produced at the F2 target were transmitted to the final focal plane of the FRS. As shown in Fig. 4.6, those nuclei with position and angle combinations outside the acceptance limits of the spectrometer were not detected. There was also a minor effect from the interaction of the nuclei with the layers of matter in the setup.

In order to obtain a correct value of the cross-section, it was crucial to consider the previous effect. For that purpose, we reproduced the experimental setup using a MOCADI simulation [Iwa97]. Then, we reconstructed the flight of the nuclei through the Fragment Separator and calculated the percentage that could reach the final focal plane. For each case, the parameters of the simulation were adjusted to reproduce the measured spatial and angular distributions at the intermediate and final focal planes. Appendix C contains a detailed compilation of the results. In previous works, the error affecting calculations of this kind was estimated to be about 10 % of the transmission value [Fer03].

Element	Z	ϵ_{TPCF4}
C	6	0.964 ± 0.002
N	7	0.956 ± 0.001
O	8	0.936 ± 0.002
F	9	0.894 ± 0.004
Ne	10	0.75 ± 0.01
Na	11	0.63 ± 0.03
Mg	12	0.42 ± 0.06
Al	13	0.23 ± 0.04

Table 4.2: Correction factors accounting for the detection efficiency of the TPCs at the final focal plane of the FRS.

4.3.3 Detection efficiency at F4

The detection efficiency at F4 was expected to be close to 100 %. However, the data indicated a different behaviour for the time-projection chambers, whose efficiency depended on the charge of the nuclei, with very low values for the highest Z. This effect was probably caused by an incorrect treatment of the time signals during the experiment. As a consequence, the position and shape of the control sum (see Section 3.3) depended on the charge of the nuclei. A fixed control-sum condition optimised for low Z values was used in this experiment, excluding a significant number of events associated to higher charges from the analysis.

In order to determine the appropriate correction factors and quantitatively evaluate the tracking efficiency at the final focal plane, we carefully studied the ratio of nuclei detected in the MUSIC that verified the control-sum condition in both TPC5 and 6 as a function of their charge, which was also measured in the MUSIC. This magnitude is called ϵ_{TPCF4} in Table 4.2. The results presented there are the averaged values obtained for different FRS settings. The associated errors correspond to the standard deviation of the sample.

4.3.4 Results for the inclusive knockout cross-sections

Sections 4.3.1–4.3.3 were devoted to explaining the calculation of the inclusive one-neutron knockout cross-section, σ_{-n} . In Section 4.3.1, we described how this calculation was based on the number of projectiles impinging the knockout target and on the number of one-neutron knockout reactions produced. Two additional corrections, related to the transmission of the fragments through the FRS, Section 4.3.2, and to the TPC detection efficiency at F4, Section 4.3.3, were required.

The results are shown in Table 4.3, where contribution of reactions occurring in

Projectile	N	σ_{-n} (mb)	Projectile	N	σ_{-n} (mb)
^{14}C	8	91 ± 9	^{23}F	14	88 ± 9
^{15}C	9	217 ± 23	^{24}F	15	127 ± 14
^{16}C	10	91 ± 19	^{25}F	16	102 ± 14
^{17}C	11	117 ± 15	^{26}F	17	110 ± 24
^{18}C	12	118 ± 14	^{24}Ne	14	71 ± 8
^{19}C	13	180 ± 32	^{25}Ne	15	94 ± 10
^{16}N	9	80 ± 9	^{26}Ne	16	107 ± 11
^{17}N	10	58 ± 6	^{27}Ne	17	102 ± 12
^{18}N	11	89 ± 9	^{28}Ne	18	70 ± 8
^{19}N	12	90 ± 10	^{27}Na	16	64 ± 8
^{20}N	13	105 ± 13	^{28}Na	17	76 ± 11
^{21}N	14	112 ± 16	^{29}Na	18	83 ± 9
^{22}N	15	137 ± 34	^{30}Na	19	89 ± 13
^{19}O	11	71 ± 7	^{31}Na	20	98 ± 14
^{20}O	12	83 ± 9	^{31}Mg	19	100 ± 21
^{21}O	13	100 ± 11	^{32}Mg	20	79 ± 15
^{22}O	14	103 ± 11	^{33}Mg	21	115 ± 25
^{23}O	15	160 ± 21	^{34}Al	21	102 ± 24
^{21}F	12	63 ± 7	^{35}Al	22	65 ± 18
^{22}F	13	85 ± 9			

Table 4.3: Inclusive one-neutron knockout cross-sections. The results are not corrected for reactions that occurred outside the target, in the surrounding layers of matter. This contribution would reduce the reported values by approximately 30 %.

Projectile	N	σ_{-n} (mb)	Projectile	N	σ_{-n} (mb)
^{16}C	10	63 ± 19	^{24}F	15	94 ± 15
^{17}C	11	72 ± 19	^{25}F	16	69 ± 15
^{18}N	11	64 ± 9	^{26}Ne	16	74 ± 11
^{19}N	12	65 ± 10	^{27}Ne	17	58 ± 12
^{20}N	13	71 ± 13	^{29}Na	18	59 ± 9
^{20}O	12	59 ± 9	^{30}Na	19	52 ± 14
^{21}O	13	72 ± 12	^{31}Mg	19	61 ± 19
^{22}O	14	68 ± 11	^{32}Mg	20	66 ± 14
^{23}F	14	62 ± 9			

Table 4.4: Inclusive one-neutron knockout cross-sections corrected for reactions taking place outside the target.

materials apart from the target is not accounted for. Those cases for which it was possible to correct this effect are presented in Table 4.4 and indicate that, on average, the cross-section values are reduced by approximately 30 %. Both in Tables 4.3 and 4.4, the errors were considered to be the contribution of three different sources, the experimental statistics and the errors associated with the transmission through the FRS and the TPC efficiency at F4.

4.4 Exclusive knockout cross-sections

The MINIBALL detector was used to measure the γ rays emitted in coincidence with the one-neutron knockout reaction. A compilation of those spectra with significant statistics, associated with $^{15-17}\text{C}$, $^{17-20}\text{N}$, $^{20-22}\text{O}$ and $^{22-25}\text{F}$ projectiles, can be found in Appendix D. There is no evidence of population of any excited fragment state in the one-neutron knockout of ^{24}F , $^{20,22}\text{O}$ and $^{16,15}\text{C}$. On the other hand, it must be noted that the moderate resolution of our measurements hindered deeper study of complex situations where numerous γ rays were produced in the de-excitation of the fragment. Therefore, we concentrated on the analysis of ^{17}C , ^{19}N , ^{21}O and ^{25}F one-neutron knockout, in which few γ lines were observed.

As described in Section 3.6.1, several corrections were needed in order to account for the MINIBALL efficiency and determine the real probability of populating each fragment state:

- The MINIBALL dead time, $\epsilon_{dead\ time}$, and the percentage of accepted γ triggers with non-null DGF signals, $\epsilon_{DGF,scaled}$. Both quantities were multiplied to obtain:

$$\epsilon_{total} = \epsilon_{dead\ time} \cdot \epsilon_{DGF,scaled} \quad (4.19)$$

This global factor depended on the spill time and is seen in Fig. 4.7 (left). The plot on the right represents the time structure of the knockout events, K , and was used to average ϵ_{total} and obtain, by means of Eq. 4.20, the final number applied to the data.

$$\epsilon = \frac{\sum_i \epsilon_{total,i} K_i}{\sum_i K_i} \quad (4.20)$$

The index i refers to the time intervals in which we divided the spill, with a length of 10^{-1} s.

- The geometrical and intrinsic efficiencies of MINIBALL. These were accounted for by means of detailed Geant 4 simulations, which included the effect of γ rays emitted by relativistic moving sources.

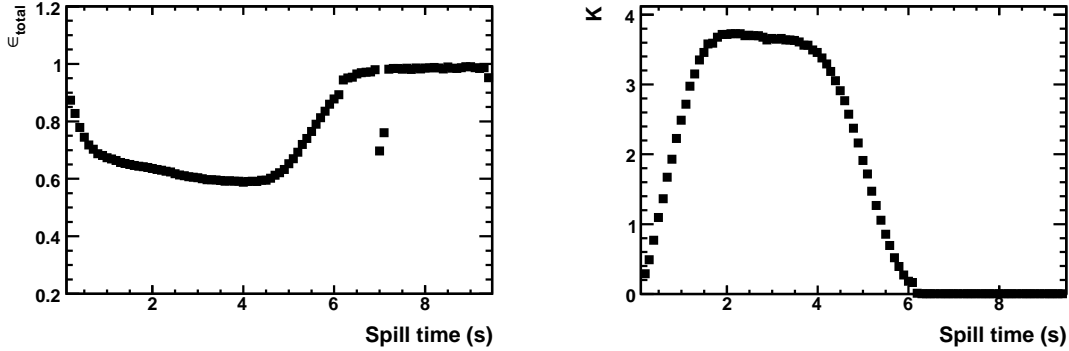


Figure 4.7: (Left) Efficiency correction calculated from the MINIBALL dead time and the percentage of accepted γ triggers with non-null DGF signals, $\epsilon_{total} = \epsilon_{dead\ time} \cdot \epsilon_{DGF, scaled}$. (Right) Time structure of the knockout events. K represents the number of events with a simultaneous trigger at the SCI_{F2} and SCI_{F4} scintillators, placed at the intermediate and final focal planes of the FRS, respectively.

In the Geant 4 simulation, the relative intensities associated with the different γ rays were free parameters whose values were selected to reproduce the experimental spectra. In order to compare the simulation with the data, we used a numerical calculation of χ^2 , looking for the γ -ray intensities that minimised this quantity.

From the γ -ray intensities, it was possible to determine the branching ratios, b , to the excited states of the knockout fragment. The associated errors varied between 6 and 25 % of the b value, including the contributions from both the simulation and the experimental statistics.

Next, the branching ratio to the ground state was calculated as,

$$b_{g.s.} = 1 - \sum_i b_i \quad (4.21)$$

where the index i refers to the excited states identified in this experiment¹.

Finally, the exclusive or partial cross-sections of each fragment state were determined to be the product of the corresponding branching ratio and the inclusive one-neutron knockout cross-section². In the error calculation, the contributions from these two quantities were taken into account.

¹Strictly speaking, the value resulting from this expression should be understood as an upper limit.

²The cross-section results that will appear in Sections 4.4.1–4.4.4 were corrected for those reactions produced outside the target.

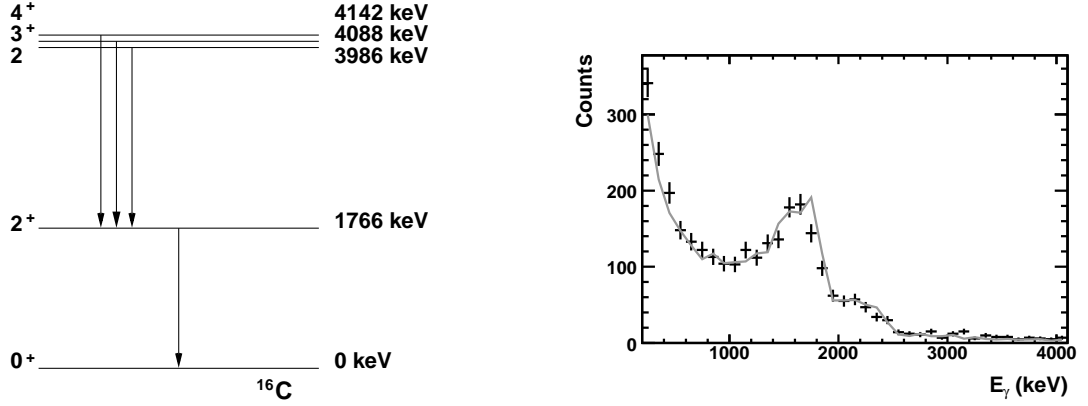


Figure 4.8: (Left) Level scheme of ^{16}C . (Right) Comparison between the simulated (grey line) and the measured (black markers) γ spectra for ^{17}C one-neutron knockout.

I^π	Energy (keV)	σ_{-n} (mb)	b
0^+	0	$23 \pm 8^{(i)}$	$0.32 \pm 0.08^{(i)}$
		$22 \pm 11^{(ii)}$	$0.19 \pm 0.09^{(ii)}$
2^+	1766	$31 \pm 10^{(i)}$	$0.43 \pm 0.07^{(i)}$
		$60 \pm 12^{(ii)}$	$0.52 \pm 0.08^{(ii)}$
$2, 3^+, 4^+$	~ 4000	$18 \pm 6^{(i)}$	$0.25 \pm 0.04^{(i)}$
		$33 \pm 7^{(ii)}$	$0.29 \pm 0.05^{(ii)}$

$\sigma_{-n}^{incl} = 72 \pm 19^{(i)}$
 $\sigma_{-n}^{incl} = 115 \pm 14^{(ii)}$

Table 4.5: Partial cross-sections and branching ratios for the populated states of ^{16}C . The cross-sections obtained in this work should not be directly compared with the results of Maddalena *et al.* due to the different beam energies used in both experiments.

⁽ⁱ⁾ This work.

⁽ⁱⁱ⁾ Maddalena *et al.* [Mad01]. The experiment was done at 60 MeV/nucleon with a C target.

4.4.1 Exclusive results for ^{17}C one-neutron knockout

One-neutron knockout of ^{17}C was previously studied by Maddalena and collaborators at the National Superconducting Cyclotron Laboratory, in Michigan [NSC], [Mad01]. The experiment was performed at 60 MeV/nucleon with a 228 mg/cm² Be target and the γ rays emitted by the ^{16}C fragment were measured by means of NaI(Tl) scintillators. The authors used the states and transitions indicated in the level scheme of Fig. 4.8 (left). The three levels around 4000 keV could not be resolved and were analysed together.

Maddalena and collaborators obtained a branching ratio of $19 \pm 9\%$ to the ground state, in disagreement with the 2% predicted by shell-model calculations. Moreover, they concluded $b = 52 \pm 8\%$ and $b = 29 \pm 5\%$ for the states at 1766

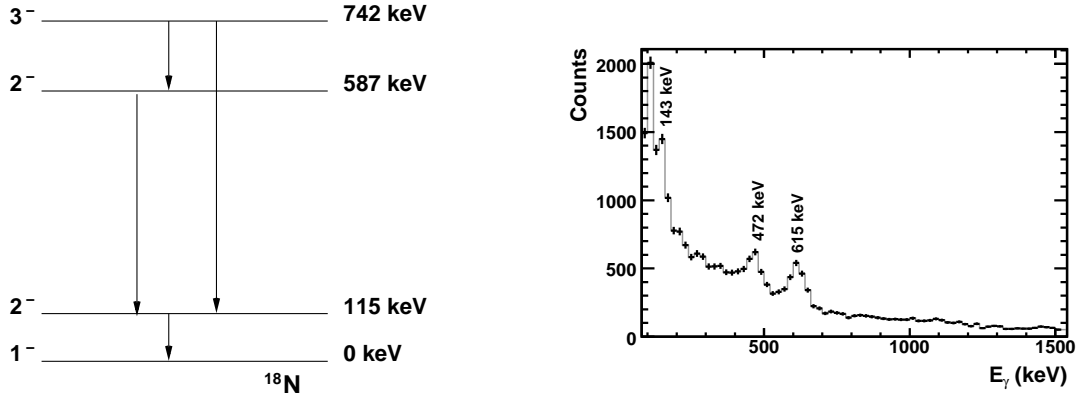


Figure 4.9: (Left) Level scheme of ^{18}N . (Right) γ spectrum measured in coincidence with ^{19}N one-neutron knockout.

and ~ 4000 keV, respectively. These results led to a unique assignment of the ^{17}C ground-state spin-parity, $J^\pi = 1/2^+$, elucidating the discussion between the $1/2^+$ and $3/2^+$ options found in the literature [Cur86, Duf86, War89].

Based on the level scheme proposed by Maddalena *et al.*, our calculations contemplate two γ rays with energies of 1766 and 2306 keV:

- The 1766 keV γ ray originates in the decay from the first 2^+ level to the ground state.
- The 2306 keV γ ray originates in the decay from the three unresolved levels near 4000 keV to the 2^+ state at 1766 keV.

The γ spectrum measured in this experiment is compared to the simulation that we used to obtain the MINIBALL efficiency and the feeding of the excited fragment states in Fig. 4.8 (right). Table 4.5 summarises the calculated branching ratios and partial cross-sections, comparing them with the results given by Maddalena *et al.*. We obtained a larger probability of feeding the ^{16}C ground state. However, considering the error bars and the low resolution of our γ spectrum, both experiments could be considered compatible. Our results confirm that there is a significant contribution from the ^{16}C ground state in the ^{17}C composition.

4.4.2 Exclusive results for ^{19}N one-neutron knockout

The low-energy levels of ^{18}N are displayed in Fig. 4.9 (left). The 2^- states at 115 and 587 keV were first populated by charge-exchange reactions [Nau80, Put83] and were later observed in a β -decay experiment [Pra91]. A higher level at 747 keV was

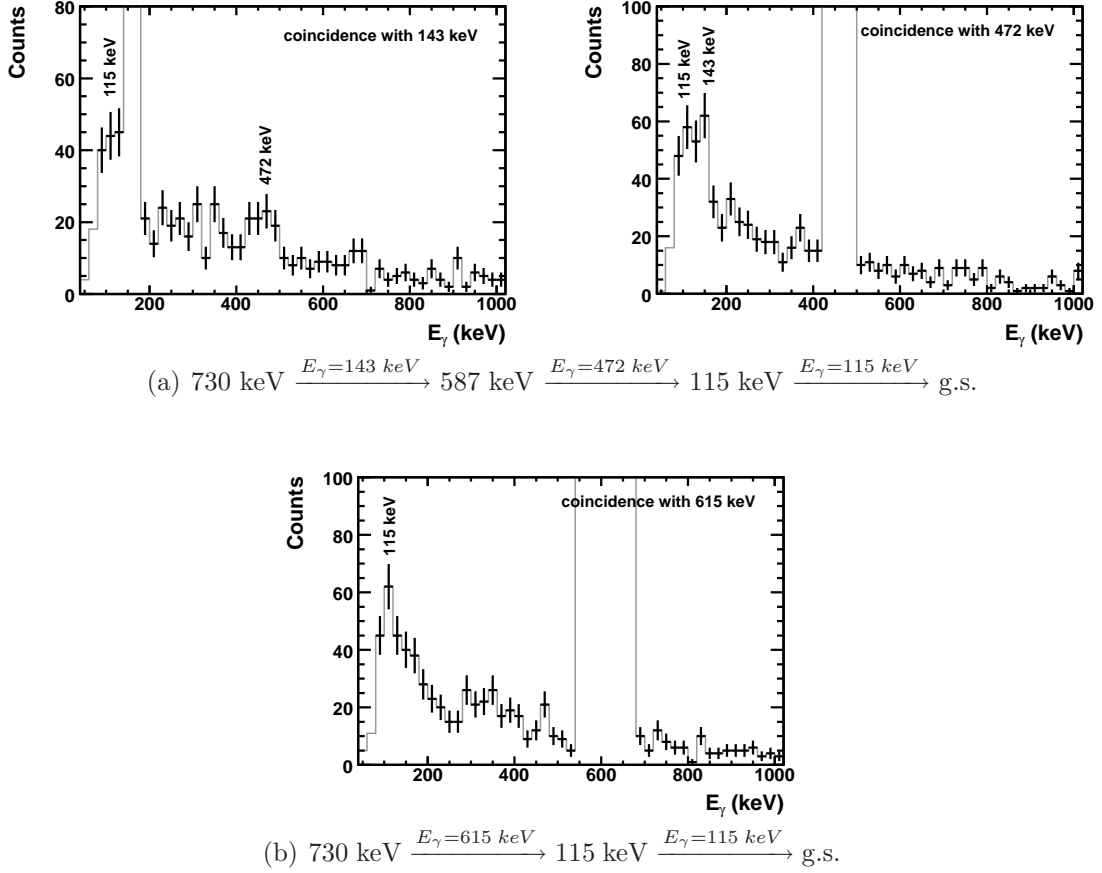


Figure 4.10: Coincidences between the three γ peaks observed in the one-neutron knockout of ^{19}N . These suggest two decay branches from the 3^- state, sited at 730 keV, namely, (a) and (b).

found in the work of Ref. [Put83] and is supported by recent fusion-evaporation data obtained at Lawrence Berkeley National Laboratory, in California [Ber], by Wiedeking and collaborators [Wie08]. Based on γ - γ coincidences, the authors suggest a placement at 742 keV and propose two transitions from this state, also represented in the scheme of Fig. 4.9.

In this work, we were able to measure the γ rays emitted in coincidence with the one-neutron knockout of ^{19}N . Fig. 4.9 (right) shows that it was possible to distinguish three clear peaks at 143, 472 and 615 keV. The coincidences between them are presented in Fig. 4.10 and locate the 3^- level of ^{18}N at 730 keV. According to our data, the decay from this state would follow two different branches:

- A cascade through the intermediate excited states, producing γ rays of 143, 472 and 115 keV.

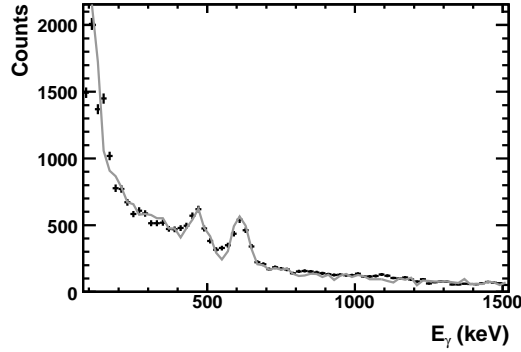


Figure 4.11: Comparison between the simulated (grey line) and the measured (black markers) γ spectra for ^{19}N one-neutron knockout.

I^π	Energy (keV)	σ_{-n} (mb)	b
2^-	587	$< 6 \pm 2$	$< 0.09 \pm 0.02$
3^-	730	$> 15 \pm 2$	$> 0.23 \pm 0.01$
$\sigma_{-n}^{incl} = 65 \pm 10$			

Table 4.6: Partial cross-sections and branching ratios for the populated states of ^{18}N .

- A decay to the first excited state, producing γ rays of 615 and 115 keV.

Both transitions are in good agreement with those published by Wiedeking *et al.* The difference of a few keV in the energy of the 3^- level can be easily explained by the resolution affecting our measurements, which limited the accuracy in the determination of the γ -peak positions to 20 keV.

Unfortunately, the lowest energy γ peaks, 115 and 143 keV, were partly mixed with the background and lay very close to the detection threshold. These facts prevented a quantitative analysis of the population of the different states. However, with the help of a Geant 4 simulation, it was possible to establish some upper and lower limits. The comparison between the experimental data and the simulation is displayed in Fig. 4.11. The results summarised in Table 4.6 indicate branching ratios to the excited states at 587 and 731 keV that are smaller than 0.09 ± 0.02 and larger than 0.20 ± 0.02 , respectively.

4.4.3 Exclusive results for ^{21}O one-neutron knockout

One-neutron knockout of ^{21}O was studied earlier at GSI by Fernández and collaborators [Fer03], who worked with high beam energies of about 1 GeV/nucleon. They

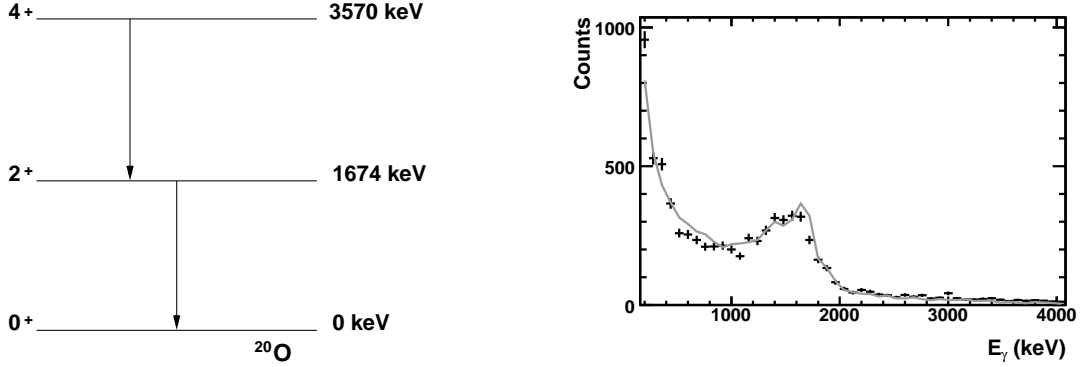


Figure 4.12: (Left) Level scheme of ^{20}O . (Right) Comparison between the simulated (grey line) and the measured (black markers) γ spectra for ^{21}O one-neutron knockout.

I^π	Energy (keV)	σ_{-n} (mb)	b
0^+	0	$20 \pm 5^{(i)}$	$0.28 \pm 0.06^{(i)}$
		$38 \pm 12^{(ii)}$	$0.53^{(ii)}$
2^+	1674	$35 \pm 6^{(i)}$	$0.48 \pm 0.04^{(i)}$
		$6.8 \pm 7.2^{(ii)}$	$0.09^{(ii)}$
4^+	3570	$17 \pm 4^{(i)}$	$0.24 \pm 0.04^{(i)}$
		$27 \pm 12^{(ii)}$	$0.38^{(ii)}$

$$\sigma_{-n}^{incl} = 72 \pm 12^{(i)}$$

$$\sigma_{-n}^{incl} = 71.9 \pm 8.9^{(ii)}$$

Table 4.7: Partial cross-sections and branching ratios for the populated states of ^{20}O . The results provided by Fernández *et al.* should be handled with discernment due to the impossibility of distinguishing the different excited states of ^{20}O in the γ spectrum measured by the authors. The beam energy used in that experiment should also be taken into account in order to compare the cross-section values with those obtained in this work.

⁽ⁱ⁾ This work.

⁽ⁱⁱ⁾ J. Fernández PhD dissertation [Fer03], the experiment was done at 1 GeV/nucleon with a C target.

used a C target surrounded by an NaI scintillator array that detected the γ rays emitted by the ^{20}O fragments produced in the reaction. The level scheme used by the authors is displayed in Fig. 4.12 (left) [Til98]. Two γ rays of 1674 and 1896 keV are emitted in the decay from the 2^+ level to the ground state and in the decay from the 4^+ to the 2^+ level, respectively.

Our calculations assumed the scheme in Fig. 4.12 as starting point. The superposition of the measured and the simulated γ spectra is shown in Fig. 4.12 (right). The calculated branching ratios and partial cross-sections are summarised in Table 4.5 and compared with the results of Ref. [Fer03]. There is a clear disagreement between

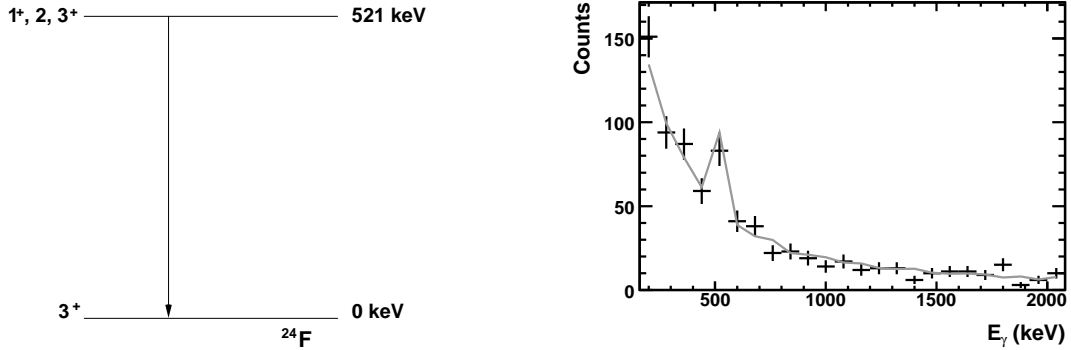


Figure 4.13: (Left) Level scheme of ^{24}F . (Right) Comparison between the simulated (grey line) and the measured (black markers) γ spectra for ^{25}F one-neutron knockout.

I^π	Energy (keV)	σ_{-n} (mb)	b
3^+	0	59 ± 13	0.85 ± 0.03
$1^+, 2, 3^+$	522	10 ± 3	0.15 ± 0.03
$\sigma_{-n}^{incl} = 69 \pm 15$			

Table 4.8: Partial cross-sections and branching ratios for the populated states of ^{24}F .

them which should be handled carefully. The spectrum measured by Fernández *et al.* shows a single peak where the 1674 and 1896 keV γ rays are completely mixed, thus increasing the uncertainty of their calculations.

4.4.4 Exclusive results for ^{25}F one-neutron knockout

According to the level scheme adopted for ^{24}F [Fir07], see Fig. 4.13 (left), a 522 keV γ ray is emitted in the decay from the first excited state of this nucleus. Fig. 4.13 (right) displays the experimental data obtained in this work. 522 keV γ rays were detected coinciding with the one-neutron knockout of ^{25}F projectiles, which indicates a certain probability of populating the first excitation level of ^{24}F in the reaction. The same plot also exhibits the simulated spectrum that led us to the results of Table 4.8. We estimated branching ratios of 0.85 ± 0.03 and 0.15 ± 0.03 that correspond to the ^{24}F ground state and first excitation level, respectively.

Chapter 5

Discussion of the results

This chapter will be devoted to the discussion and interpretation of the results presented in Sections 4.2, 4.3 and 4.4. In order to effectively treat the significant amount of data collected in this experiment, the exposition will be divided into several parts and will focus on certain isotopic chains.

The general trend of the inclusive one-neutron knockout cross-sections and longitudinal-momentum distributions will be analysed as a function of the neutron number. Momentum distributions are extremely sensitive to the orbital angular momentum of the neutron removed in the reaction, with a FWHM that is remarkably narrower for $l = 0, 1$ than for $l = 2$. This behaviour will be carefully explained in Section 5.3.1 and will be used to distinguish different l components in the ground state of the analysed projectiles.

We will be able to identify relevant structural phenomena such as the formation of one-neutron halos in odd-mass C isotopes, the effects that appear for N, O and F nuclei above $N = 14$ and the particularities of the ground-state configuration for neutron-rich Ne isotopes.

Proximity to what is known as the *island of inversion* and the current lack of data in this region motivated a deeper analysis of the Ne isotopic chain. Detailed calculations of the longitudinal-momentum distributions were performed in order to clarify the different single-particle contributions to the ground state of these nuclei.

5.1 Results for $^{14-19}\text{C}$

The low binding energies and diffuse neutron distributions make odd-mass C isotopes good candidates for neutron-halo configurations, a form of nuclear matter that appears in loosely bound systems and where the valence neutron(s) wave function extends far beyond the standard nuclear radius. As the binding energies become

smaller in the vicinity of the drip-line, the valence neutron or neutrons tunnel out of the central potential, enhancing the diffuseness at the nuclear surface. Eventually, this leads to a de-localization that looks like a kind of halo surrounding the core of the nucleus. The appearance of such a configuration is determined by the height of the potential barrier, which itself depends on the binding energy and the orbital angular momentum¹. As the centrifugal barrier lowers the probability of tunnelling to larger radii, the halo formation requires smaller angular momentums and occurs most likely for s and p states.

Neutron-removal experiments such as the one described in this dissertation constitute a suitable tool for the investigation of neutron-halo nuclei. The cross-section of the one-neutron knockout process is expected to undergo a significant increase and valuable information about the halo wave function can be extracted from the momentum distribution of the core fragments, see Section 1.2. According to the Heisenberg uncertainty principle, the spatial spread of the halo would result in a narrow distribution when translated into momentum coordinates [Kob88].

Fig. 5.1 displays the inclusive results obtained in this work. The experimental one-neutron knockout cross-sections and the widths of the measured longitudinal-momentum distributions are represented as a function of the neutron number in the projectile. The one-neutron separation energies given in the literature are also included as complementary data. We will use these results to discuss the structural properties of neutron-odd C isotopes, namely, ^{15,17,19}C.

First, we will consider the case of ¹⁵C. The measured momentum distribution should be treated carefully due to the limited transmission of the ¹⁴C fragments through the FRS spectrometer and the resulting acceptance cuts, see Fig. B.1. Although this circumstance could affect the FWHM value, there is no doubt about the narrowing of the distribution, which corresponds to the crossing of the $N = 8$ shell and the dominance of a $1s_{1/2}$ intruder configuration. The cross-section also undergoes a clear increase that, combined with a large $1s_{1/2}$ admixture, a very narrow momentum distribution and a relatively weak binding of the last neutron, $S_n = 1218 \pm 8$ keV [Aud97], may indicate a spatial de-localization of the valence-neutron orbital, which has been suggested in other works [Baz95, Baz98].

The possibility of a halo configuration was discussed in greater detail by Sauvan *et al.* in a previous one-neutron knockout experiment [Sau00, Sau04]. In their results, the authors also found reasonable indications of a halo structure. However, the situation remains unclear due to contradictory measurements of the ¹⁵C total-interaction cross-section, which show no effect [Oza98, Lia90] and minor enhancements [Fan00, Vil91]. Despite the predominant $l = 0$ character of the valence

¹For protons, the height of the barrier also depends on the Coulomb potential, which is why proton halos are expected to be less common than those made up of neutrons.

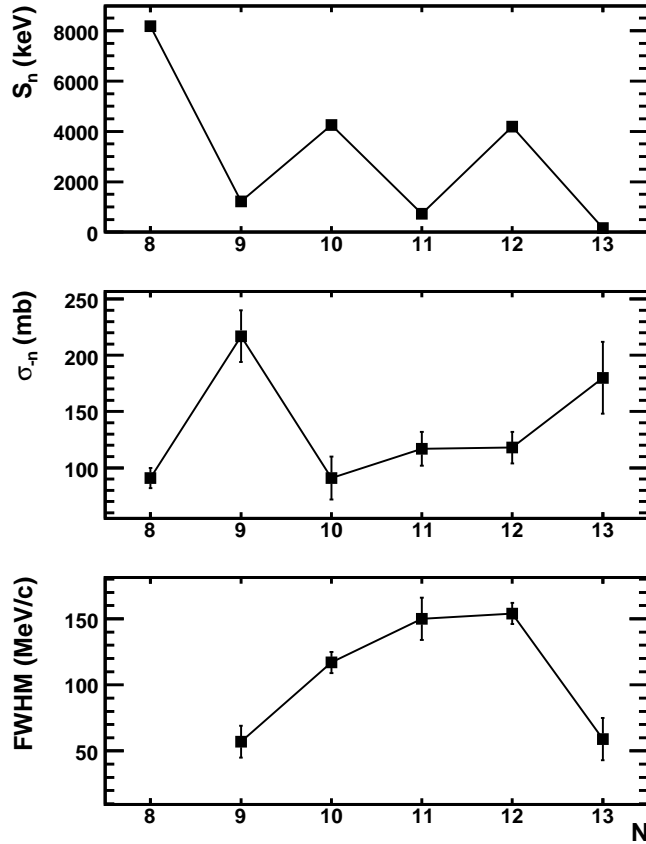


Figure 5.1: Inclusive results for $^{14-19}\text{C}$. Starting from the top: the one-neutron separation energies, S_n , the one-neutron knockout cross sections, σ_n , and the FWHM of the fragment longitudinal-momentum distributions are represented as a function of the neutron number in the projectile, N .

neutron, its binding energy, which exceeds 1 MeV, could restrict the spatial extent of the density distribution².

The next odd-mass isotope is ^{17}C . Even though it has a low one-neutron separation energy, $S_n = 728 \pm 17$ keV [Aud97], the broad momentum distribution and the small cross-section measured in this work suggest no halo formation. The enhanced width of the momentum distribution indicates a $l = 2$ nature of the valence neutron. A more accurate picture can be obtained from the exclusive results presented in Section 4.4.1, according to which the ^{17}C ground-state is dominated, with a probability of 43 ± 7 %, by a $^{16}\text{C}(2^+) \otimes 0d_{5/2}$ component. Such a configuration, where a $0d_{5/2}$ neutron is coupled to the first 2^+ state of ^{16}C , at 1766 keV, is associated with a high effective separation energy³, $S_n^{eff} = 2494$ keV, and with an increase of the

²The one-neutron separation energy of ^{15}C , $S_n = 1218 \pm 8$ keV, should be compared with those of ^{17}C , $S_n = 728 \pm 17$ keV, and ^{19}C , $S_n = 160 \pm 11$ keV.

³When we work with a separation energy of 728 keV, we assume that the ground state of ^{16}C is

centrifugal barrier, which explain the observed halo suppression.

Previous one-neutron knockout experiments led to similar conclusions concerning the ground-state of ^{17}C and allowed to clarify its spin-parity, $J^\pi = 3/2^+$ [Baz98, Mad01, Sau00, Sau04]. In particular, Maddalena *et al.* were able to identify and quantify contributions from three different components [Mad01]. The main one, $^{16}\text{C}(2^+) \otimes 0d_{5/2}$, would account for the dominant $l = 2$ and smaller admixtures of $^{16}\text{C}(2^+) \otimes 1s_{1/2}$ and $^{16}\text{C}(0^+) \otimes 0d_{3/2}$ would complete the representation. The authors found a difficulty associated with the one-neutron knockout of ^{17}C to the ground state of ^{16}C . They measured a branching ratio of $19 \pm 9\%$, which is noticeably larger than the theoretical prediction. In Section 4.4, we extracted a value of $32 \pm 8\%$ which supports these results.

We will close this section with the case of ^{19}C , a nucleus that has attracted much attention due to its remarkably low one-neutron separation energy, $S_n = 160 \pm 11$ keV [Aud93]⁴, understood as a possible indication of a well-developed one-neutron halo. ^{19}C stands out in Fig. 5.1, the measured cross-section is noticeably increased with respect to the neighboring isotope and the FWHM of the fragment momentum distribution undergoes a reduction by a factor larger than 2. Both observations can be interpreted as a reliable signature of the halo configuration and indicate a remarkable $l = 0$ character of the valence neutron.

Although experimental clues regarding larger separation energies have been found [Nak99, Mad01], the one-neutron halo of ^{19}C has been confirmed over the years by several works that have placed the structure of this nucleus far from the simple shell-model predictions [Bau98, Baz95, Mar96], in which the last neutron would occupy a $0d_{5/2}$ orbit. The role of $1s_{1/2}$ and $0d_{5/2}$ neutrons coupled to the 0^+ (g.s.) and 2^+ (1620 keV) states of the ^{18}C core has been extensively discussed in the literature [Baz95, Baz98]. The Coulomb dissociation experiment published by Nakamura *et al.* [Nak99] allowed a definitive spin-parity assignment, $J^\pi = 1/2^+$, and indicated a leading $^{18}\text{C}(0^+) \otimes 1s_{1/2}$ component. A few years later, further works appeared that supported these conclusions [Cor01, Mad01].

directly populated when we remove the last neutron of ^{17}C . If this is not the case and the reaction feeds the first 2^+ state of ^{16}C , at 1766 keV, we should consider an effective separation energy, where $S_n^{eff} = 728 + 1766 = 2494$ keV.

⁴This number represents the weighted average of measurements carried out at Los Alamos and GANIL [Orr91, Wou88]. The value $S_n = 240$ keV, frequently used in the literature, includes two earlier and less precise results.

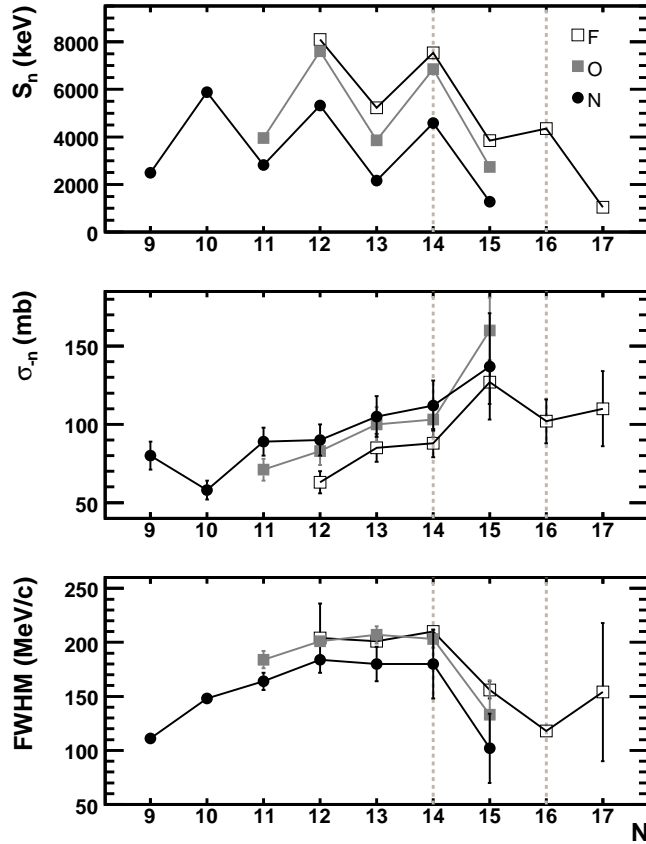


Figure 5.2: Inclusive results for $^{16-22}\text{N}$, $^{19-23}\text{O}$ and $^{21-26}\text{F}$. Starting from the top: the one-neutron separation energies, S_n , the one-neutron knockout cross sections, σ_n , and the FWHM of the fragment longitudinal-momentum distributions are represented as a function of the neutron number in the projectile, N .

5.2 Results for $^{16-22}\text{N}$, $^{19-23}\text{O}$ and $^{21-26}\text{F}$

The results concerning $^{16-22}\text{N}$, $^{19-23}\text{O}$ and $^{21-26}\text{F}$ are displayed in Fig. 5.2. There, a clear effect becomes visible when crossing $N = 14$, with a significant reduction in the width of the fragment longitudinal-momentum distribution and a larger one-neutron knockout cross-section. Such behaviour can be understood within the simplest shell-model picture. For neutron numbers $N = 8$ to 14 , the valence neutrons would occupy a $0d_{5/2}$ orbit, while, for $N = 15-16$, they would stay in a $1s_{1/2}$ level. This change from $l = 2$ to $l = 0$ configurations explains the narrowing of the momentum distributions. The enhanced cross-sections could generally be attributed to the combination of weaker binding energies and large $1s_{1/2}$ admixtures, where the core levels are completely filled up to $0d_{5/2}$ and there is a single neutron in a $1s_{1/2}$ orbital.

It is important to comment on the case of ^{22}N , which has been proposed as a one-neutron halo candidate [Gup00, Oza00, Soh08]. We have presented the first

one-neutron knockout data obtained for this nucleus. Although the situation is not so clear as for ^{19}C and we cannot make a definitive statement about the neutron spatial distribution, our results provide worthwhile structural information and suggest a significant weight for the $1s_{1/2}$ configuration.

The reported effect above $N = 14$ was earlier observed for ^{23}O and $^{24,25}\text{F}$ in the works of Refs. [Fer03, Sau00]. However, controversy surfaced in relation to the ^{23}O structure. The simple picture of a $1s_{1/2}$ neutron coupled to the ground state of the core would point to $J^\pi = 1/2^+$. A different configuration with a modified ^{22}O core and $J^\pi = 5/2^+$ was proposed by Kanungo *et al.* [Kan02]. The authors based their conclusion on the analysis of the fragment longitudinal-momentum distributions measured in one- and two-neutron removal reactions. The validity of this interpretation was discussed by Brown and collaborators [Bro03] and was conclusively rejected by experimental data containing detailed spectroscopic information [Cor04, Fer03]. A dominant $^{22}\text{O}(0^+) \otimes 1s_{1/2}$ single-particle configuration was confirmed and the spin-parity of the ground state was established as $J^\pi = 1/2^+$. Additional support for this conclusion was provided by the work of Ref. [Sau04] and by a later Coulomb-breakup experiment carried out at GSI [Noc05].

Finally, ^{26}F also deserves a specific comment. The line $N = 16$ is crossed, the binding energy suffers a significant reduction, $S_n = 1050 \pm 15$ keV [Aud95], and the traditional shell model predicts a rather stable core, where the neutron levels are completely filled up to $1s_{1/2}$ and coupled to a single valence neutron that is in a $0d_{3/2}$ orbit. Nevertheless, a previous one-neutron knockout experiment showed a low cross-section and a narrow momentum distribution, $\text{FWHM} = 121 \pm 10$ MeV/c, that seem to contradict this hypothesis [Fer03]. The authors interpreted these two facts as a possible indication of a different structure where we would find an excited ^{25}F core and a $1s_{1/2}$ valence neutron. The FWHM value obtained in this work is slightly higher, 154 ± 64 MeV/c, but still compatible within the error bar. Neither did we observe any significant increase of the cross-section, which was almost equal to the one measured for ^{25}F projectiles. Both observations could support the conclusions of Ref. [Fer03] and indicate a strong $1s_{1/2}$ component.

5.3 Results for $^{24-28}\text{Ne}$

In recent years, numerous studies have looked into the $N \sim 20$ neutron-rich region of the nuclear landscape, where several indications of new structural phenomena have been found. Of great interest is the disappearance of the traditional $N = 20$ magicity observed for sodium and magnesium isotopes [Dét78, Mot95]. Considerable efforts have been made by the scientific community to explain the vanishing of the $N = 20$ shell closure. Early explanations suggested a collapse in the usual ordering of the single-particle states [Sto83, Wil80]. Later on, different models appeared, some of

them based on $2p - 2h$ states that may intrude below the normal spherical states and originate what is known as the *island of inversion*. As an alternative approach, the two lower pf orbits were added to the sd space in the Monte Carlo Shell Model calculations⁵ [Ots01c, Uts99], allowing the mixing of sd and pf configurations and providing a reasonable description of the experimental data [Uts04]. This last theory predicts a rapidly decreasing shell gap at $N = 20$ that would cause a wider *island of inversion*. The crossing between intruder and normal configurations would take place at $N = 18$, resulting in deformed ground states already at this neutron number and giving rise to the appearance of low-energy intruder states up to $N = 17$ [Dom06].

The vanishing of magicity at $N = 20$ has also been related to a new shell gap at $N = 16$ that converts ^{24}O into a doubly magic nucleus [Oza00, Sta04], as confirmed by the recent work of Kanungo *et al.* [Kan09]. From a simple point of view, such behaviour could be explained by the migration of the $0d_{3/2}$ neutron orbit towards the pf shell and the consequent distancing of the $1s_{1/2}$ and $0d_{3/2}$ sub-shells. Otsuka *et al.* use the lack of attractive interaction between $0d_{3/2}$ neutrons and $0d_{5/2}$ protons to describe this phenomenon. It must be noted that the $0d_{5/2}$ proton level is empty for ^{24}O [Ots01a].

The presence of a new shell closure at $N = 16$ might be also supported by the fact that ^{22}C , ^{23}N and ^{24}O are the last bound nuclei of their respective isotopic chains or by the break in neutron-separation energy systematics observed for ^{28}Mg and ^{26}Ne [Obe05].

These antecedents locate $^{24-28}\text{Ne}$ in a transient region for nuclear structure and make its investigation especially attractive. A brief overview of the information available concerning neutron-rich Ne isotopes will be helpful for the discussion of our results:

^{25}Ne , $J^\pi = 1/2^+$

Recent experiments established the spin-parity of the ^{25}Ne ground state, $J^\pi = 1/2^+$, and outlined a possible scheme of the low-lying energy levels. Three

⁵The Monte Carlo Shell Model (MCSM) was developed to overcome the limitations of conventional shell model calculations, where the large dimension of the valence-nucleon Hilbert space prevents the diagonalization of the Hamiltonian matrix. The MCSM approach is based on the Quantum Monte Carlo Diagonalization method (QMDM), which uses a simplified Hamiltonian matrix. Only those basis states that are important for the *eigenstate* of interest are selected. If this step is done properly, the results provide a good approximation to the exact diagonalization in the entire Hilbert space. For a review, see Ref. [Ots01a].

When working with neutron-rich nuclei in the $N \sim 20$ region, two main effective interactions should be mentioned. The first is known as USD and accounts for the sd shell [Bro88]. However, in order to understand the *island of inversion*, it is also necessary to include at least part of the pf shell as orbits where the nucleons are active [Uts99]. The interaction used in $sd - pf$ calculations is called SDPF-M.

states were found at 1703, 2090 and 3316 keV, with $J^\pi = 5/2^+$, $3/2^+$ and $5/2^+$ [Fer07, Obe06, Ter06]. These results are in good agreement with previous β -decay experiments [Pad05, Ree99] and are consistent with both USD and SDPF-M Monte Carlo Shell Model predictions. It is also interesting that the decay from the 3316 keV level occurs throughout the first excited state, at 1703 keV.

^{26}Ne , $J^\pi = 0^+$

γ spectroscopy of ^{26}Ne was performed in a fragmentation experiment [Bel05] and the level scheme proposed for this nucleus is in good agreement with calculations in the sd shell model space. ^{26}Ne has also been investigated by means of the one-neutron knockout technique [Ter06]. The ground state of ^{25}Ne and the excited levels at 1703, 2090 and 3316 keV were populated in the reaction. The corresponding branching ratios were extracted from the coincident γ spectrum and the exclusive momentum distributions were determined. This last observable indicated the removal of a $l = 0$ neutron in those reactions leading to the core ground state and an angular momentum $l = 2$ related to the occupation of the 1703 and 3316 keV levels. Although statistics did not allow for a similar analysis of the few events populating the 2090 keV state, the authors used Refs. [Cat05a, Pad05] to deduce a $l = 2$ contribution. The results indicate the following ground-state structure for ^{26}Ne :

$$\begin{aligned} &(43 \%) \ ^{25}\text{Ne}(1/2^+, \text{g.s.}) \otimes s_{1/2} \\ &(26 \%) \ ^{25}\text{Ne}(5/2^+, 1703 \text{ keV}) \otimes d_{5/2} \\ &(22 \%) \ ^{25}\text{Ne}(5/2^+, 3316 \text{ keV}) \otimes d_{5/2} \\ &(9 \%)^6 \ ^{25}\text{Ne}(3/2^+, 2090 \text{ keV}) \otimes d_{3/2} \end{aligned}$$

^{27}Ne , $J^\pi = 3/2^+$

The β -decay properties of ^{27}Ne were studied in the work of Ref. [Tri06], showing good agreement with sd shell model calculations and no evidence of any anomalous behaviour. These data also support the $3/2^+$ ground-state assumption for this nucleus, which was based on systematics. Other experimental works led to the discovery of two ^{27}Ne states at 765 and 885 keV, with $3/2^-$ and $1/2^+$ spin-parity. The $3/2^-$ state is not predicted by calculations in the sd space and suggests an intruder configuration [Dom06, Obe06, Ter06].

^{28}Ne , $J^\pi = 0^+$

Spectroscopic measurements of ^{28}Ne located its first excited state at 1293 keV, with $J^\pi = 2^+$. This low energy value was found to be in disagreement with

⁶The spin-parity of the excited ^{25}Ne level at 2090 keV has not been clearly established. Different values are found in the literature, namely, $3/2^+$, $7/2^-$ and $3/2^-$. We excluded cases with negative parities because they would not be compatible with the $l = 2$ assumption.

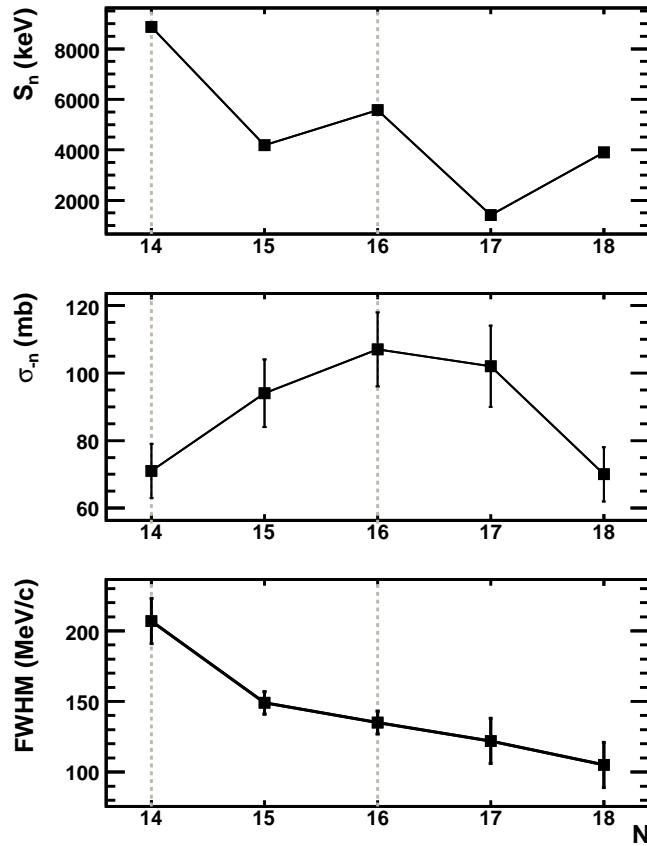


Figure 5.3: Inclusive results for $^{24-28}\text{Ne}$. Starting from the top: the one-neutron separation energies, S_n , the one-neutron knockout cross sections, σ_{-n} , and the FWHM of the fragment longitudinal-momentum distributions are represented as a function of the neutron number in the projectile, N .

sd calculations and could only be understood in the extended $sd - pf$ model [Bel05, Dom06]. It might also point to a reduced $N = 20$ shell gap. The one-neutron knockout of this nucleus was carefully analysed by Terry *et al.* [Ter06]. The $3/2^-$ and $1/2^+$ states of ^{27}Ne at 765 and 885 keV were populated in the reaction and the exclusive fragment momentum distributions were determined. They suggested the removal of a $l = 0, 1$ neutron and excluded the $l = 2$ possibility. The work of Terry and collaborators suggests the following ground-state configuration for ^{28}Ne :

$$\begin{aligned}
 &(32 \%) \ ^{27}\text{Ne}(3/2^+, \text{g.s.}) \otimes d_{3/2} \\
 &(15 \%) \ ^{27}\text{Ne}(3/2^-, 765 \text{ keV}) \otimes p_{3/2} \\
 &(53 \%)^7 \ ^{27}\text{Ne}(1/2^+, 885 \text{ keV}) \otimes s_{1/2}
 \end{aligned}$$

⁷The spin-parity of the excited ^{27}Ne level at 885 keV has not yet been established. Among the different values treated in the literature, $1/2^+$, $7/2^-$ and $5/2^-$, we have selected the only possibility

Fig. 5.3 summarises the inclusive results obtained in this dissertation, where both $N = 14$ and 16 lines were crossed. According to an elementary single-particle description within the traditional shell model, the last neutron in $^{24-28}\text{Ne}$ projectiles would occupy different orbits, namely, ^{24}Ne ($0d_{5/2}$), $^{25-26}\text{Ne}$ ($1s_{1/2}$) and $^{27-28}\text{Ne}$ ($0d_{3/2}$). The validity of this simple picture could be investigated by an appropriate analysis of the momentum distributions measured for the one-neutron knockout fragments. Specifically, the associated FWHM values would provide us with rough identification of $l = 0$ and $l = 2$ components.

A quick look at Fig. 5.3 is enough to appreciate a FWHM reduction at $N = 14$. This is the same effect discussed in Section 5.2 for ^{22}N , ^{23}O and $^{24,25}\text{F}$. It corresponds to the change from $0d_{5/2}$ to $1s_{1/2}$ configurations.

The filling of the $0d_{3/2}$ orbit is expected at $N = 16$ and should enhance the widths of the measured momentum distributions. However, the behaviour of the $^{27-28}\text{Ne}$ isotopes seems to contradict this hypothesis. Further study of the $^{24-28}\text{Ne}$ isotopic chain will be carried out in the next section in order to develop a more accurate description of their ground-state structure. The experimental momentum distributions will be carefully analysed with the help of theoretical calculations and will be used to identify different *core* \otimes *neutron* contributions.

5.3.1 Single-particle content from longitudinal-momentum distributions

In the early seventies, the momentum distributions of projectile fragments were extensively studied for well-bound stable nuclei [Gre75] and phenomenologically described by Gaussian profiles. A simple model developed by Goldhaber [Gol74] connected the widths of the distributions with the Fermi momentum, k_F , through Eq. 5.1,

$$\sigma = \sigma_0 \sqrt{\frac{A_f(A_p - A_f)}{A_p - 1}}; \quad \sigma_0 = \frac{k_F}{\sqrt{5}} \quad (5.1)$$

where A_f and A_p represent the fragment and projectile mass numbers.

Later on, the fragmentation model proposed by Friedman [Fri83] related the width of the distributions to the separation energy of the removed nucleons and to a cut-off radius that was introduced due to the requirement of fragment survival. However, this model failed in the description of exotic nuclei, such as those exhibiting halo configurations, and needed to be modified.

that is compatible with the angular momenta proposed in Ref. [Ter06], namely, $l = 0, 1$. The $l = 1$ possibility was also excluded because it cannot lead to the correct parity for the ^{28}Ne ground state.

Henceforward, we will restrict ourselves to the single-nucleon knockout context and will study the longitudinal-momentum distributions measured for $A - 1$ fragments. These are less affected by the reaction mechanism and easier to interpret than the transverse components [Ber92]. Only reactions on light targets will be considered, so that contributions from Coulomb dissociation can be neglected.

As we explained in Section 1.2, stripping is the dominant process in the high-energy regime. Modern works frequently assume that the target is *transparent* to the core fragment and recur to the Serber mechanism [Ser47] to identify the fragment momentum distribution with that of the removed nucleon in the initial state inside the projectile. However, several authors noted that this interpretation does not hold in general because not all parts of the spatial wave function are explored with equal probability [Bro96, Esb96]. The observed momentum distributions are mainly determined by the asymptotic form of the wave function [Aum98, Sim07], $r \rightarrow \infty$, which, for a neutron with angular momentum l , can be written as follows:

$$\psi_{lm}(\mathbf{r}) \propto \kappa^{3/2} h_l(i\kappa r) Y_{lm}(\theta, \phi) \quad (5.2)$$

θ and ϕ correspond to the polar and azimuthal angles, r is the module of the vector that connects the core centre of mass with the valence nucleon and $h_l(i\kappa r)$ represents the first spherical Hankel function. The parameter κ can be expressed in terms of the neutron-separation energy, S_n , and the reduced mass of the core-neutron system, μ , according to Eq. 5.3.

$$\kappa = \sqrt{2\mu S_n} \quad (5.3)$$

In order to obtain the probability distribution in the momentum space⁸ along the longitudinal z axis, the square Fourier transform of the wave function must be integrated over the transverse coordinates. This leads us to Eq. 5.4.

$$\frac{dN}{dk_z} \propto \int \exp[ik_z(z - z')] \psi(x, y, z) \psi^*(x, y, z') dx dy dz dz' \quad (5.4)$$

The requirement of fragment survival is accounted for by means of a lower cut-off parameter in the wave function, x_0 , that acts perpendicularly to the beam direction. Interactions inside this region would result in destruction of the fragment. In this situation, it is possible to obtain simple analytical expressions for the lowest three angular momenta [Han96, Sme98],

$$\frac{dN_{l=0}}{dk_z} = \frac{A_{0j}^2 x_0^2 \kappa}{2\pi} \left\{ K_1^2(\xi) - K_0^2(\xi) \right\} \quad (5.5)$$

⁸We will work in terms of the wave vector $\mathbf{k} = \frac{\mathbf{p}}{\hbar}$.

$$\frac{dN_{l=1}}{dk_z} = \frac{A_{1j}^2 x_0^2}{2\pi\kappa} \left\{ k_z^2 [K_1^2(\xi) - K_0^2(\xi)] + (k_z^2 + \kappa^2) [K_2^2(\xi) - K_1^2(\xi) - \frac{2}{\xi} K_1(\xi) K_2(\xi)] \right\} \quad (5.6)$$

$$\begin{aligned} \frac{dN_{l=2}}{dk_z} = \frac{A_{2j}^2 x_0^2}{8\pi\kappa^3} \left\{ (3k_z^2 + \kappa^2)^2 [K_1^2(\xi) - K_0^2(\xi)] + 12k_z^2 (k_z^2 + \kappa^2) [K_2^2(\xi) - K_1^2(\xi) - \right. \\ \left. - \frac{2}{\xi} K_1(\xi) K_2(\xi)] + 3(k_z^2 + \kappa^2)^2 [K_3^2(\xi) - K_2^2(\xi) - \frac{4}{\xi} K_2(\xi) K_3(\xi)] \right\} \end{aligned} \quad (5.7)$$

where A_{lj} is a dimensionless coefficient that we assumed equal to one and the argument of the modified Bessel functions, $K_i(\xi)$, with $i = 0-3$, is given by Eq. 5.8.

$$\xi = x_0 \sqrt{k_z^2 + \kappa^2} \quad (5.8)$$

Eqs. 5.5–5.7 depend simply on the neutron-separation energy, see Eq. 5.3, and on the selected cut-off parameter, x_0 . They are useful tools for estimating the widths and shapes of the longitudinal-momentum distributions in nuclear breakup experiments. As it will be seen next, s and d waves can easily be distinguished from each other due to the significant difference in their characteristic widths.

In the analysis of Ne isotopes, we assumed a simplified structure that was uniquely based on two different components⁹, as shown in Eq. 5.9,

$$Projectile = W_{gs}(core \otimes neutron)_{gs} + W_{exc}(core \otimes neutron)_{exc} \quad (5.9)$$

The coefficients W_{gs} and W_{exc} would account for the weights of each $core \otimes neutron$ configuration, where gs and exc refer to the ground state and an excited level of the core. Our main goal was to determine their respective values.

Eqs. 5.5–5.7 reflect how the angular momentum of the valence neutron, l , and the neutron-separation energy are closely related to the momentum distribution of the knockout fragment. This behaviour allowed us to determine W_{gs} and W_{exc} from a simple fit of the measured momentum distributions, where we used an admixture of two l components that would be coupled to different core states. The situation is specified below by Eq. 5.10.

$$\frac{dN}{dk_z} = W_{gs} \left(\frac{dN_l}{dk_z} \right)_{gs} + W_{exc} \left(\frac{dN_l}{dk_z} \right)_{exc} \quad (5.10)$$

⁹The stability of our calculations limited the number of components that could be included.

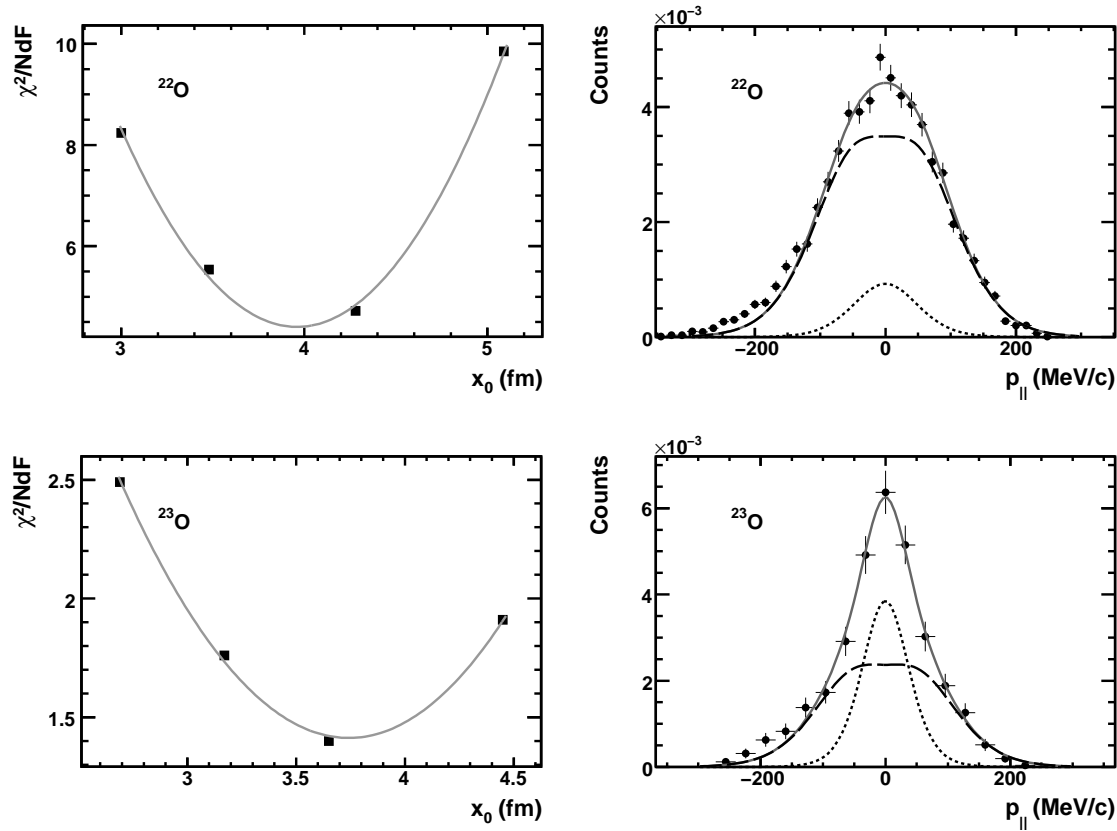


Figure 5.4: (Left) Correlation between χ^2/NdF and the cut-off parameter, x_0 , used to fit the experimental momentum distributions. (Right) The solid line represents the fit of the inclusive momentum distribution measured for the fragment in $^{22-23}\text{O}$ one-neutron knockout. The dotted and dashed lines correspond to the calculated $l = 0$ and $l = 2$ contributions, respectively.

At this point, it is important to note that the integral of each $\frac{dN_i}{dk_z}$ function, as well as the experimental distributions, had to be normalised to unity.

Calculations were done for several values of the cut-off parameter, x_0 , looking for the best χ^2 result. We assumed a parabolic behaviour to determine the position of the χ^2 minimum and we made the first derivative, $\frac{\partial\chi^2}{\partial x_0}$, equal to zero. Then, we used the second derivative to estimate the error of the x_0 value [Bev92]:

$$\sigma_{x_0} = \sqrt{2 \left(\frac{\partial^2 \chi^2}{\partial x_0^2} \right)^{-1}} \quad (5.11)$$

The errors associated with W_{gs} and W_{exc} were derived from the previous σ_{x_0} and the fit to the experimental data.

In order to validate the outlined procedure, ^{22}O and ^{23}O projectiles were analysed first. ^{22}O is known to exhibit a dominant $l = 2$ component, while a significant

Projectile	x_0 (fm)	I^π	E (keV)	S_n (keV)	l	Weight
^{22}O (0^+)	3.96 ± 0.08	$5/2^+$	0	6850	2	0.86 ± 0.04
		$1/2^+$	1218	8068	0	0.12 ± 0.04
^{23}O ($1/2^+$)	3.74 ± 0.27	0^+	0	2740	0	0.38 ± 0.07
		2^+	3199	5939	2	0.60 ± 0.07

Table 5.1: Calculated $core(I^\pi, E) \otimes neutron(l)$ contributions in the $^{22-23}\text{O}$ ground state. The cut-off parameter, x_0 , and the neutron-separation energy, S_n , that were used in the calculations are also shown.

$l = 0$ contribution emerges for ^{23}O [Fer03, Sau00]. In the case of ^{23}O , we took the one-neutron knockout experiment carried out by Cortina and collaborators at GSI [Cor04, Fer03] as our reference. The authors used a γ -ray detector to obtain spectroscopic information and determine the branching ratio to each state of the ^{22}O core. They found that 59 % of the events directly fed the core ground state and were associated with $l = 0$ neutrons. The remaining 41 % was shared with similar probabilities among three excitation levels at 3200, 4500 and 5800 keV and mainly corresponded to $l = 2$ contributions.

Fig. 5.4 and Table 5.1 summarise the results of our work. Fig. 5.4 (left) shows the χ^2 value as a function of the cut-off parameter, x_0 . The election of x_0 was optimised by requiring a minimum χ^2 . In Fig. 5.4 (right) and Table 5.1, we can see a major $l = 2$ contribution for ^{22}O projectiles, which accounts for 86 ± 4 % of the events and corresponds to a $^{21}\text{O}(5/2^+, \text{g.s.}) \otimes d_{5/2}$ configuration. In turn, ^{23}O shows a noticeable enhancement of the $l = 0$ component, observed with a probability of 38 ± 7 % and also associated with the ground state of the core fragment, $^{22}\text{O}(0^+, \text{g.s.}) \otimes s_{1/2}$. These calculations reproduce the expected trend when crossing $N = 14$ and were interpreted as a reasonable guarantee for the subsequent work on Ne nuclei.

Figs. 5.5–5.6 and Table 5.2 display the results concerning $^{24-28}\text{Ne}$ isotopes. The general trend of $^{24-26}\text{Ne}$ reflects the change from $l = 2$ to $l = 0$ configurations at $N = 14$ and is in good agreement with predictions based on the traditional shell model. This effect was already observed for ^{23}O and occurs for ^{22}N and ^{24}F as well, see Section 5.2. It is responsible for the FWHM reduction pointed out in Section 5.3.

In the case of $^{27,28}\text{Ne}$, we expected an enhancement of the $l = 2$ components related to the crossing of $N = 16$. However, the ground-state of these nuclei is dominated by $s_{1/2}$ neutrons coupled to excited states of the core. In particular, a $l = 0$ character is observed in the valence neutron for ^{27}Ne and ^{28}Ne with probabilities of 64 ± 12 and 81 ± 9 %, respectively.

It is especially interesting to compare our results for $^{26,28}\text{Ne}$ with the earlier one-

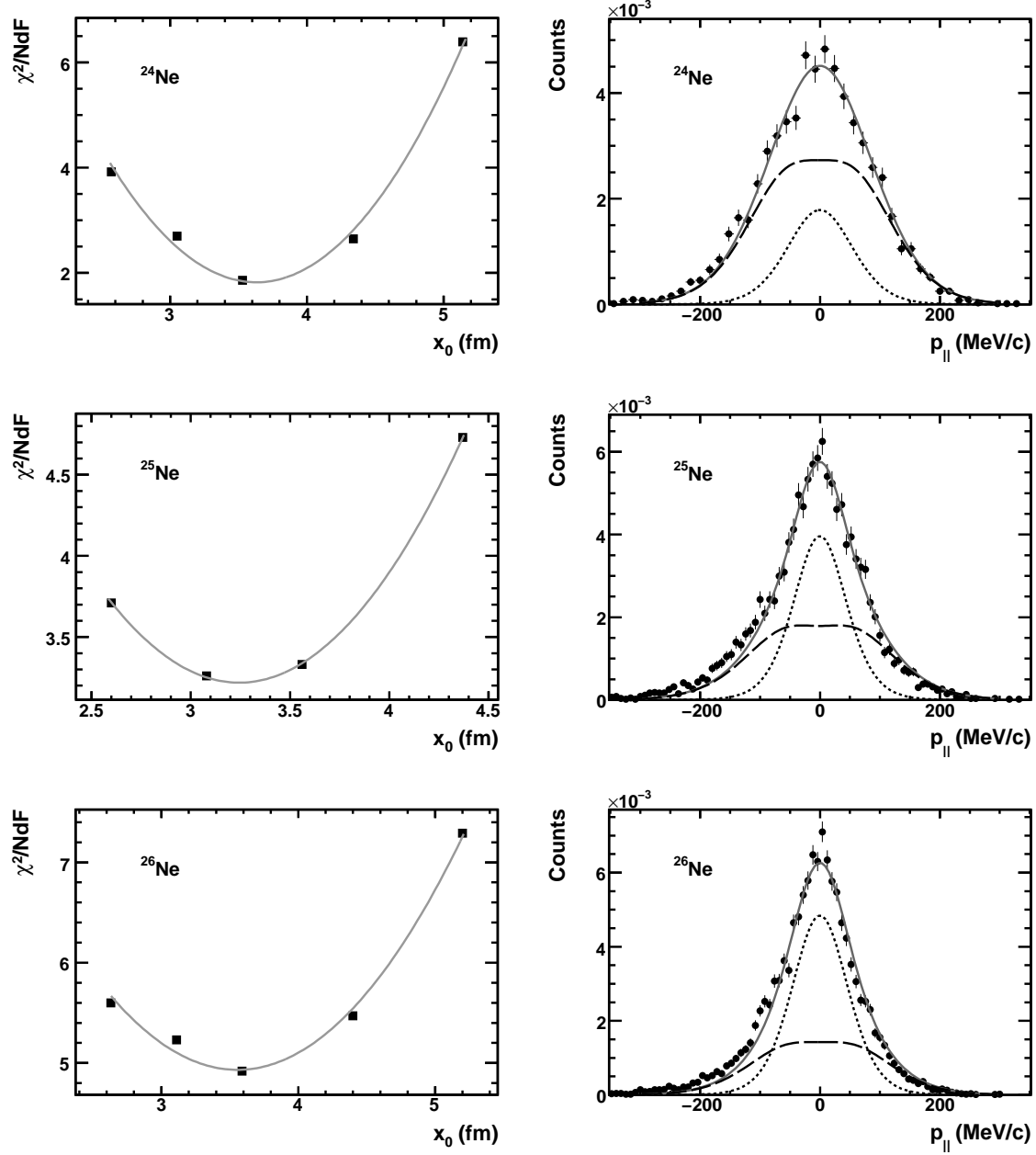


Figure 5.5: (Left) Correlation between χ^2/NdF and the cut-off parameter, x_0 , used to fit the experimental momentum distributions. (Right) The solid line represents the fit of the fragment momentum distributions measured in the one-neutron knockout of $^{24-26}\text{Ne}$. The dotted and dashed lines correspond to the calculated $l=0$ and $l=2$ contributions, respectively.

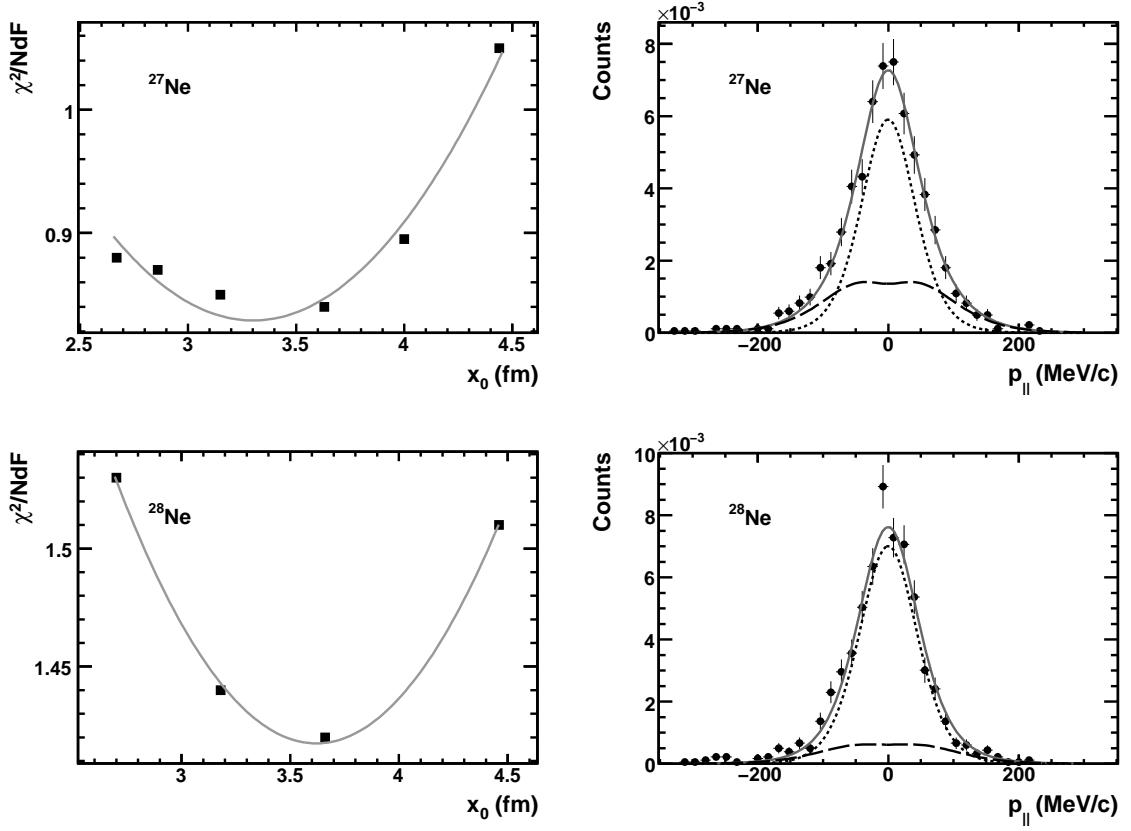


Figure 5.6: (Left) Correlation between χ^2/NdF and the cut-off parameter, x_0 , used to fit the experimental momentum distributions. (Right) The solid line represents the fit of the fragment momentum distributions measured in the one-neutron knockout of $^{27-28}\text{Ne}$. The dotted and dashed lines correspond to the calculated $l = 0$ and $l = 2$ contributions, respectively.

Projectile	x_0 (fm)	I^π	E (keV)	S_n (keV)	l	Weight
^{24}Ne (0^+)	3.63 ± 0.12	$5/2^+$	0	8869	2	0.74 ± 0.05
		$1/2^+$	1017	9886	0	0.25 ± 0.05
^{25}Ne ($1/2^+$)	3.24 ± 0.11	0^+	0	4180	0	0.46 ± 0.03
		2^+	1982	6162	2	0.51 ± 0.03
^{26}Ne (0^+)	3.55 ± 0.13	$1/2^+$	0	5580	0	0.59 ± 0.03
		$5/2^+$	1703	7283	2	0.38 ± 0.03
^{27}Ne ($3/2^+$)	3.30 ± 0.47	0^+	0	1410	2	0.34 ± 0.11
		2^+	2024	3434	0	0.64 ± 0.12
^{28}Ne (0^+)	3.61 ± 0.50	$3/2^+$	0	3900	2	0.16 ± 0.08
		$1/2^+$	885	4785	0	0.81 ± 0.09

Table 5.2: Calculated $core(I^\pi, E) \otimes neutron(l)$ contributions in the $^{24-28}\text{Ne}$ ground state. The cut-off parameter, x_0 , and the neutron-separation energy, S_n , that were used in the calculations are also shown.

neutron knockout experiment carried out by Terry *et al.* at NSCL [Ter06], who based their conclusions on spectroscopic measurements performed with a segmented Ge array for γ detection, SeGA [Mue01]. They attained an accurate description of the projectiles, which accounted for the role of different excited fragment states. Although the description provided in this dissertation is a more simplified picture, we arrived at very similar conclusions. In ^{26}Ne and ^{28}Ne one-neutron knockout, we obtained probabilities of 59 ± 3 and 16 ± 8 %, respectively, associated with the feeding of the core ground state. These values are reasonably close to the 43 and 32 % for ^{26}Ne and ^{28}Ne reported by Ref. [Ter06].

Conclusions

The intent of the work described in this dissertation was to explore the single-particle properties of neutron-rich projectiles, described as a sum of different *core* \otimes *neutron* configurations. Thirty-nine nuclei, ranging from C to Al and with neutron numbers from $N = 8$ to 22, were experimentally studied by means of the one-neutron knockout technique.

The experiment was performed at *Gesellschaft für Schwerionenforschung* [GSI], in Darmstadt, Germany, where we made use of the FRS magnetic spectrometer [Gei92]. Exotic neutron-rich projectiles were obtained by fragmentation of a ^{40}Ar primary beam accelerated to 700 MeV/nucleon. The one-neutron knockout reaction took place in a 1720 mg/cm^2 Be target surrounded by the MINIBALL array of segmented Ge detectors [Ebe01]. In this manner, it was possible to measure the emitted γ rays and identify the excited states of the $A - 1$ fragments.

Two inclusive observables: the longitudinal-momentum distribution of the $A - 1$ fragments and the one-neutron knockout cross-section, were determined for the different projectiles, namely, $^{14-19}\text{C}$, $^{16-22}\text{N}$, $^{19-23}\text{O}$, $^{21-26}\text{F}$, $^{24-28}\text{Ne}$, $^{27-31}\text{Na}$, $^{31-33}\text{Mg}$ and $^{34-35}\text{Al}$.

The fragment momentum distributions are especially appropriate for the study of halo structures, since, according to the Heisenberg uncertainty principle, the spatial de-localization would result in very small widths. The shape and width of these distributions are also sensitive to the orbital angular momentum of the neutron removed in the reaction and inform about its wave function. We performed a detailed analysis of the FWHM values, which can be used to outline the l character of the valence neutron and roughly distinguish between $l = 0$ and 2 contributions in the *sd* region. In general terms, our results agree with the one-neutron knockout data currently available in the literature. However, the transmission of the fragments produced in ^{14}C and ^{16}N one-neutron knockout was seriously affected by the acceptance limits of the FRS and it was not possible to extract the associated FWHM.

The inclusive cross-sections of the one-neutron knockout process were evaluated to obtain complementary information. Among the different corrections applied to these experimental data, it was important to account for reactions that did not occur

in the target, but in the materials surrounding it. Such a task required dedicated sets of measurements and could only be performed for a certain number of cases: $^{16-17}\text{C}$, $^{18-20}\text{N}$, $^{20-22}\text{O}$, $^{23-25}\text{F}$, $^{26-27}\text{Ne}$, $^{29-30}\text{Na}$ and $^{31-32}\text{Mg}$.

The interpretation of the inclusive results was restricted to certain isotopic chains: $^{14-19}\text{C}$, $^{16-22}\text{N}$, $^{19-23}\text{O}$, $^{21-26}\text{F}$ and $^{24-28}\text{Ne}$, and organised around specific topics.

The appearance of one-neutron halo configurations was discussed for odd-mass carbon isotopes, that is to say, $^{15,17,19}\text{C}$. In the case of ^{15}C , our results could indicate an extended spatial distribution of the valence neutron. Although similar conclusions were obtained in previous experiments, contradictory measurements of the total-interaction cross-section leave room for doubt about the structure of this nucleus. The description of ^{17}C was completed with exclusive measurements. It exhibits a clear halo suppression caused by the predominance of a $^{16}\text{C}(2^+) \otimes 0d_{5/2}$ component in the ground state. Additionally, we were able to observe the well-known one-neutron halo of ^{19}C .

In accordance with traditional shell model predictions, our results for N, O and F reflect the change from $0d_{5/2}$ to $1s_{1/2}$ configurations when crossing $N = 14$. This work also provides the first one-neutron knockout data for ^{22}N . Though it was insufficient to draw conclusions about a possible extended nature of the valence-neutron density distribution [Oza00, Soh08], we can assert a significant $1s_{1/2}$ admixture in the ground state. Concerning ^{26}F , no clear effects were observed in relation to the crossing of $N = 16$ and the expected population of the $0d_{3/2}$ neutron level. As Fernández *et al.* suggested [Fer03], these results might indicate a different configuration, based on a $1s_{1/2}$ valence neutron coupled to an excited state of the ^{25}F core.

As occurs with N, O and F, Ne isotopes also exhibit significant $1s_{1/2}$ admixtures when crossing $N = 14$. However, $^{27,28}\text{Ne}$, with $N = 17$ and 18 , do not behave as expected. The valence neutron occupies a $1s_{1/2}$ level rather than $0d_{3/2}$ and is coupled to an excited state of the core. To study the structure of $^{24-28}\text{Ne}$ projectiles more fully, we analysed the measured momentum distributions on the basis of a simple theoretical model. Our calculations included the orbital angular momentum of the removed neutron, its separation energy and a lower cut-off parameter that ensured the core survival. We assumed a simplified picture of the projectile that accounted for only two possible *core* \otimes *neutron* configurations. The conclusions derived from this description are in good agreement with the exclusive results obtained by Terry *et al.* [Ter06] for $^{26,28}\text{Ne}$ one-neutron knockout.

Exclusive measurements were also carried out. The accumulated statistics allowed us to study the γ rays emitted in the one-neutron knockout of $^{15-17}\text{C}$, $^{17-20}\text{N}$, $^{20-22}\text{O}$ and $^{22-25}\text{F}$. In the case of ^{24}F , $^{20,22}\text{O}$ and $^{15,16}\text{C}$, we did not observe any proof

of fragment de-excitation, which probably means that reactions feeding its ground state prevailed in the process. Unfortunately, the moderate resolution of the spectra hindered a detailed analysis of complex situations where numerous γ rays were produced. Therefore, we concentrated on four feasible cases, ^{17}C , ^{19}N , ^{21}O and ^{25}F .

The γ rays measured in ^{17}C one-neutron knockout suggest the population of the first excited ^{16}C state at 1766 keV and a group of three levels around 4000 keV. The exclusive data support the previous work of Maddalena *et al.* [Mad01], who found a significant probability of feeding the ground state of the core, in apparent contradiction with theoretical calculations. We arrived at similar results that confirm their conclusions.

Concerning ^{19}N one-neutron knockout, three low-energy levels of the core were populated in the reaction, at 115, 588 and 747 keV. In light of the γ coincidences observed, we proposed a decay scheme for ^{18}N that is in good agreement with the recent work of Wiedeking *et al.* [Wie08]. Even though it was not possible to determine the associated branching ratios and cross-sections, we were able to set upper and lower limits for the population of the ^{18}N states at 588 and 747 keV.

In ^{21}O one-neutron knockout, the first two excited levels of the core, at 1674 and 3570 keV, were populated. The calculated branching ratios and partial cross-sections show significant differences with respect to previous data obtained by Fernández *et al.* [Fer03]. The low resolution of measurements carried out at that time could explain the discrepancies.

Measurements carried out for ^{25}F projectiles show that the first excitation level of ^{24}F , at 522 keV, was populated. We calculated the associated branching ratio and partial cross-section.

By and large, this work contributes to a better understanding of the neutron-rich region in the nuclear landscape. Our data can be combined with previous experiments, which mainly studied species up to F, to obtain a more solid picture of the ground-state structure for numerous isotopes. Also, the measurements we performed for higher proton numbers, up to Al, constitute a valuable source of information in a domain that is still relatively unexplored.

Appendix A

Optics of charged particles

This appendix describes the use of magnetic fields to bend and direct the paths of a bunch of charged particles. We will explain here those concepts and relations required to understand the working mode of the Fragment Separator in this experiment. A complete review of the optics of charged particles can be found in Ref. [Car87].

A.1 The phase space

A beam of particles may be represented at any instant of time by a collection of points in a six-dimensional space, known as phase space, where a single particle has three coordinates specifying its position and three specifying its momentum. The coordinates are defined in terms of a certain point in the phase space known as the reference particle. The path of the reference particle through the magnetic system is called the reference trajectory and its momentum is the reference momentum.

The three coordinates that specify the position of a particle, labelled s , x and y , are displayed in Fig. A.1. The first represents the distance along the reference trajectory and is the independent variable in charged-particle optics. At any point on the reference trajectory, we can define a longitudinal axis in the direction of the reference momentum. The two transverse coordinates, x and y , are perpendicular to this axis and correspond to the horizontal and vertical directions, respectively.

The momentum coordinates are defined as two direction tangents, a and b , and the fractional momentum deviation, δ_p . The equations below specify these definitions,

$$a = \frac{dx}{ds}, \quad b = \frac{dy}{ds} \tag{A.1}$$

$$\delta_p = \frac{p - p_0}{p_0} \tag{A.2}$$

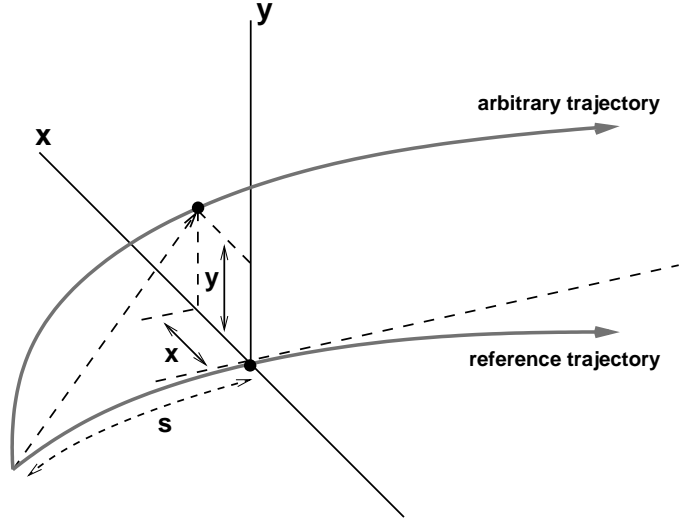


Figure A.1: Coordinate system used in the optics of charge particles.

where p_0 is the reference momentum and p the momentum of the charged particle.

A.2 The transfer matrix

The action of a magnetic system can be described by what are known as transfer matrices. In this representation, the vector that specifies the initial situation of an ion can be transformed by multiplying it by the transfer matrix, T , to obtain a new vector that describes the situation of the ion after passing through the system.

$$\begin{pmatrix} x \\ a \\ y \\ b \\ s \\ \delta_p \end{pmatrix} = T \begin{pmatrix} x_0 \\ a_0 \\ y_0 \\ b_0 \\ s_0 \\ \delta_{p0} \end{pmatrix} \quad (\text{A.3})$$

In the case of mid-plane symmetry where the bend plane is horizontal, the transfer matrix is expressed as follows:

$$T = \begin{pmatrix} t_{11} & t_{12} & 0 & 0 & 0 & t_{16} \\ t_{21} & t_{22} & 0 & 0 & 0 & t_{26} \\ 0 & 0 & t_{33} & t_{34} & 0 & 0 \\ 0 & 0 & t_{43} & t_{44} & 0 & 0 \\ t_{51} & t_{52} & 0 & 0 & 1 & t_{56} \\ 0 & 0 & 0 & 0 & 0 & 1 \end{pmatrix} \quad (\text{A.4})$$

Hence, both horizontal and vertical motion are completely independent. The

elements t_{ij} represent the first-order solutions of the motion equation for the charged particle.

$$\begin{aligned}
t_{11} &= (x|x) = \frac{\partial x}{\partial x_0}, & t_{12} &= (x|a) = \frac{\partial x}{\partial a_0}, & t_{16} &= (x|\delta) = \frac{\partial x}{\partial \delta_{p0}} \\
t_{21} &= (a|x) = \frac{\partial a}{\partial x_0}, & t_{22} &= (a|a) = \frac{\partial a}{\partial a_0}, & t_{26} &= (a|\delta) = \frac{\partial a}{\partial \delta_{p0}}, \\
t_{33} &= (y|y) = \frac{\partial y}{\partial y_0}, & t_{34} &= (y|b) = \frac{\partial y}{\partial b_0} \\
t_{43} &= (b|y) = \frac{\partial b}{\partial y_0}, & t_{44} &= (y|b) = \frac{\partial b}{\partial b_0} \\
t_{51} &= (s|x) = \frac{\partial s}{\partial x_0}, & t_{52} &= (s|a) = \frac{\partial s}{\partial a_0}, & t_{56} &= (s|\delta) = \frac{\partial s}{\partial \delta_{p0}}
\end{aligned}$$

The element $t_{11} = (x|x)$ is usually called magnification, M , and reflects the dependence between the final and the initial x positions. Another important element for our studies is $t_{16} = (x|\delta)$, usually known as dispersion, D . It expresses the change in the x position induced by a difference in the fractional momentum deviation.

A.3 Measuring the longitudinal momentum

We consider the Fragment Separator to be divided in two different stages, F0–F2 and F2–F4, as illustrated in Fig. A.2. These stages are described by the transfer matrices A and B according to Eqs. A.5 and A.6.

$$\begin{pmatrix} x_{F2} \\ a_{F2} \\ y_{F2} \\ b_{F2} \\ s_{F2} \\ \delta_{F2} \end{pmatrix} = A \begin{pmatrix} x_{F0} \\ a_{F0} \\ y_{F0} \\ b_{F0} \\ s_{F0} \\ \delta_{F0} \end{pmatrix} \quad (\text{A.5})$$

$$\begin{pmatrix} x_{F4} \\ a_{F4} \\ y_{F4} \\ b_{F4} \\ s_{F4} \\ \delta_{F4} \end{pmatrix} = B \begin{pmatrix} x_{F2} \\ a_{F2} \\ y_{F2} \\ b_{F2} \\ s_{F2} \\ \delta_{F2} \end{pmatrix} \quad (\text{A.6})$$

The x positions at the focal planes F2 and F4 can be deduced from the previous equations.

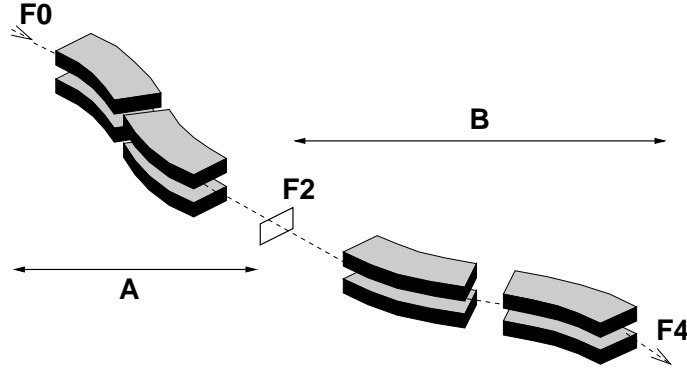


Figure A.2: Schematic drawing of the FRS magnetic spectrometer. It is divided in two stages that correspond to the regions between the initial and intermediate focal planes, F0–F2, and between the intermediate and final focal planes, F2–F4.

$$x_{F2} = (x|x)_A x_{F0} + (x|a)_A a_{F0} + (x|\delta)_A \delta_{F0} \quad (\text{A.7})$$

$$x_{F4} = (x|x)_B x_{F2} + (x|a)_B a_{F2} + (x|\delta)_B \delta_{F2} \quad (\text{A.8})$$

For a system with point-to-point imaging, the position at the focal plane does not depend on the angle, so the coefficients $(x|a)_A$ and $(x|a)_B$ must be zero. Moreover, we can neglect x_{F0} for a well-focused beam centred at the entrance of the FRS. Under these assumptions, the above expressions are transformed as follows:

$$x_{F2} = (x|\delta)_A \delta_{F0} \quad (\text{A.9})$$

$$x_{F4} = (x|x)_B x_{F2} + (x|\delta)_B \delta_{F2} \quad (\text{A.10})$$

By replacing x_{F2} in Eq. A.10, we obtain:

$$x_{F4} = (x|x)_B (x|\delta)_A \delta_{F0} + (x|\delta)_B \delta_{F2} \quad (\text{A.11})$$

This can be taken a step further, since Eq. A.12 must be fulfilled in the energy-loss mode.

$$(x|x)_B (x|\delta)_A = -(x|\delta)_B \quad (\text{A.12})$$

In this way, when the momentum deviation does not change in the mid-plane, i.e., $\delta_{F0} = \delta_{F2}$, we ensure that the entire system is achromatic and that the position at the final focal plane does not depend on the momentum of the particle.

Then, by modifying Eq. A.11 according to the condition A.12, we arrive at:

$$x_{F4} = -(x|\delta_p)_B \delta_{pF0} + (x|\delta_p)_A \delta_{pF2} \quad (\text{A.13})$$

$$= -(x|\delta_p)_B \frac{p_{F0} - p_A}{p_A} + (x|\delta_p)_B \frac{p_{F2} - p_B}{p_B} \quad (\text{A.14})$$

$$= -(x|\delta_p)_B \frac{p_{F0}}{p_A} + (x|\delta_p)_B \frac{p_{F2}}{p_B} \quad (\text{A.15})$$

By solving Eq. A.15 for the momentum of the particle at the second stage of the spectrometer, p_{F2} , we obtain:

$$p_{F2} = \frac{x_{F4}}{(x|\delta)_B} p_B + \frac{p_{F0}}{p_A} p_B \quad (\text{A.16})$$

Now, we can deduce p_{F0} from the relation $x_{F2} = (x|\delta)_A \frac{p_{F0} - p_A}{p_A}$, see Eq. A.9.

$$p_{F0} = p_A \left(1 + \frac{x_{F2}}{(x|\delta)_A} \right) \quad (\text{A.17})$$

Which results in:

$$p_{F2} = p_B \left(1 + \frac{x_{F2}}{(x|\delta)_A} + \frac{x_{F4}}{(x|\delta)_B} \right) \quad (\text{A.18})$$

The reference momentum, p_B , is defined by the reference magnetic rigidity at the second stage of the spectrometer, χ_B , and by the charge of the particle, q_B .

$$p_B = \chi_B q_B \quad (\text{A.19})$$

This leads us to the final formula A.20, which was used to calculate the momentum of the knockout fragments in this experiment.

$$p_{F2} = q_B \chi_B \left(1 + \frac{x_{F2}}{(x|\delta)_A} + \frac{x_{F4}}{(x|\delta)_B} \right) \quad (\text{A.20})$$

We would like to remark that p_{F2} is the momentum in the reference frame of the laboratory, which must be converted into the rest frame of the projectile.

Appendix B

Inclusive longitudinal-momentum distributions

We measured the longitudinal-momentum distributions of the fragments produced in the one-neutron knockout of different projectiles, ranging from carbon isotopes to aluminium. The results are compiled in the figures of the following pages:

- **Figures B.1 and B.2**, $^{14-19}\text{C}$ projectiles.
- **Figures B.3, B.4 and B.5**, $^{16-22}\text{N}$ projectiles.
- **Figures B.6 and B.7**, $^{19-23}\text{O}$ projectiles.
- **Figures B.8 and B.9**, $^{21-26}\text{F}$ projectiles.
- **Figures B.10 and B.11**, $^{24-28}\text{Ne}$ projectiles.
- **Figures B.12 and B.13**, $^{27-31}\text{Na}$ projectiles.
- **Figure B.14**, $^{31-33}\text{Mg}$ projectiles.
- **Figure B.15**, $^{34-35}\text{Al}$ projectiles.

The plots on the left side were used to study acceptance cuts that could distort the results. We represented the longitudinal momentum, p_{\parallel} , as a function of the x direction tangent at the final focal plane, a_{F4} . The affected regions are marked with dashed lines and were excluded from the analysis.

The plots on the right side correspond to the momentum distributions in the projectile comoving frame, p_{\parallel} . The solid lines represent the Gaussian fits used to determine the FWHM values that appear on the top of the graphs. In the $^{15}\text{C} \rightarrow ^{14}\text{C}$ case, where the distribution is noticeably cut, a graphical evaluation of the FWHM was applied.

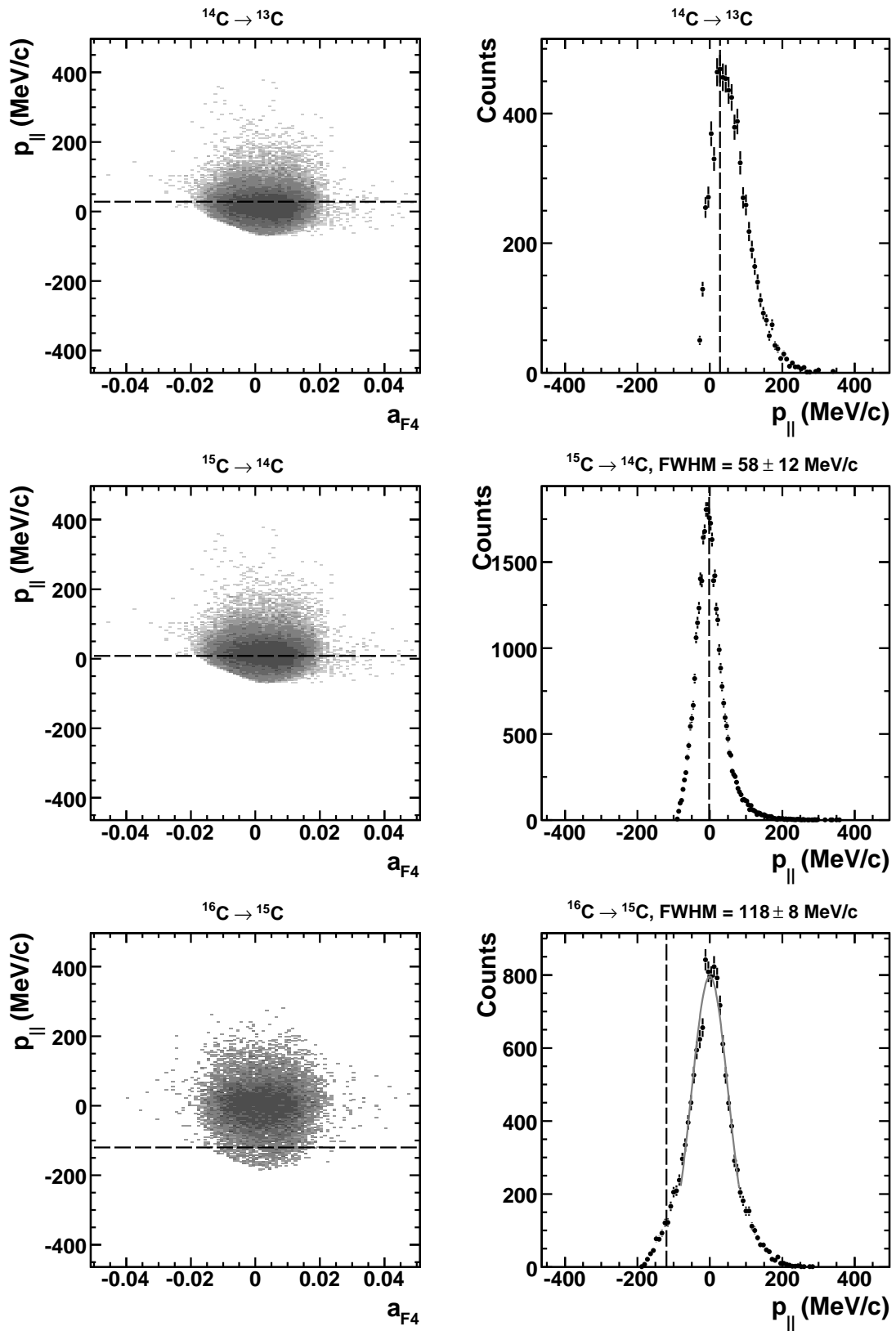


Figure B.1: Momentum distributions measured in $^{14-16}\text{C}$ one-neutron knockout.

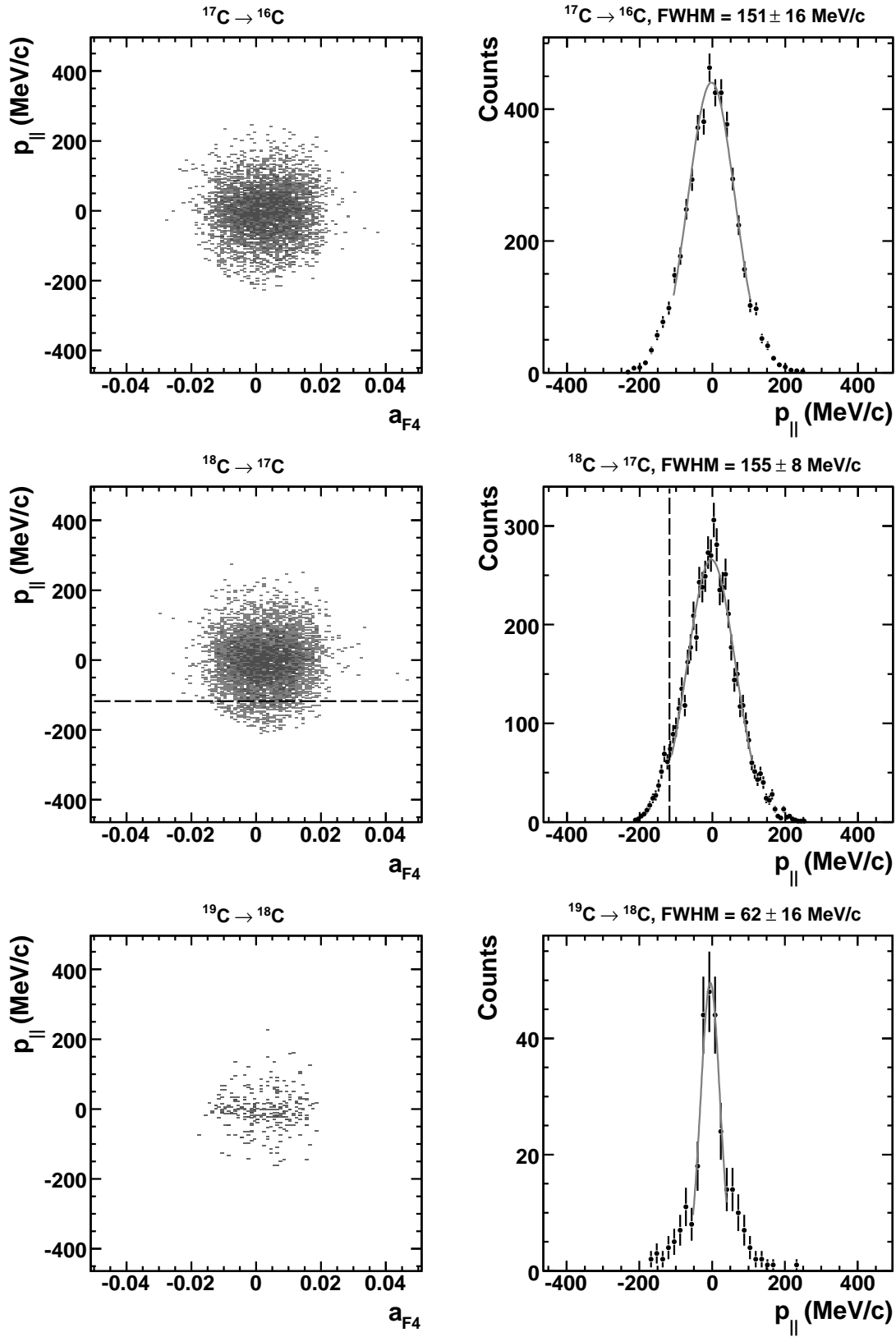


Figure B.2: Momentum distributions measured in $^{17-19}\text{C}$ one-neutron knockout.

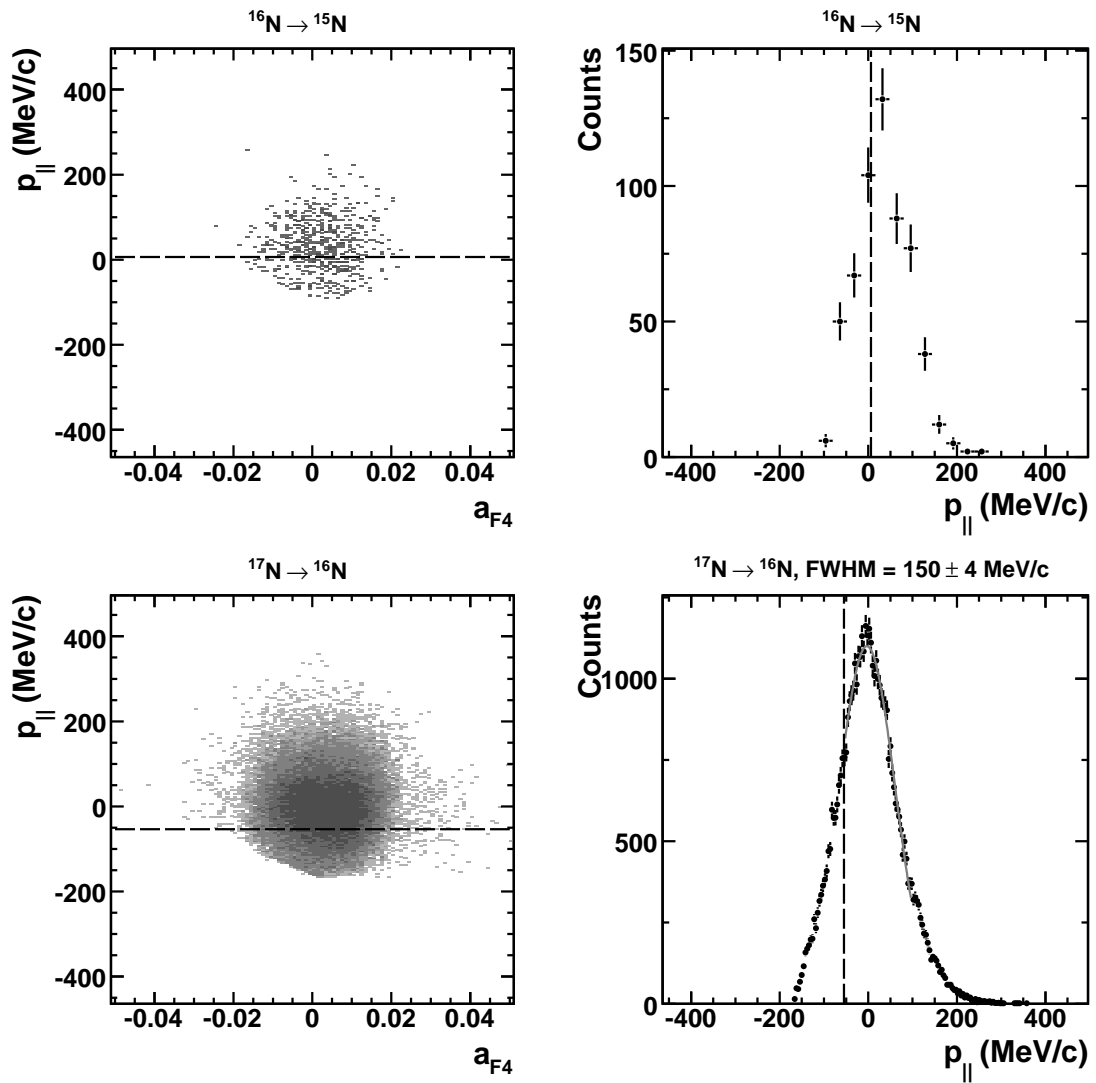


Figure B.3: Momentum distributions measured in $^{16-17}\text{N}$ one-neutron knockout.

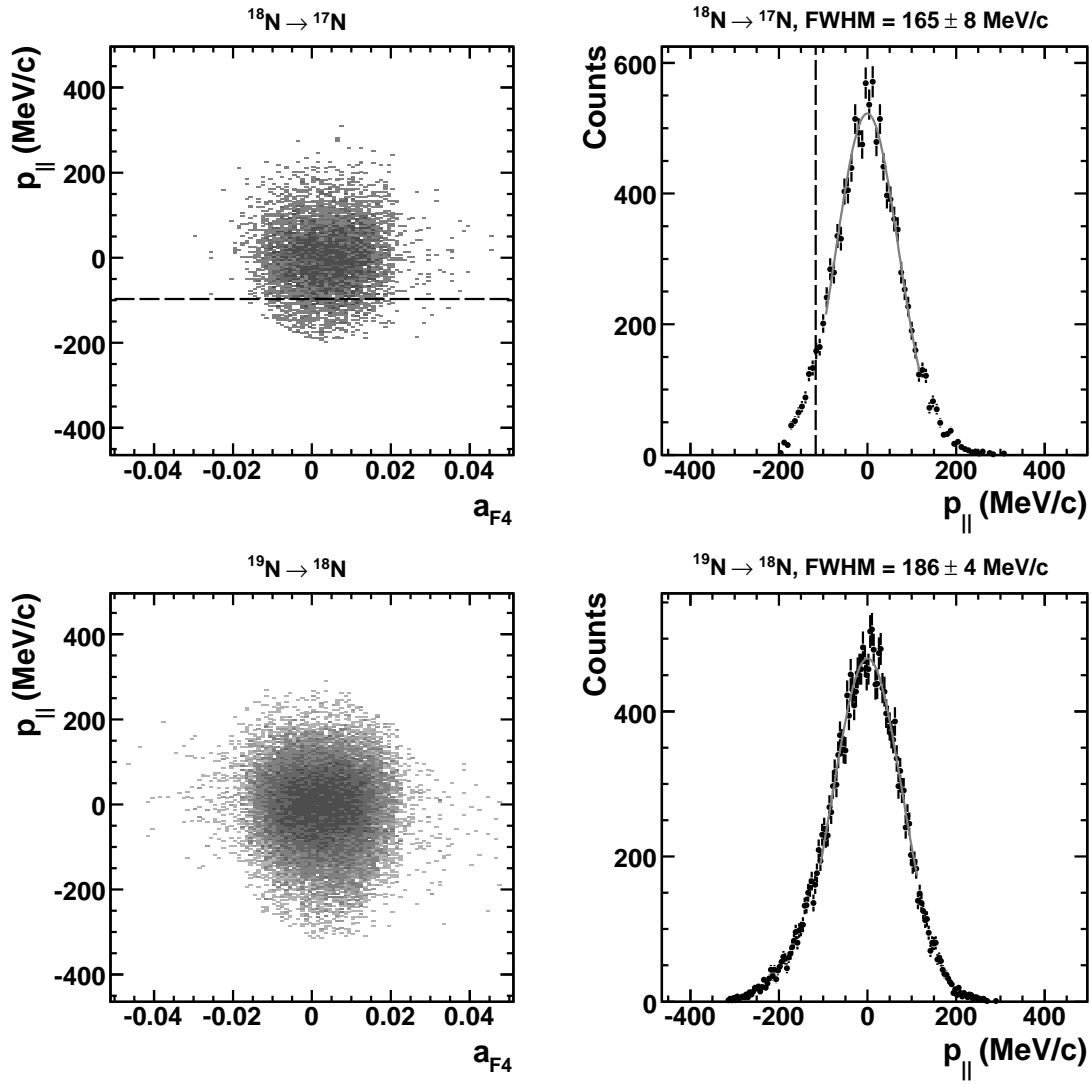


Figure B.4: Momentum distributions measured in $^{18-19}\text{N}$ one-neutron knockout.

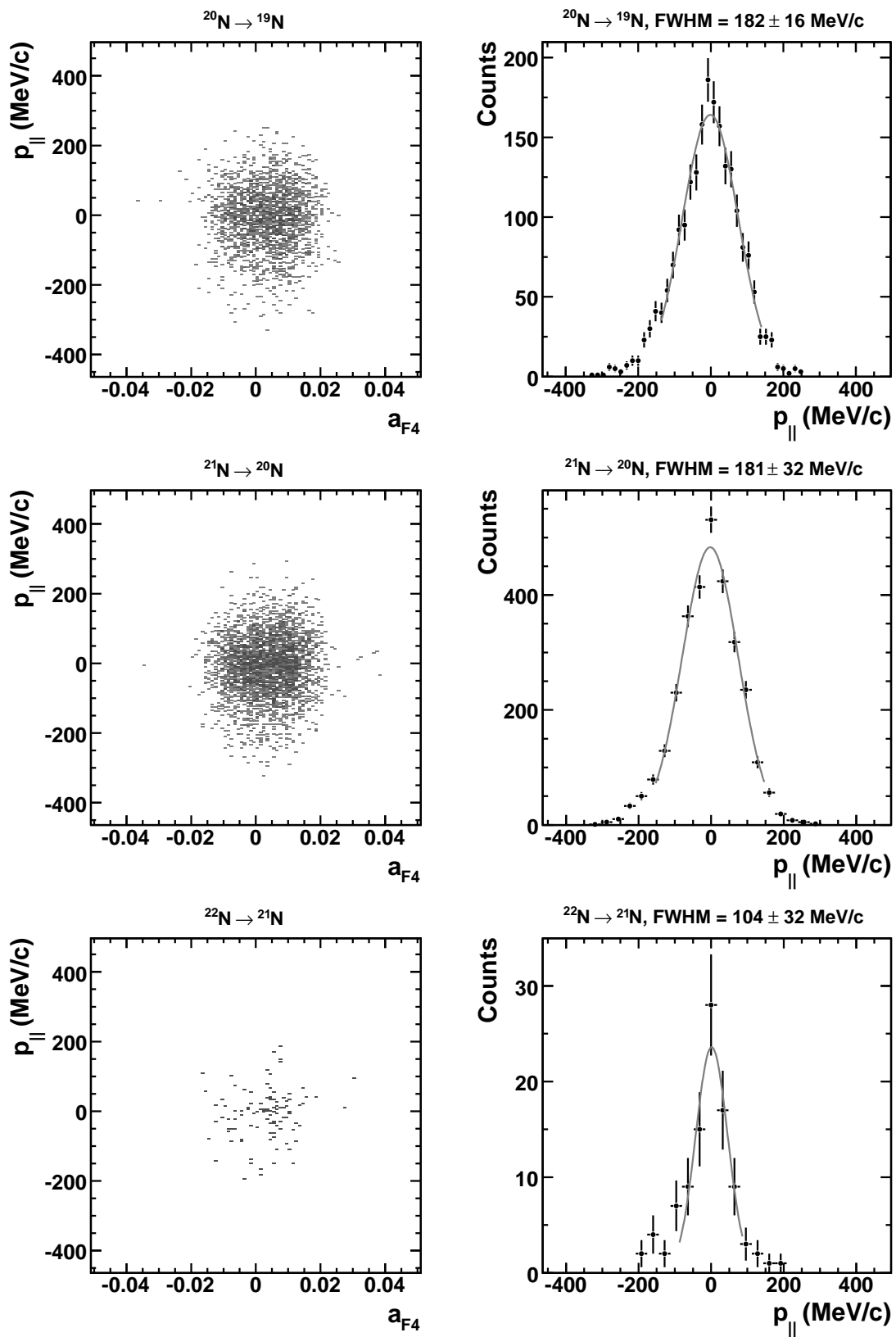


Figure B.5: Momentum distributions measured in $^{20-22}\text{N}$ one-neutron knockout.

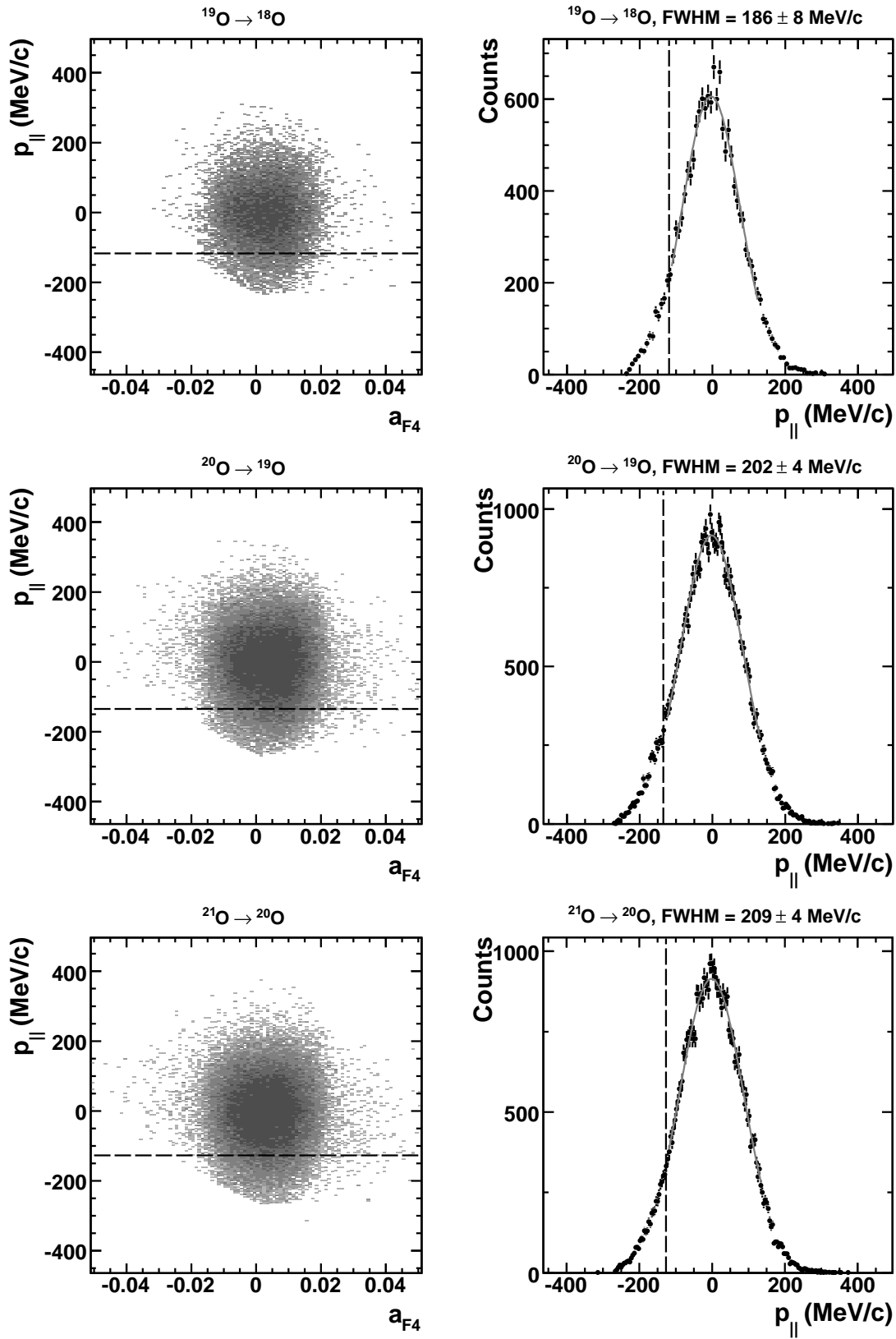


Figure B.6: Momentum distributions measured in $^{19-21}\text{O}$ one-neutron knockout.

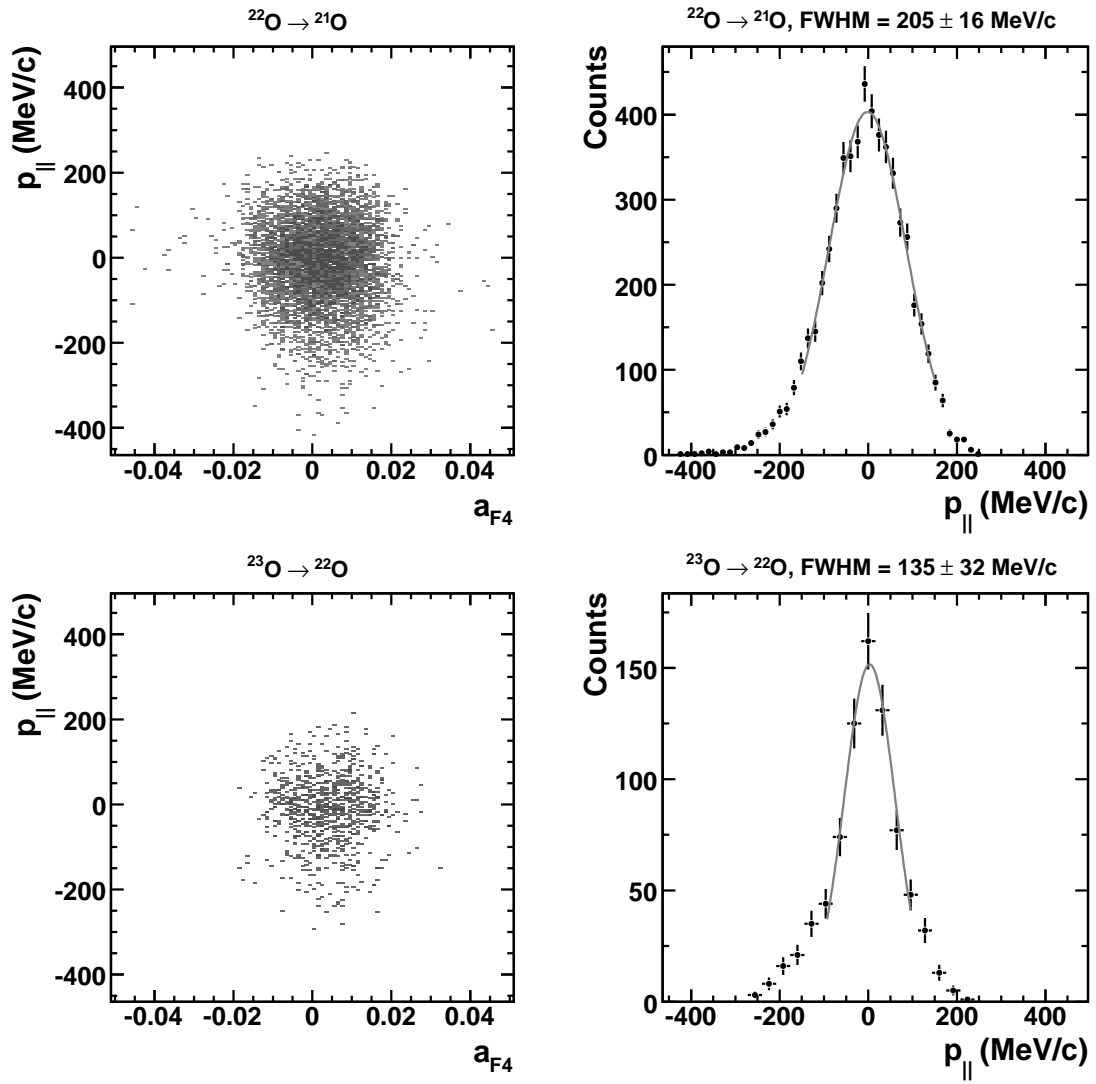


Figure B.7: Momentum distributions measured in $^{22-23}\text{O}$ one-neutron knockout.

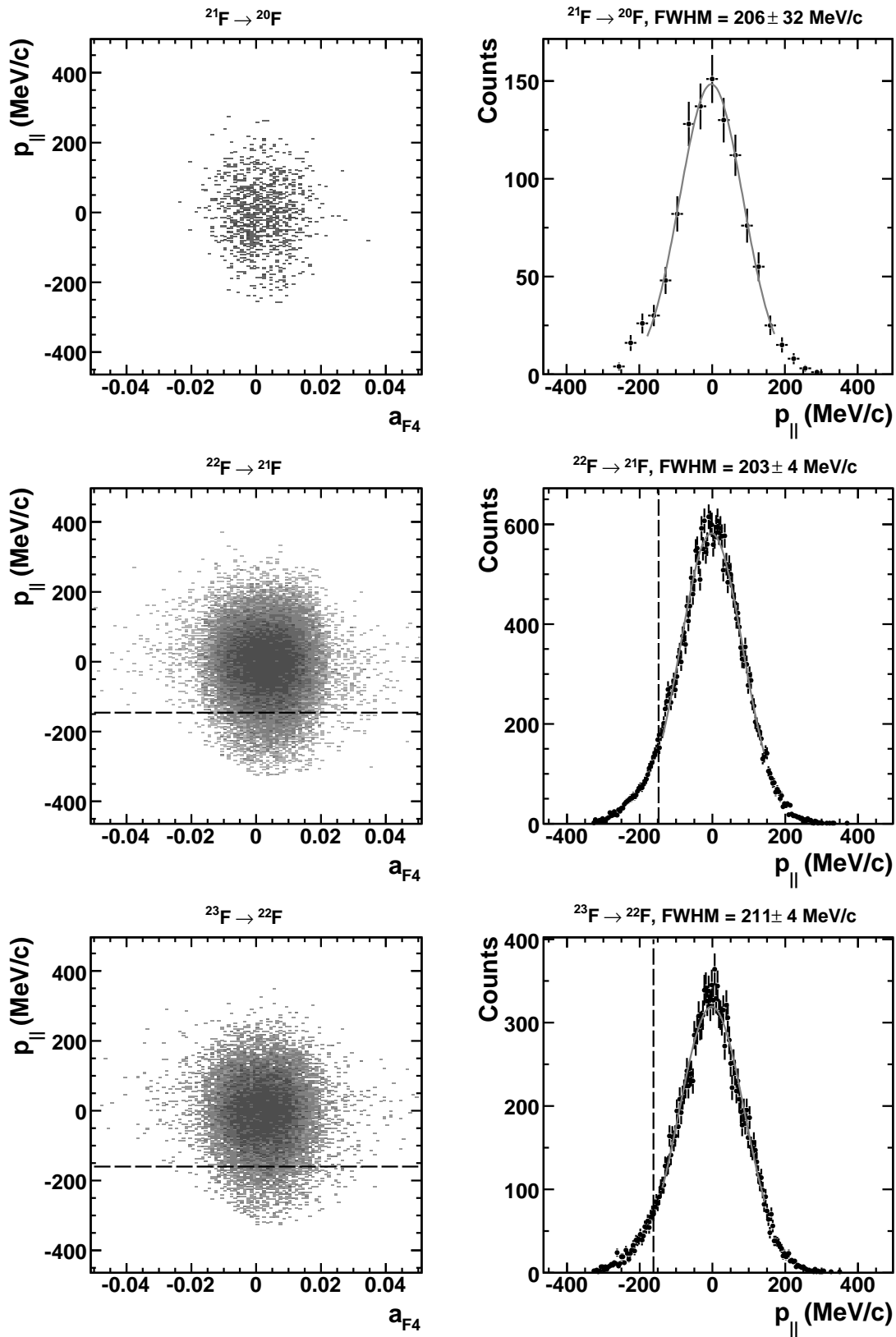


Figure B.8: Momentum distributions measured in $^{21-23}\text{F}$ one neutron knockout.

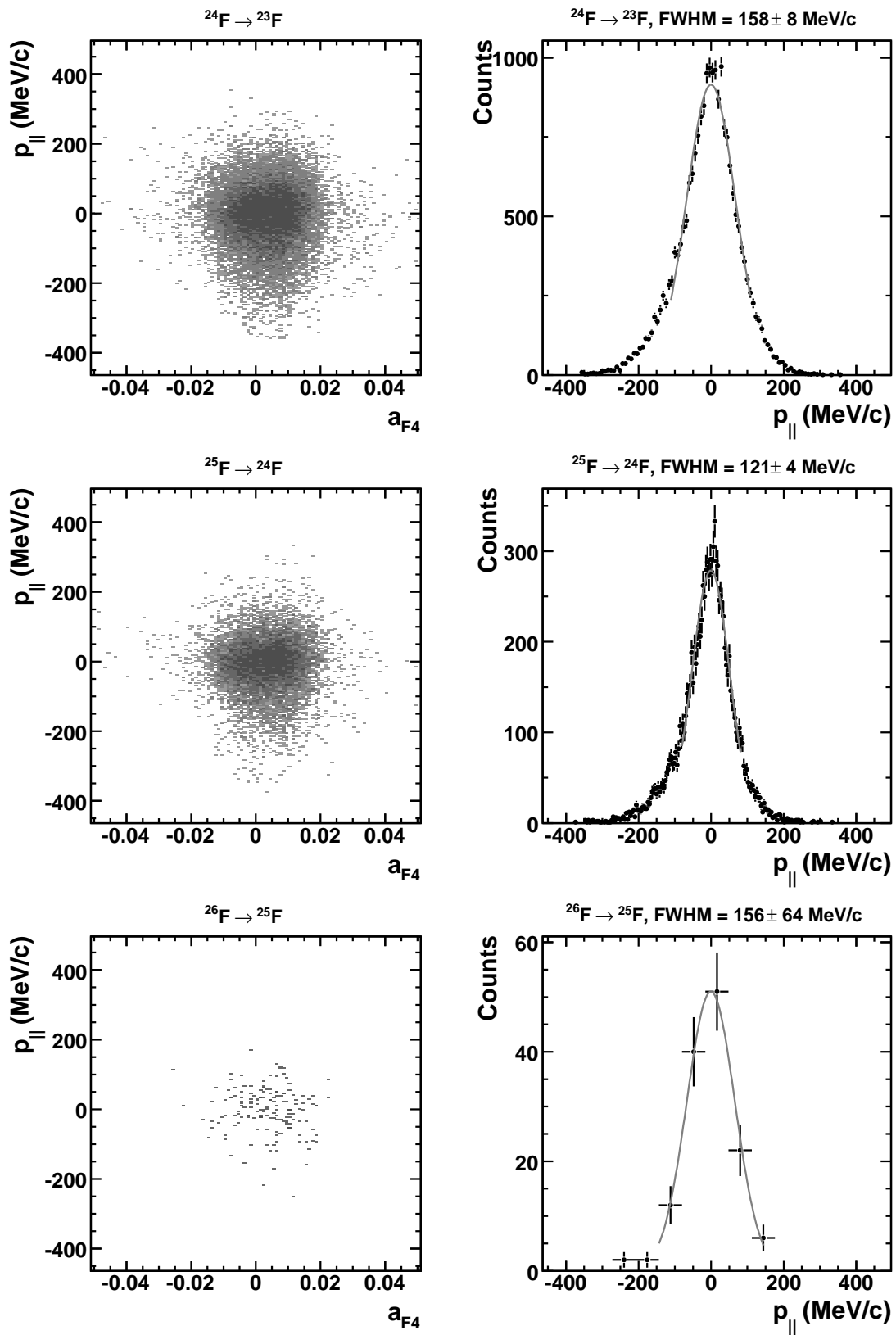


Figure B.9: Momentum distributions measured in $^{24-26}\text{F}$ one-neutron knockout.

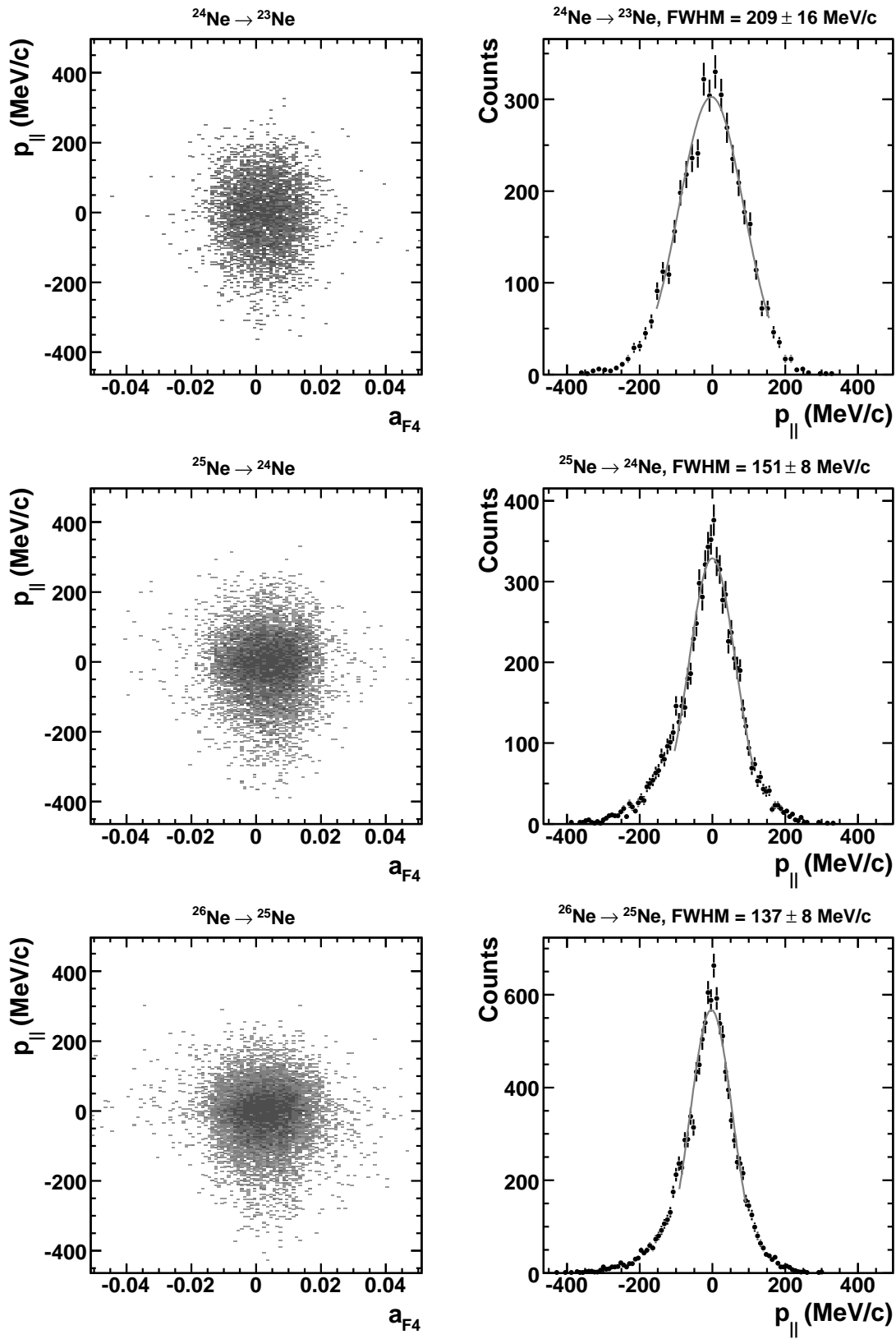


Figure B.10: Momentum distributions measured in $^{24-26}\text{Ne}$ one-neutron knockout.

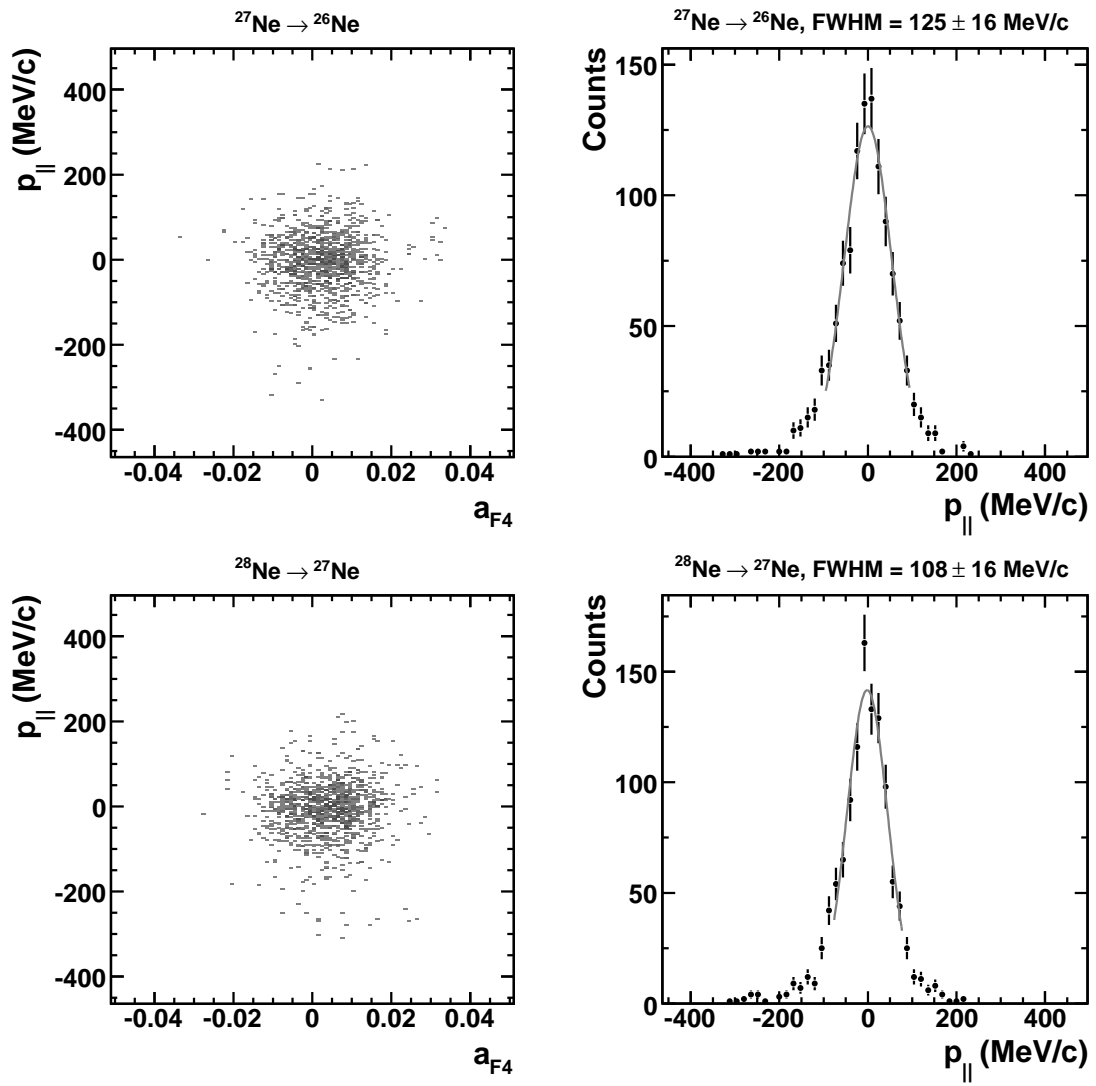


Figure B.11: Momentum distributions measured in $^{27-28}\text{Ne}$ one-neutron knockout.

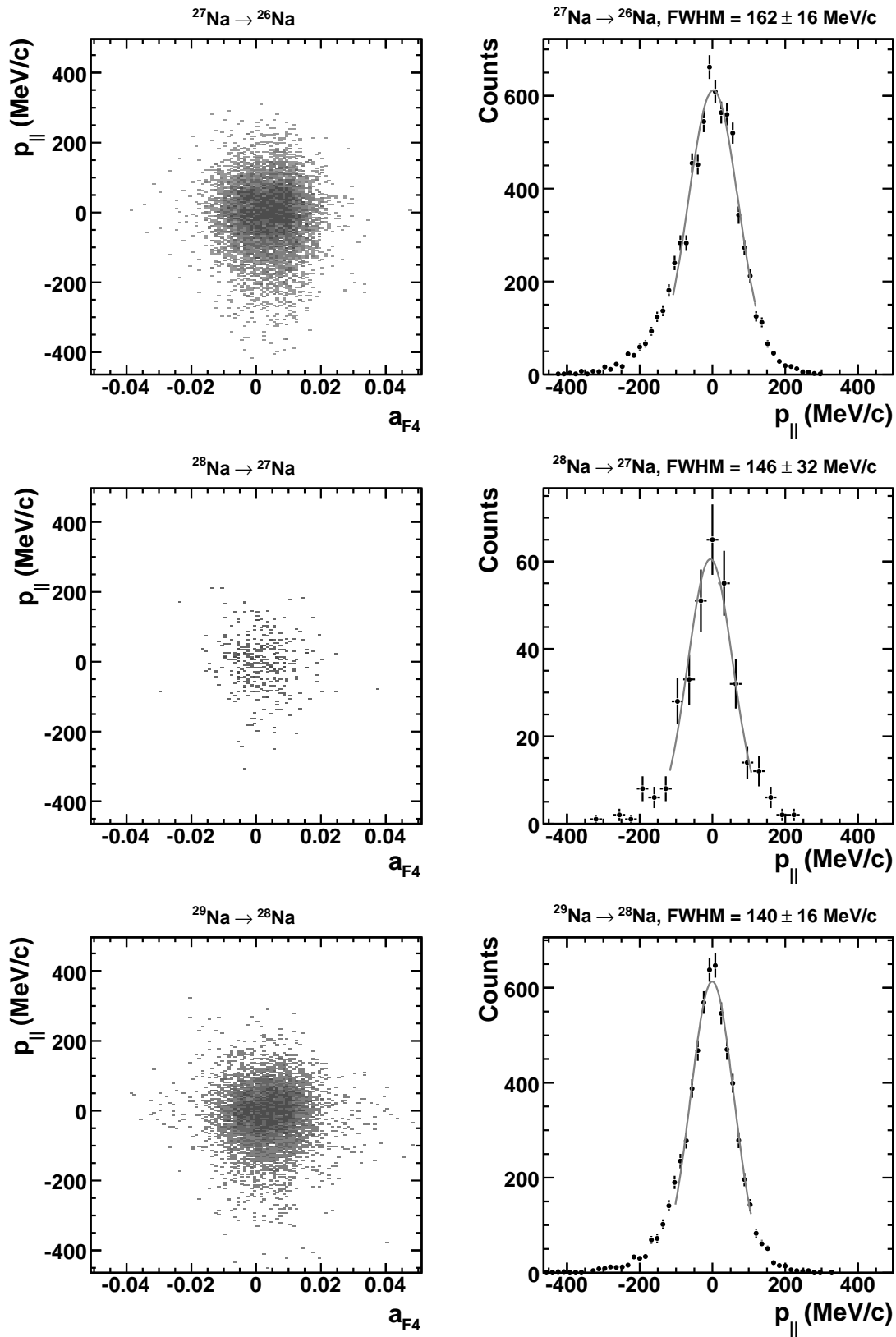


Figure B.12: Momentum distributions measured in $^{27-29}\text{Na}$ one-neutron knockout.

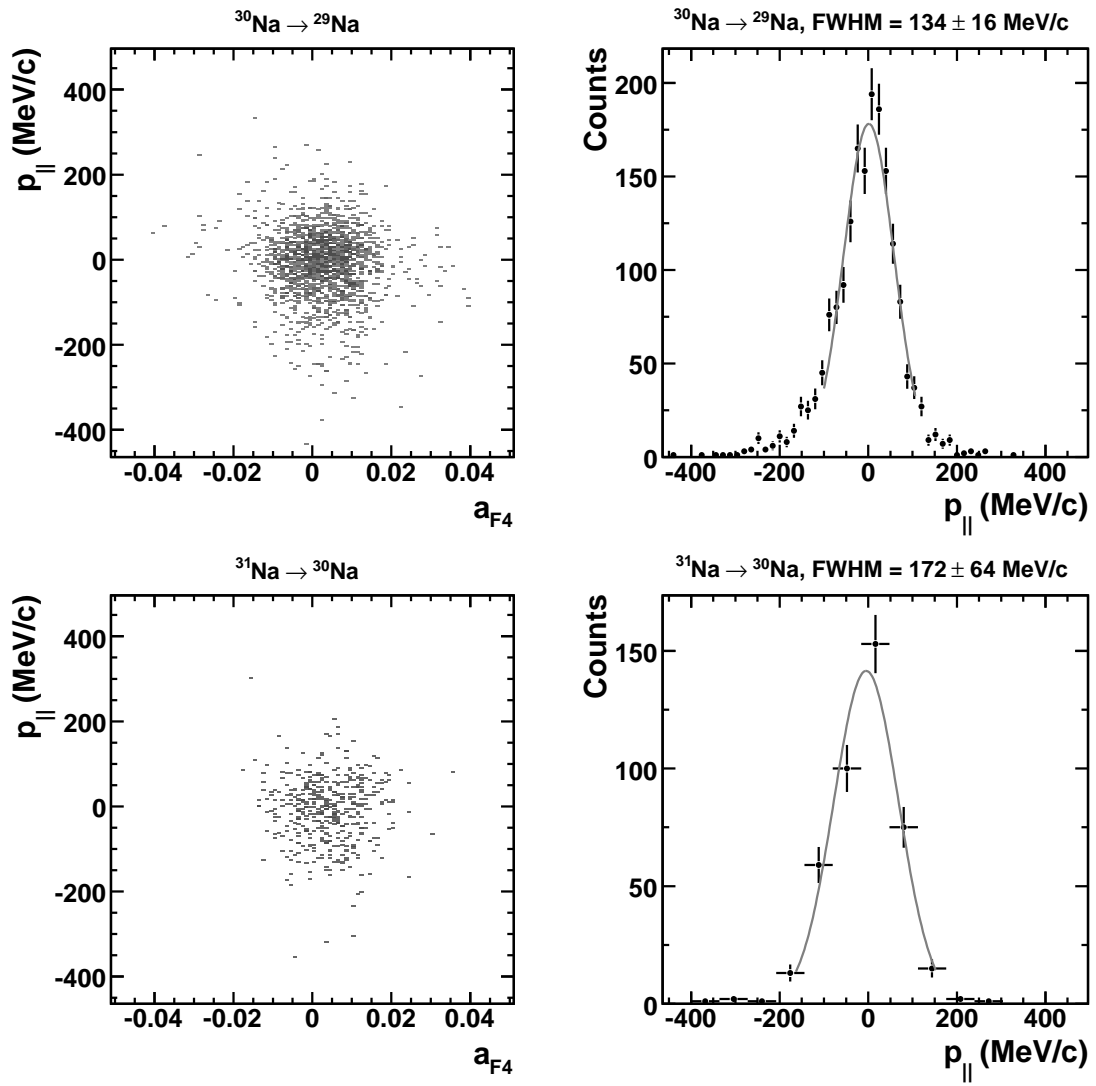


Figure B.13: Momentum distributions measured in $^{30-31}\text{Na}$ one-neutron knockout.

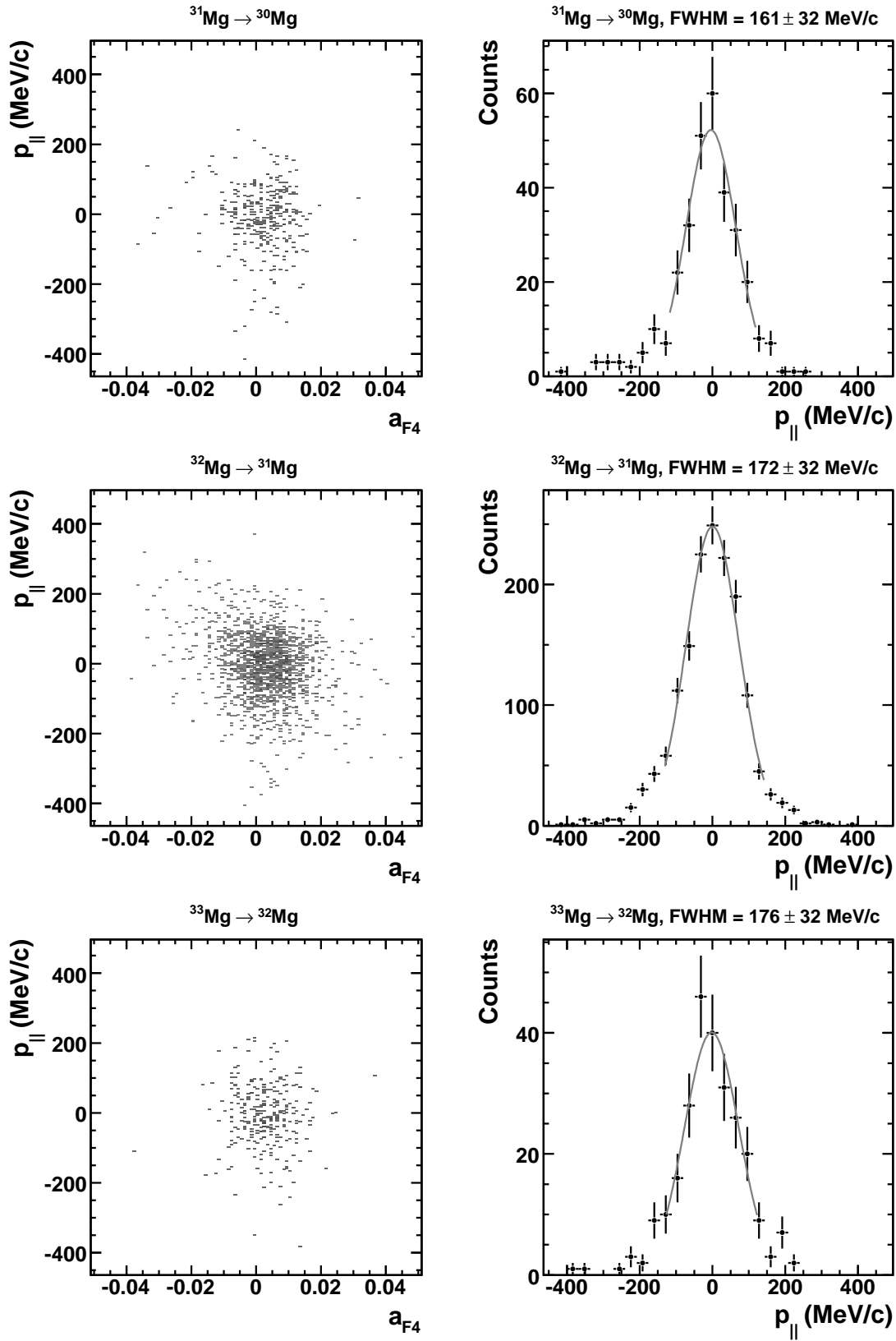


Figure B.14: Momentum distributions measured in $^{31-33}\text{Mg}$ one-neutron knockout.

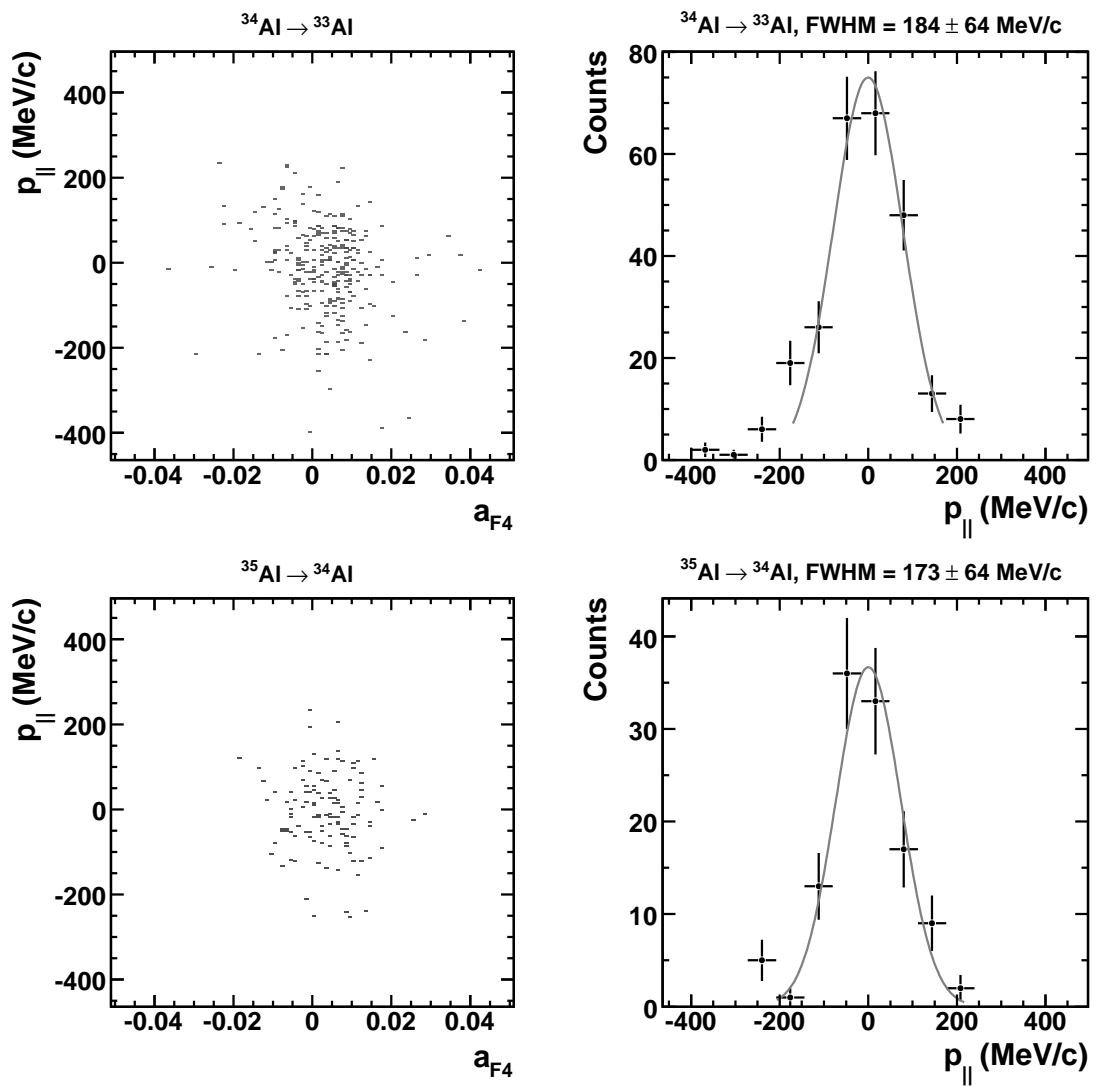


Figure B.15: Momentum distributions measured in $^{34-35}\text{Al}$ one-neutron knockout.

Appendix C

Transmission through the FRS

Transmission of the one-neutron knockout fragments from the intermediate to the final focal planes of the FRS was determined by means of specific MOCADI simulations [Iwa97]. The detector setup and the optics used in this experiment were carefully reproduced in order to reconstruct the measured position distributions and the flight of each nucleus along the spectrometer.

The magnetic fields in the four FRS dipoles were adjusted to select a certain projectile, ${}^A\text{X}$, and a one-neutron knockout fragment, ${}^{A-1}\text{X}$, as reference particles. The different settings, named ${}^A\text{X} \rightarrow {}^{A-1}\text{X}$, are listed in Table C.1 together with the experimental values of the magnetic fields.

FRS setting	B ₁ (T)	B ₂ (T)	B ₃ (T)	B ₄ (T)
${}^{22}\text{N} \rightarrow {}^{21}\text{N}$	1.1995	1.1914	1.1129	1.1092
${}^{20}\text{O} \rightarrow {}^{19}\text{O}$	0.9489	0.9396	0.8694	0.8668
${}^{23}\text{O} \rightarrow {}^{22}\text{O}$	1.0971	1.0929	1.0208	1.0175
${}^{23}\text{O} \rightarrow {}^{22}\text{O}$	1.0970	1.0930	1.0106	1.0073
${}^{24}\text{O} \rightarrow {}^{23}\text{O}$	1.1456	1.1342	1.0564	1.0532
${}^{24}\text{F} \rightarrow {}^{23}\text{F}$	1.0137	1.0034	0.9339	0.9309
${}^{25}\text{F} \rightarrow {}^{24}\text{F}$	1.0574	1.0474	0.9779	0.9747
${}^{25}\text{F} \rightarrow {}^{24}\text{F}$	1.0581	1.0474	0.9680	0.9651

Table C.1: FRS settings and magnetic fields applied to the dipoles. Bold characters refer to specific settings where the magnetic fields B₃ and B₄ were reduced by 1 % in order to centre new fragments from the intermediate to the final focal planes.

In Table C.2, we summarise the transmission results obtained from the simulation of each ${}^A\text{X} \rightarrow {}^{A-1}\text{X}$ setting. They were used to determine the one-neutron knockout cross-sections and represent the percentage of fragments that reached the final FRS focal plane from those produced at the knockout target.

FRS setting	Projectile	Fragment	Transmission (%)
$^{22}\text{N} \rightarrow ^{21}\text{N}$	^{18}C	^{17}C	47 ± 5
	^{19}C	^{18}C	50 ± 5
	^{21}N	^{20}N	57 ± 6
	^{22}N	^{21}N	52 ± 5
$^{20}\text{O} \rightarrow ^{19}\text{O}$	^{14}C	^{13}C	18 ± 2
	^{15}C	^{14}C	24 ± 2
	^{16}C	^{15}C	27 ± 3
	^{16}N	^{15}N	42 ± 4
	^{17}N	^{16}N	41 ± 4
	^{18}N	^{17}N	40 ± 4
	^{19}O	^{18}O	57 ± 6
	^{20}O	^{19}O	49 ± 5
	^{21}O	^{20}O	46 ± 5
	^{21}F	^{20}F	63 ± 6
	^{22}F	^{21}F	56 ± 6
	^{23}F	^{22}F	52 ± 5
	^{24}Ne	^{23}Ne	60 ± 6
	^{25}Ne	^{24}Ne	57 ± 6
^{27}Na	^{26}Na	63 ± 6	
$^{23}\text{O} \rightarrow ^{22}\text{O}$	^{16}C	^{15}C	23 ± 2
	^{17}C	^{16}C	25 ± 3
	^{18}C	^{17}C	35 ± 4
	^{19}N	^{18}N	47 ± 5
	^{20}N	^{19}N	48 ± 5
	^{21}N	^{20}N	46 ± 5
	^{22}O	^{21}O	60 ± 6
	^{23}O	^{22}O	56 ± 6
	^{25}F	^{24}F	65 ± 7
^{26}F	^{25}F	62 ± 6	
$^{23}\text{O} \rightarrow ^{22}\text{O}$	^{16}C	^{15}C	49 ± 5
	^{17}C	^{16}C	51 ± 5
	^{18}C	^{17}C	49 ± 5
	^{19}N	^{18}N	60 ± 6
	^{20}N	^{19}N	57 ± 6
	^{21}N	^{20}N	53 ± 5
	^{22}O	^{21}O	63 ± 6
$^{24}\text{O} \rightarrow ^{23}\text{O}$	^{18}C	^{17}C	43 ± 4
	^{20}N	^{19}N	54 ± 5
	^{21}N	^{20}N	50 ± 5
$^{24}\text{F} \rightarrow ^{23}\text{F}$	^{15}C	^{14}C	18 ± 2
	^{16}C	^{15}C	19 ± 2

Table C.2 Continued on next page.

FRS setting	Projectile	Fragment	Transmission (%)
	^{17}C	^{16}C	25 ± 2
	^{18}N	^{17}N	42 ± 4
	^{19}N	^{18}N	42 ± 4
	^{20}N	^{19}N	39 ± 4
	^{20}O	^{19}O	55 ± 5
	^{21}O	^{20}O	51 ± 5
	^{22}O	^{21}O	48 ± 5
	^{23}F	^{22}F	58 ± 6
	^{24}F	^{23}F	55 ± 5
	^{26}Ne	^{25}Ne	61 ± 6
	^{27}Ne	^{26}Ne	57 ± 6
	^{28}Na	^{27}Na	72 ± 7
	^{29}Na	^{28}Na	63 ± 6
	^{30}Na	^{29}Na	57 ± 6
	^{31}Mg	^{30}Mg	70 ± 7
	^{32}Mg	^{31}Mg	65 ± 7
^{34}Al	^{33}Al	72 ± 7	
^{35}Al	^{34}Al	66 ± 7	
$^{25}\text{F} \rightarrow ^{24}\text{F}$	^{16}C	^{15}C	21 ± 2
	^{17}C	^{16}C	27 ± 3
	^{18}C	^{17}C	37 ± 4
	^{18}N	^{17}N	44 ± 4
	^{19}N	^{18}N	44 ± 4
	^{20}N	^{19}N	44 ± 4
	^{21}O	^{20}O	54 ± 5
	^{22}O	^{21}O	52 ± 5
	^{23}O	^{22}O	49 ± 5
	^{24}O	^{23}F	57 ± 6
	^{25}F	^{24}F	56 ± 6
	^{27}Ne	^{26}Ne	64 ± 6
	^{28}Ne	^{27}Ne	57 ± 6
	^{29}Ne	^{28}Ne	58 ± 6
^{30}Na	^{29}Na	66 ± 7	
^{31}Na	^{30}Na	61 ± 6	
^{33}Mg	^{32}Mg	68 ± 7	
$^{25}\text{F} \rightarrow ^{24}\text{F}$	^{16}C	^{15}C	48 ± 5
	^{17}C	^{16}C	42 ± 4
	^{18}N	^{17}N	55 ± 6
	^{19}N	^{18}N	51 ± 5
	^{20}N	^{19}N	47 ± 5
	^{21}O	^{20}O	57 ± 6

Table C.2 Continued on next page.

FRS setting	Projectile	Fragment	Transmission (%)
	^{22}O	^{21}O	53 ± 5
	^{24}F	^{23}F	58 ± 6
	^{25}F	^{24}F	57 ± 6

Table C.2: Transmission of the one-neutron knockout fragments between the intermediate and final FRS focal planes.

Appendix D

γ -ray measurements

The γ measurements performed in this experiment provided us with information about the different fragment states populated in the one-neutron knockout reaction. In the context of Serber model [Ser47], we assumed that the fragment was not affected by the process and thus the observed excited states offer valuable information about the structure of the initial projectile.

In this appendix, we present in Figs. D.1–D.14 the γ spectra obtained in coincidence with the one-neutron knockout of several projectiles, namely, $^{15-17}\text{C}$, $^{17-20}\text{N}$, $^{20-22}\text{O}$ and $^{22-25}\text{F}$.

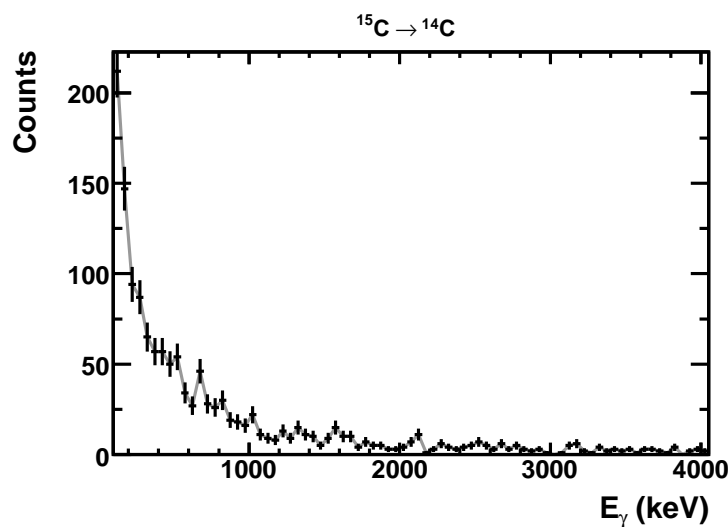


Figure D.1: γ spectrum measured in coincidence with ^{15}C one-neutron knockout.

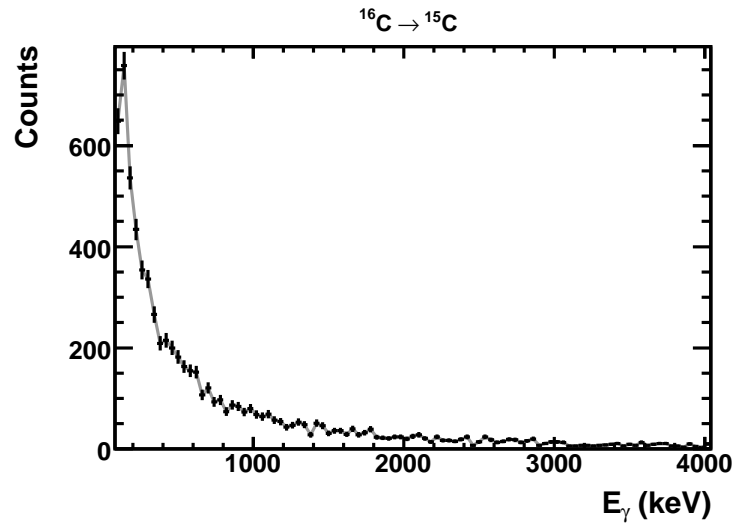


Figure D.2: γ spectrum measured in coincidence with ^{16}C one-neutron knockout.

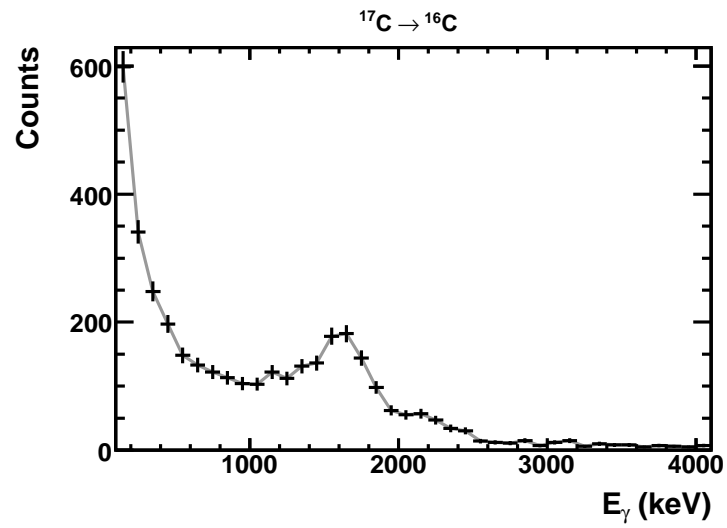


Figure D.3: γ spectrum measured in coincidence with ^{17}C one-neutron knockout.

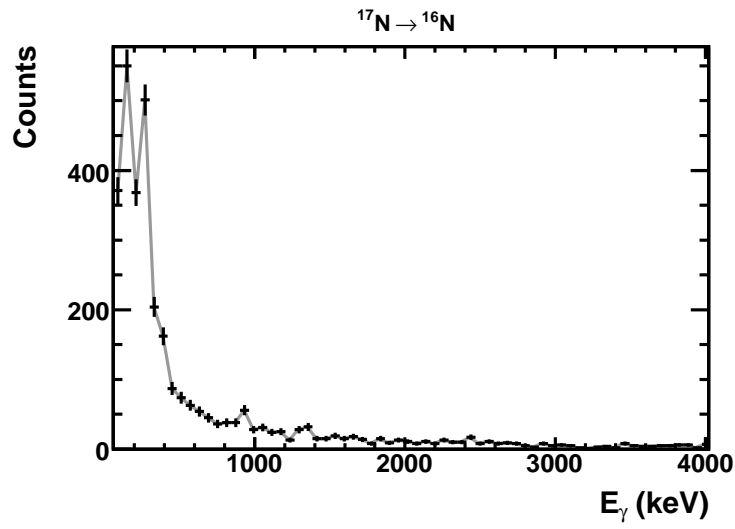


Figure D.4: γ spectrum measured in coincidence with ^{17}N one-neutron knockout.

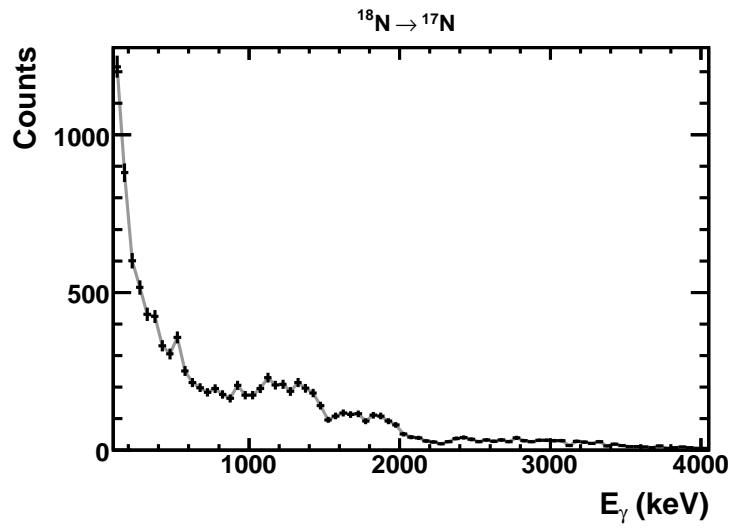


Figure D.5: γ spectrum measured in coincidence with ^{18}N one-neutron knockout.

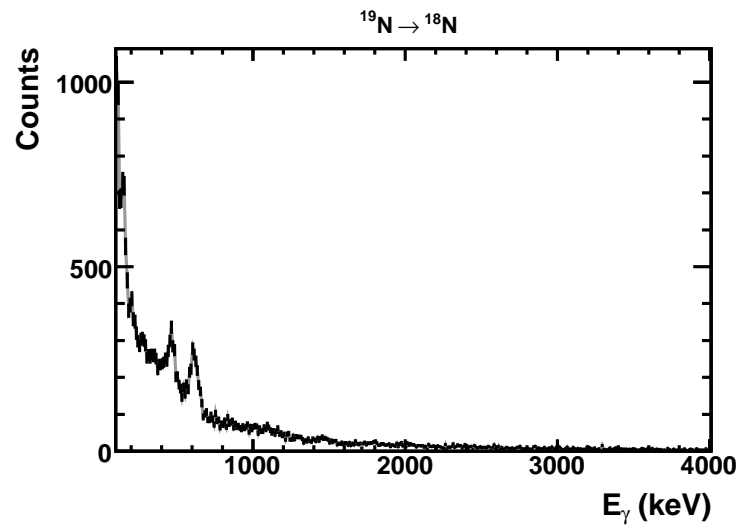


Figure D.6: γ spectrum measured in coincidence with ^{19}N one-neutron knockout.

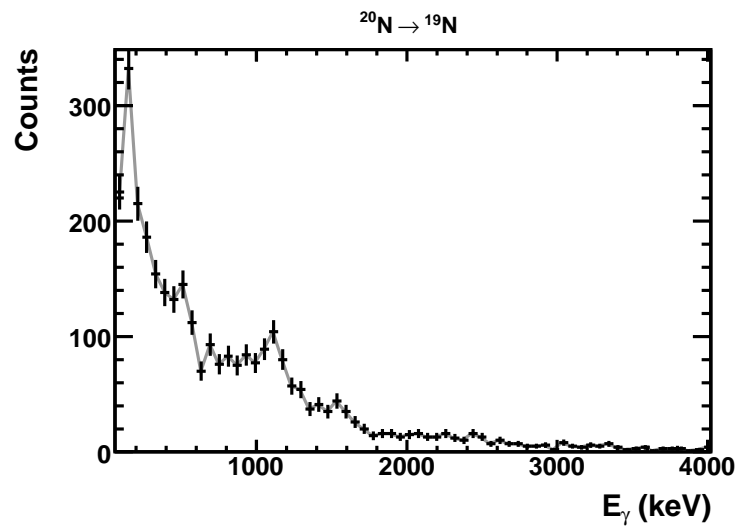


Figure D.7: γ spectrum measured in coincidence with ^{20}N one-neutron knockout.

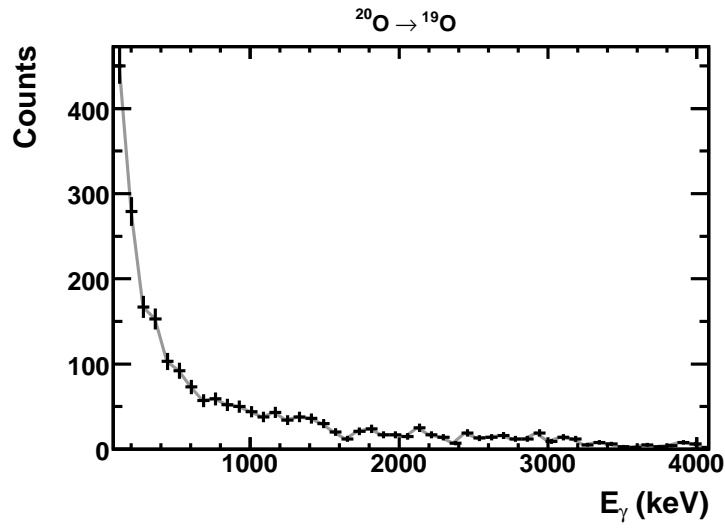


Figure D.8: γ spectrum measured in coincidence with ^{20}O one-neutron knockout.

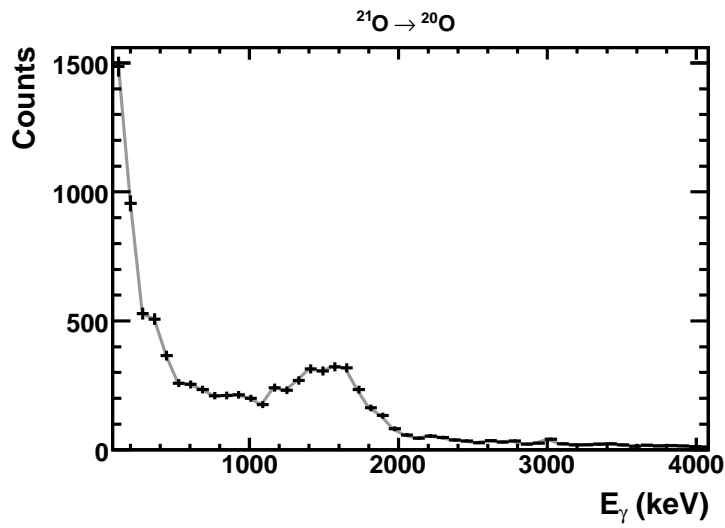


Figure D.9: γ spectrum measured in coincidence with ^{21}O one-neutron knockout.

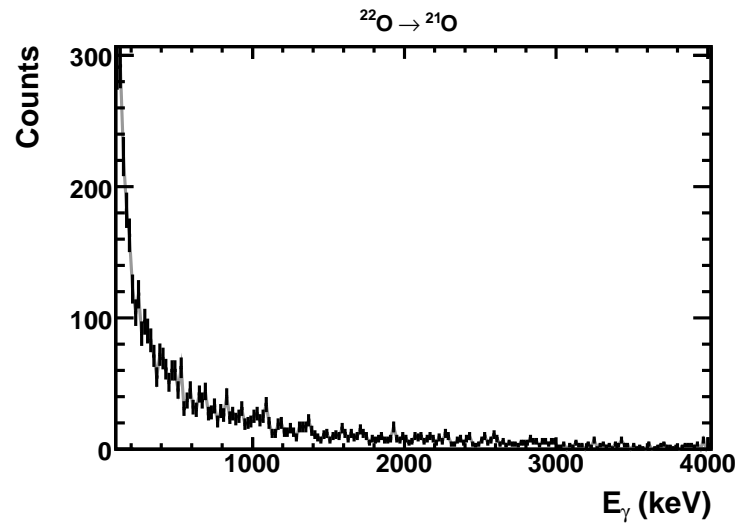


Figure D.10: γ spectrum measured in coincidence with ^{22}O one-neutron knockout.

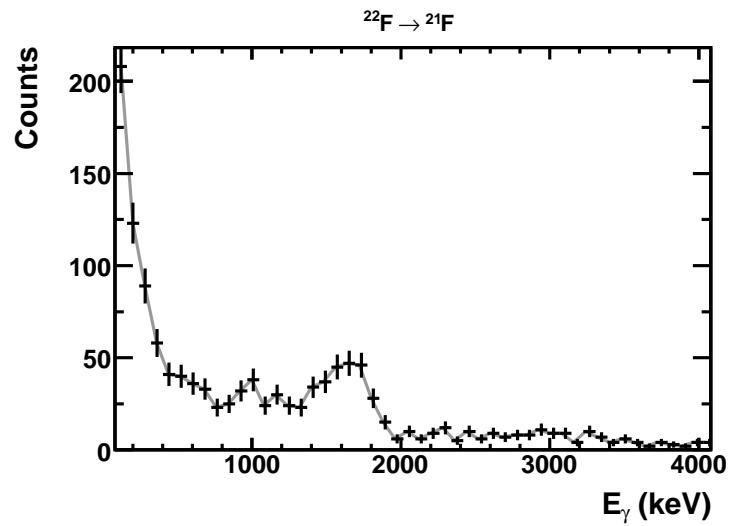


Figure D.11: γ spectrum measured in coincidence with ^{22}F one-neutron knockout.

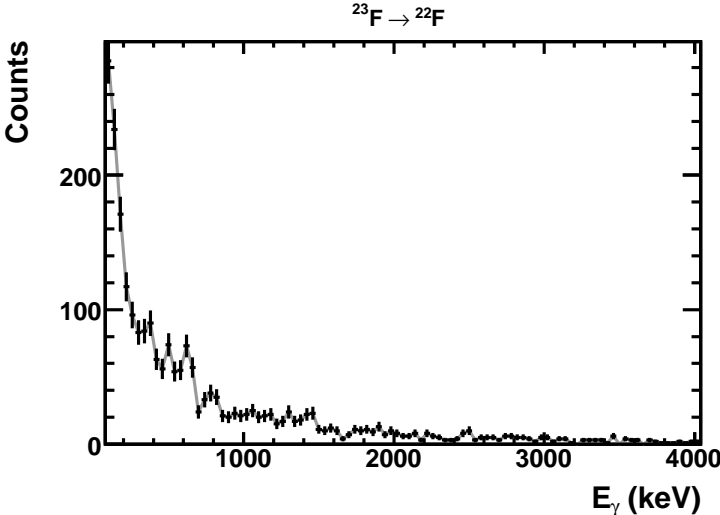


Figure D.12: γ spectrum measured in coincidence with ^{23}F one-neutron knockout.

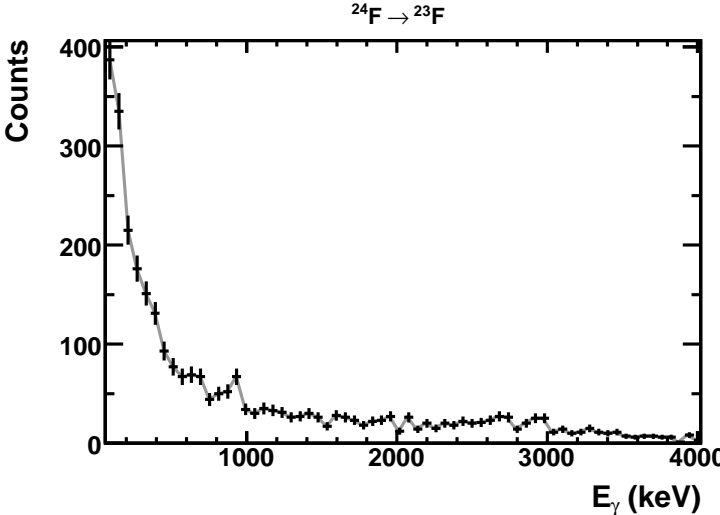


Figure D.13: γ spectrum measured in coincidence with ^{24}F one-neutron knockout.

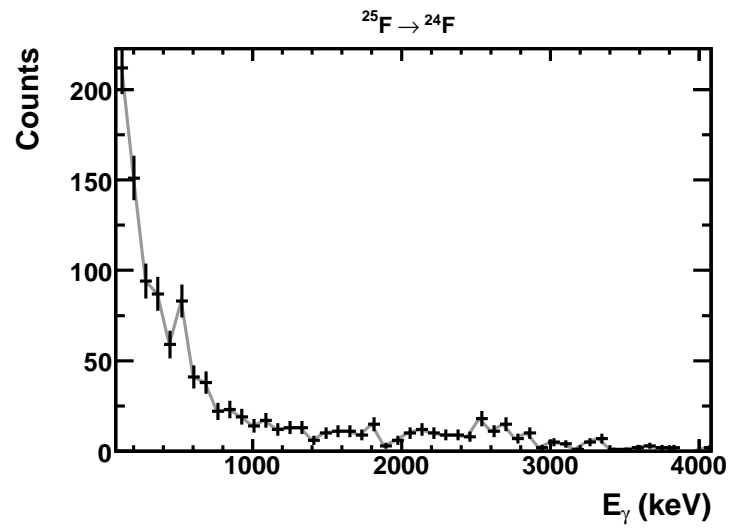


Figure D.14: γ spectrum measured in coincidence ^{25}F one-neutron knockout.

Bibliography

- [Aud93] G. Audi and A. H. Wapstra, *The 1993 atomic mass evaluation : (I) Atomic mass table*, Nucl. Phys. A **565** (1993) 1.
- [Aud95] G. Audi and A. H. Wapstra, *The 1995 update to the atomic mass evaluation*, Nucl. Phys. A **595** (1995) 409.
- [Aud97] G. Audi *et al.*, *The N_{UBASE} evaluation of nuclear and decay properties*, Nucl. Phys. A **624** (1997) 1.
- [Aum98] T. Aumann *et al.*, *Manifestation of the halo structure in momentum distributions from ${}^6\text{He}$ fragmentation*, Nucl. Phys. A **640** (1998) 24.
- [Aum00] T. Aumann *et al.*, *One-Neutron Knockout from Individual Single-Particle States of ${}^{11}\text{Be}$* , Phys. Rev. Lett. **84** (2000) 35.
- [Aum05] T. Aumann, *Reactions with fast radioactive beams of neutron-rich nuclei*, Eur. Phys. J. A **26** (2005) 441.
- [Bau98] T. Baumann *et al.*, *Longitudinal momentum distributions of ${}^{16,18}\text{C}$ fragments after one-neutron removal from ${}^{17,19}\text{C}^*$* , Phys. Lett. B **439** (1998) 256.
- [Bau99] T. Baumann, *Longitudinal momentum distributions of ${}^8\text{B}$ and ${}^{19}\text{C}$: Signatures for one-proton and one-neutron halos*, Ph.D. thesis, Justus-Liebig Universität Gießen (1999).
- [Baz95] D. Bazin *et al.*, *One-neutron halo of ${}^{19}\text{C}$* , Phys. Rev. Lett. **74** (1995) 3569.
- [Baz98] D. Bazin *et al.*, *Probing the halo structure of ${}^{19,17,15}\text{C}$ and ${}^{14}\text{B}$* , Phys. Rev. C **57** (1998) 2156.
- [Baz03] D. Bazin *et al.*, *New direct reaction: Two-Proton Knockout from Neutron-Rich Nuclei*, Phys. Rev. Lett. **91** (2003) 012501.
- [Bel05] M. Belleguic *et al.*, *Search for neutron excitations across the $N=20$ shell gap in ${}^{25-29}\text{Ne}$* , Phys. Rev. C **72** (2005) 054316.
- [Ber] *Lawrence Berkeley National Laboratory*, <http://www.lbl.gov/> .

- [Ber92] C. A. Bertulani and K. W. McVoy, *Momentum distributions in reactions with radioactive beams*, Phys. Rev. C **46** (1992) 2638.
- [Bev92] P. R. Bevington and D. K. Robinson, *Data reduction and error analysis for the physical sciences*, McGraw-Hill (1992).
- [Boi02] H. Boie, *Aufbau eines Experimentes zur Messung der Emissionswahrscheinlichkeit von Bremsstrahlung im alpha-Zerfall von ^{210}Po* , Ph.D. thesis, Universität Heidelberg (2002).
- [Bro88] B. A. Brown and B. H. Wildenthal, *Status of the nuclear shell model*, Annu. Rev. Nucl. Part. Sci **38** (1988) 29.
- [Bro96] B. A. Brown, A. Csóto and R. Sherr, *Coulomb displacement energy and the low-energy astrophysical S_{17} factor for the $^7\text{Be}(p,)^8\text{B}$ reaction*, Nucl. Phys. A **597** (1996) 66.
- [Bro03] B. A. Brown, P. G. Hansen and J. A. Tostevin, *Comment on Experimental Evidence of Core Modification in the Near Drip-Line Nucleus ^{23}O* , Phys. Rev. Lett. **90** (2003) 159201.
- [Car87] D. Carey, *The optics of charged particle beams*, Harwood Academic Publishers (1987).
- [Cat05a] W. N. Catford *et al.*, *First experiments on transfer with radioactive beams using the TIARA array*, Eur. Phys. J A **25** s01 (2005) 245.
- [Cat05b] W. N. Catford *et al.*, *Nucleon transfer via (d,p) using TIARA with a ^{24}Ne radioactive beam*, J. Phys. G **31** (2005) S1655.
- [Cor01] D. Cortina-Gil *et al.*, *One-nucleon removal cross-sections for $^{17-19}\text{C}$ and $^{8,10}\text{B}$* , Eur. Phys. J. A **10** (2001) 49.
- [Cor02] D. Cortina-Gil *et al.*, *Experimental evidence for the ^8B ground state configuration*, Phys. Lett. B **529** (2002) 36.
- [Cor04] D. Cortina-Gil *et al.*, *Shell Structure of the Near-Dripline Nucleus ^{23}O* , Phys. Rev. Lett. **93** (2004) 062501.
- [Cur86] M. S. Curtin *et al.*, *Lifetime measurements of neutron-rich light isotopes Be^{14} and C^{17}* , Phys. Rev. Lett. **56** (1986) 34.
- [Dét78] C. Détraz *et al.*, *Beta decay of $^{27-32}\text{Na}$ and their descendants*, Phys. Rev. C **19** (1978) 164.
- [Dom06] Z. Dombrádi *et al.*, *Vanishing $N=20$ Shell Gap: Study of Excited States in $^{27,28}\text{Ne}$* , Phys. Rev. Lett. **96** (2006) 182501.

- [Duf86] J. P. Dufour *et al.*, *Beta Decay of ^{17}C , ^{19}N , ^{22}O , ^{24}F , ^{26}Ne , ^{32}Al , ^{34}Al , $^{35-36}\text{Si}$, $^{36-37-38}\text{P}$, ^{40}S* , Z. Phys. A **324** (1986) 487.
- [Ebe01] J. Eberth *et al.*, *MINIBALL - A Ge detector array for radioactive ion beam facilities*, Prog. Part. Nucl. Phys. **46** (2001) 389.
- [Esb96] H. Esbensen, *Momentum distributions in stripping reactions of single-nucleon halo nuclei*, Phys. Rev. C **53** (1996) 2007.
- [Fan00] D. Q. Fang *et al.*, *Measurements of total reaction cross sections for some light nuclei at intermediate energies*, Phys. Rev. C **61** (2000) 064311.
- [Fer03] J. Fernández-Vázquez, *Investigation of the structure of light neutron rich isotopes using breakup reactions at relativistic energies*, Ph.D. thesis, Universidade de Santiago de Compostela (2003).
- [Fer07] B. Fernández-Domínguez *et al.*, *Single particle structure of exotic nuclei with transfer reactions*, Prog. Part. Nucl. Phys. **59** (2007) 389.
- [Fir07] R. B. Firestone, *Nuclear Data Sheets for $A=24$* , Nuclear Data Sheets **108** (2007) 2319.
- [Fri83] W. A. Friedman, *Heavy ion projectile fragmentation: A reexamination*, Phys. Rev. C **27** (1983) 569.
- [Fuk04] N. Fukuda *et al.*, *Coulomb and nuclear breakup of a halo nucleus ^{11}Be* , Phys. Rev. C **70** (2004) 054606.
- [Gad06a] A. Gade *et al.*, *Cross-shell excitation in two-proton knockout: Structure of ^{52}Ca* , Phys. Rev. C **74** (2006) 021302.
- [Gad06b] A. Gade *et al.*, *One-neutron knockout in the vicinity of the $N=32$ sub-shell closure: $^9\text{Be}(^{57}\text{Cr}, ^{56}\text{Cr}+\gamma)X$* , Phys. Rev. C **74** (2006) 047302.
- [Gad08] A. Gade and T. Glasmacher, *In-beam γ -ray spectroscopy of bound states with fast exotic ion beams*, Prog. Part. Nucl. Phys. **60** (2008) 161.
- [GAN] *Grand Accélérateur National d'Ions Lourds*, <http://www.ganil.fr/> .
- [Gau06] L. Gaudefroy *et al.*, *Reduction of the Spin-Orbit Splittings at the $N=28$ Shell Closure*, Phys. Rev. Lett. **97** (2006) 092501.
- [Gau08] L. Gaudefroy *et al.*, *Structure of the $N=27$ isotones derived from the $^{44}\text{Ar}(d,p)^{45}\text{Ar}$ reaction*, Phys. Rev. C **78** (2008) 034307.
- [Gea] *Geant4*, <http://geant4.web.cern.ch/geant4/> .

- [Gei92] H. Geissel *et al.*, *The GSI projectile fragment separator (FRS): a versatile magnetic system for relativistic heavy ions*, Nucl. Instr. Meth. B **70** (1992) 286.
- [Gol74] A. S. Goldhaber, *Statistical models for fragmentation processes*, Phys. Lett. B **53** (1974) 306.
- [Gre75] D. E. Greiner *et al.*, *Momentum Distributions of Isotopes Produced by Fragmentation of Relativistic ^{12}C and ^{16}O Projectiles*, Phys. Rev. Lett. **35** (1975) 152.
- [GSI] *GSI Helmholtzzentrum für Schwerionenforschung GmbH*, <http://www.gsi.de>.
- [Gup00] R. K. Gupta *et al.*, *The halo structure of neutron-drip line nuclei: (neutron) cluster-core model*, J. Phys. G **26** (2000) L23.
- [Han87] P. G. Hansen and B. Jonson, *The Neutron Halo of Extremely Neutron-Rich Nuclei*, Europhys. Lett. **4** (1987) 409.
- [Han95] P. G. Hansen, A. S. Jensen and B. Jonson, *Nuclear halos*, Annu. Rev. Nucl. Part. Sci. **45** (1995) 591.
- [Han96] P. G. Hansen, *Momentum content of Single-Nucleon Halos*, Phys. Rev. Lett. **77** (1996) 1016.
- [Han03] P. G. Hansen and T. A. Tostevin, *Direct reactions with exotic nuclei*, Annu. Rev. Nucl. Part. Sci. **53** (2003) 219.
- [Hax49] O. Haxel, J. H. D. Jensen and H. E. Suess, *On the Magic Numbers in Nuclear Structure*, Phys. Rev. **75** (1949) 1766.
- [Hen96] K. Hencken, G. Bertsch and H. Esbensen, *Breakup reactions of the halo nuclei ^{11}Be and ^8B* , Phys. Rev. C **54** (1996) 3043.
- [Him08] P. Himpe *et al.*, *g factor of the exotic $N=21$ isotope ^{34}Al : probing the $N=20$ and $N=28$ shell gaps at the border of the island of inversion*, Phys. Lett. B **658** (2008) 203.
- [Hli98] V. Hlinka *et al.*, *Time projection chambers for tracking and identification of radioactive beams*, Nucl. Instr. Meth. A **419** (1998) 503.
- [Iwa97] N. Iwasa *et al.*, *The GSI projectile fragment separator (FRS): a versatile magnetic system for relativistic heavy ions*, Nucl. Instr. Meth. B **126** (1997) 284.
- [Iwa00a] H. Iwasaki *et al.*, *Low-lying intruder 1^- state in ^{12}Be and the melting of the $N=8$ shell closure*, Phys. Lett. B **491** (2000) 8.

- [Iwa00b] H. Iwasaki *et al.*, *Quadrupole deformation of ^{12}Be studied by proton inelastic scattering*, Phys. Lett. B **481** (2000) 7.
- [Kan02] R. Kanungo *et al.*, *Experimental Evidence of Core Modification in the Near Drip-Line Nucleus ^{23}O* , Phys. Rev. Lett. **88** (2002) 142502.
- [Kan09] R. Kanungo *et al.*, *One-Neutron Removal Measurement Reveals ^{24}O as a new Doubly Magic Nucleus*, Phys. Rev. Lett. **102** (2009) 152501.
- [Kob88] T. Kobayashi *et al.*, *Projectile Fragmentation of the Extremely Neutron-Rich Nucleus ^{11}Li at 0.79 GeV/nucleon*, Phys. Rev. Lett. **60** (1988) 2599.
- [Kra01] G. J. Kramer, H. P. Blok and L. Lapikás, *A consistent analysis of $(e, e'p)$ and $(d, ^3\text{He})$ experiments*, Nucl. Phys. A **679** (2001) 267.
- [Lia90] E. Liatard *et al.*, *Matter Distribution in Neutron-Rich Light Nuclei and Total Reaction Cross-Section*, Europhys. Lett. **13** (1990) 401.
- [Mad01] V. Maddalena *et al.*, *Single-neutron knockout reactions: Application to the spectroscopy of $^{16,17,19}\text{C}$* , Phys. Rev. C **63** (2001) 024613.
- [Mai09] P. Maierbeck *et al.*, *Structure of ^{55}Ti from relativistic one-neutron knockout*, Phys. Lett. B **675** (2009) 22.
- [Mar96] F. M. Marqués *et al.*, *Neutrons from the breakup of ^{19}C* , Phys. Lett. B **381** (1996) 407.
- [May49] M. G. Mayer, *On Closed Shells in Nuclei. II*, Phys. Rev. **75** (1949) 1969.
- [Mot95] T. Motobayashi *et al.*, *Large deformation of the very neutron-rich nucleus ^{32}Mg from intermediate-energy Coulomb excitation*, Phys. Lett. B **346** (1995) 9.
- [Mue01] W. F. Mueller *et al.*, *Thirty-two-fold segmented germanium detectors to identify γ -rays from intermediate-energy exotic beams*, Nucl. Inst. Meth. Phys. Res. A **466** (2001) 492.
- [Nak99] T. Nakamura *et al.*, *Coulomb Dissociation of ^{19}C and its Halo Structure*, Phys. Rev. Lett. **83** (1999) 1112.
- [Nau80] F. Naulin *et al.*, *Mass Excess and Excited States of ^{14}B and ^{18}N from the $(^{14}\text{C}, ^{14}\text{B})$ and $(^{18}\text{O}, ^{18}\text{N})$ Reactions*, J. Phys. Lett. **41** (1980) L79.
- [Noc05] C. Nociforo *et al.*, *Coulomb breakup of ^{23}O* , Phys. Lett. B **605** (2005) 79.
- [NSC] *National Superconducting Cyclotron Laboratory at Michigan State University*, <http://www.nscl.msu.edu/> .

- [Obe05] A. Obertelli *et al.*, *N=16 subshell closure from stability to the neutron drip line*, Phys. Rev. C **71** (2005) 024304.
- [Obe06] A. Obertelli *et al.*, *γ spectroscopy of $^{25,27}\text{Ne}$ and $^{26,27}\text{Na}$* , Phys. Rev. C **74** (2006) 064305.
- [Orr91] N. A. Orr *et al.*, *New mass measurements of neutron-rich nuclei near N=20*, Phys. Lett. B **258** (1991) 29.
- [Orr92] N. A. Orr *et al.*, *Momentum distributions of ^9Li fragments following the breakup of ^{11}Li* , Phys. Rev. Lett. **69** (1992) 2050.
- [Ots01a] T. Otsuka, *Monte Carlo shell model*, Nucl. Phys. A **693** (2001) 383.
- [Ots01b] T. Otsuka *et al.*, *Magic Numbers in Exotic Nuclei and Spin-Isospin Properties of the NN Interaction*, Phys. Rev. Lett. **87** (2001) 082502.
- [Ots01c] T. Otsuka *et al.*, *Shell model results for neutron-rich nuclei*, Nucl. Phys. A **682** (2001) 155c.
- [Oza98] A. Ozawa *et al.*, *Measurements of interaction cross-sections for Carbon isotopes at relativistic energies and the halo structure in C-19*, RIKEN-AF-NP-294 (1998) 13.
- [Oza00] A. Ozawa *et al.*, *New Magic Number, N = 16, near the Neutron Drip Line*, Phys. Rev. Lett. **84** (2000) 5493.
- [Oza08] A. Ozawa *et al.*, *Measurement of the reaction cross section of ^{18}C and observations of fragments from ^{17}C and ^{18}C at 80 A MeV*, Phys. Rev. C **78** (2008) 054313.
- [Pad05] S. W. Padgett *et al.*, *Spectroscopy of ^{25}Ne and the N=16 magic number*, Phys. Rev. C **72** (2005) 064330.
- [Pal03] R. Palit *et al.*, *Exclusive measurement of breakup reactions with the one-neutron halo nucleus ^{11}Be* , Phys. Rev. C **68** (2003) 034318.
- [Pan97] V. R. Pandharipande, I. Sick and P. K. A. deWitt Huberts, *Independent particle motion and correlations in fermion systems*, Rev. Mod. Phys. **69** (1997) 981.
- [Pfü94] M. Pfützner *et al.*, *Energy deposition by relativistic heavy ions in thin argon absorbers*, Nucl. Instr. Meth. B **86** (1994) 213.
- [PMT] *Hamamatsu PMT*, <http://sales.hamamatsu.com/en/products/electron-tube-division/detectors/photomultiplier-modulesphp> .
- [Pra91] M. Pravikoff *et al.*, *The beta decay of $^{18}\text{C}^*$* , Nucl. Phys. A **528** (1991) 225.

- [Pra03] U. D. Pramanik *et al.*, *Coulomb breakup of the neutron-rich isotopes ^{15}C and ^{17}C* , Phys. Lett. B **551** (2003) 63.
- [Put83] G. D. Putt *et al.*, *The mass of ^{18}N* , Nucl. Phys. A **399** (1983) 190.
- [Ree99] A. T. Reed *et al.*, *Radioactivity of neutron-rich oxygen, fluorine, and neon isotopes*, Phys. Rev. C **60** (1999) 024311.
- [RIK] *RIKEN Nishina Center for Accelerator-Based Science*, <http://www.rarf.riken.go.jp/Eng/> .
- [ROO] *ROOT*, <http://root.cern.ch/drupal/> .
- [Sag94] H. Sagawa and N. Takigawa, *Projectile fragmentation of halo nuclei in peripheral direct reaction model*, Phys. Rev. C **50** (1994) 985.
- [Sau00] E. Sauvan *et al.*, *One-neutron removal reactions on neutron-rich psd-shell nuclei*, Phys. Lett. B **491** (2000) 1.
- [Sau04] E. Sauvan *et al.*, *One-neutron removal reactions on light neutron-rich nuclei*, Phys. Rev. C **69** (2004) 044603.
- [Ser47] R. Serber, *The Production of High Energy Neutrons for Stripping*, Phys. Rev. **72** (1947) 1008.
- [Sim07] H. Simon *et al.*, *Systematic investigation of the drip-line nuclei ^{11}Li and ^{14}Be and their unbound subsystems ^{10}Li and ^{13}Be* , Nucl. Phys. A **791** (2007) 267.
- [Sme98] M. Smedberg, *Probing the drip-lines through momentum distributions*, Ph.D. thesis, Chalmers Tekniska Högskola (1998).
- [Soh08] D. Sohler *et al.*, *In-beam gamma-ray spectroscopy of the neutron-rich nitrogen isotopes $^{19-22}\text{N}$* , Phys. Rev. C **77** (2008) 044303.
- [Sta04] M. Stanoiu *et al.*, *$N = 14$ and 16 shell gaps in neutron-rich oxygen isotopes*, Phys. Rev. C **69** (2004) 034312.
- [Sto83] M. H. Storm, A. Watt and R. R. Whitehead, *Crossing of single-particle energy levels resulting from neutron excess in the sd shell*, J. Phys. G **9** (1983) L165.
- [Sym79] T. J. M. Symons *et al.*, *Observation of New Neutron-Rich Isotopes by Fragmentation of 205-MeV/Nucleon ^{40}Ar Ions*, Phys. Rev. Lett. **42** (1979) 40.
- [Tan85] I. Tanihata *et al.*, *Measurements of Interaction Cross Sections and Nuclear Radii in the Light p-Shell Region*, Phys. Rev. Lett. **55** (1985) 2676.

- [Ter06] J. Terry *et al.*, *Direct evidence for the onset of intruder configurations in neutron-rich Ne isotopes*, Phys. Lett. B **640** (2006) 86.
- [Thi75] C. Thibault *et al.*, *Direct measurements of masses of ^{11}Li and $^{26-32}\text{Na}$ with an on-line mass spectrometer*, Phys. Rev. C **12** (1975) 644.
- [Til98] D. R. Tilley *et al.*, *Energy levels of light nuclei, $A=20^*$* , Nucl. Phys. A **636** (1998) 249.
- [Tos99] J. A. Tostevin, *Core excitation in halo nucleus break-up*, J. Phys. G **25** (1999) 735.
- [Tri06] V. Tripathi *et al.*, *β -delayed γ spectroscopy of neutron rich $^{27,28,29}\text{Na}$* , Phys. Rev. C **73** (2006) 054303.
- [TUM] *Technische Universität München*, <http://portal.mytum.de/welcome> .
- [Uts99] Y. Utsuno *et al.*, *Varying shell gap and deformation in $N \sim 20$ unstable nuclei studied by the Monte Carlo shell model*, Phys. Rev. C **60** (1999) 054315.
- [Uts04] Y. Utsuno *et al.*, *Onset of intruder ground state in exotic Na isotopes and evolution of the $N=20$ shell gap*, Phys. Rev. C **70** (2004) 044307.
- [Vil91] A. C. C. Villari *et al.*, *Measurements of reaction cross sections for neutron-rich exotic nuclei by a new direct method*, Phys. Lett. B **268** (1991) 345.
- [War89] E. K. Warburton and D. J. Millener, *Structure of C^{17} and N^{17}* , Phys. Rev. C **39** (1989) 1120.
- [Wei35] C. F. v. Weizsäcker, *Zur Theorie der Kernmassen*, Z. Physik **96** (1935) 431.
- [Wes79] G. D. Westfall *et al.*, *Production of Neutron-Rich Nuclides by Fragmentation of 212-MeV/amu ^{48}Ca* , Phys. Rev. Lett. **43** (1979) 1859.
- [Wie08] M. Wiedeking *et al.*, *Nuclear structure of ^{18}N and the neighboring $N = 11$ isotones*, Phys. Rev. C **77** (2008) 054305.
- [Wil80] B. H. Wildenthal and W. Chung, *Collapse of the conventional shell-model ordering in the very-neutron-rich isotopes of Na and Mg*, Phys. Rev. C **22** (1980) 2260.
- [Win01] J. S. Winfield *et al.*, *Single-neutron transfer from $^{11}\text{Be}_{gs}$ via the (p, d) reaction with a radioactive beam*, Nucl. Phys. A **683** (2001) 48.
- [Wou88] J. M. Wouters *et al.*, *Direct mass measurements of the neutron-rich light isotopes of lithium through fluorine*, Z. Phys. A **331** (1988) 229.

- [Yan03] Y. Yanagisawa *et al.*, *The first excited state of ^{30}Ne studied by proton inelastic scattering in reversed kinematics*, Phys. Lett. B **566** (2003) 84.
- [Yon06] K. Yoneda *et al.*, *Two-neutron knockout from neutron-deficient ^{34}Ar , ^{30}S , and ^{26}Si* , Phys. Rev. C **74** (2006) 021303.

Acknowledgements

This work relies on the help of several people to whom I would like to express my gratitude. First of all, those ones who, on April 2006, took care of the experimental setup or participated in the measurements carried out in the FRS, at GSI.

I am also indebted to my supervisor, Dolores Cortina Gil, who introduced me in the research field of Nuclear Physics and gave me the opportunity of joining the Experimental Group of Nuclei and Particles (GENP) in the *Universidade of Santiago de Compostela*. I would also like to thank to Héctor Álvarez Pol and David Pérez Loureiro, who really helped me in the daily work, making things working, and Saúl Beceiro Novo because he supported me in many occasions.

Important contributions arrived from Roman Gernhauser, who was able to understand the tracking difficulties found in this experiment and, together with Peter Maierbeck, made possible the analysis of the γ -ray measurements carried out. Both of them received me for a couple of months in the *Technische Universität München*.

The people from the Department of Fundamental Physics, at the *Chalmers Tekniska Högskola*, who welcomed me so warmly, deserve my most sincere gratitude. I would never be able to finish this work without the help of Mikhail Zhukov and Björn Jonson, to whom I would also like to thank his nice words and his constant support.

Finalmente, tamén quero darlle as gracias á miña familia, meu pai, miña mai eu meu irmán, e a aqueles que me apoiaron e acompañaron durante todo este tempo, especialmente Germam e Normando, que sempre me trae caixas con lapis de cores.

*Et je puis devenir comme les grandes personnes
qui ne s'intéressent plus qu'aux chiffres.
C'est donc pour ça encore
que j'ai acheté une boîte de couleurs et des crayons.*

Le Petit Prince,
"Antoine de Saint-Exupéry"

This work was partially supported by the Spanish *Ministerio de Educación*,
under the grant FPU-AP2005-3308.